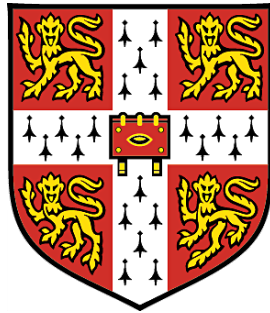


Vibrational and mechanical properties of disordered solids



Rico Milkus

Wolfson College
University of Cambridge

This dissertation is submitted for the degree of
Doctor of Philosophy

November 2017

Vibrational and mechanical properties of disordered solids

Rico Milkus

The recent development of a framework called non-affine lattice dynamics made it possible to calculate the elastic moduli of disordered systems directly from their microscopic structure and potential energy landscape at zero temperature. In this thesis different types of disordered systems were studied using this framework. By comparing the shear modulus and vibrational properties of nearest neighbour spring networks based on depleted lattices we were able to show that the dominating quantity of the system's non-affine reorganisation during shear deformation is the affine force field. Furthermore we found that different implementation of disorder lead to the same behaviour at the isostatic point.

Later we studied the effect of long range interaction in such depleted lattices with regard to spatial correlation local elasticity. We found that the implementation of long springs with decaying spring constant reproduced the spatial correlation observed in simulations of Lennard-Jones glasses.

Finally we looked at simple freely rotating polymer model chains by extending the framework to angular forces and studied the dependence of the shear modulus and the vibrational density of states (VDOS) and length and bending stiffness of the chains. We found that the effect of chain length on the shear modulus and the vibrational density of states diminishes as it depends on the number of backbone bonds in the system. This number increases fast for short chains as many new backbone bonds are introduced but slows down significantly when the chain length reaches 50 monomers per chain. For the dependence on the bending stiffness we found a rich phenomenology that can be understood by looking at specific motions of the monomers relative the the chain geometry. We were able to trace back the different regimes of the VDOS to the simple model of the triatomic molecule. We also explored the limits of non-affine lattice dynamics when describing systems at temperatures $T > 0$ and gave an approximate solution for the shear modulus in this case.

Declaration

This dissertation is the result of my own work and includes nothing which is the outcome of work done in collaboration except as declared in the Preface and specified in the text. It is not substantially the same as any that I have submitted, or, is being concurrently submitted for a degree or diploma or other qualification at the University of Cambridge or any other University or similar institution except as declared in the Preface and specified in the text. I further state that no substantial part of my dissertation has already been submitted, or, is being concurrently submitted for any such degree, diploma or other qualification at the University of Cambridge or any other University or similar institution except as declared in the Preface and specified in the text. It does not exceed the prescribed word limit of 65,000 words and contains no more than 150 figures.

Parts of the thesis contain work that has been published or is to be published:

1. R. Milkus and A. Zaccone, "*Local inversion-symmetry breaking controls the boson peak in glasses and crystals*", Phys. Rev. B **93**, 094204 (2016).
2. R. Milkus and A. Zaccone, "*Atomic-scale origin of dynamic viscoelastic response and creep in disordered solids*", Phys. Rev. E **95**, 023001 (2017).
3. J. Krausser, R. Milkus and A. Zaccone, "*Non-affine lattice dynamics of defective fcc crystals*", Soft Matter **13**, 6079-6089 (2017).
4. J. Krausser and R. Milkus, "*Long range correlation in depleted spring networks*", preprint (2017).
5. R. Milkus, C. Ness, V. Palyulin, J. Weber, A. Lapkin and A. Zaccone, "*Interpretation of the vibrational spectra of glassy polymers using coarse-grained simulations*", submitted to Macromolecules (2017).

I have contributed to all aspects of the research of papers 1-4. I have contributed to all aspects of the research of paper 5 aside from simulations performed by Christopher Ness. Paper 4 is also part of the PhD thesis of Johannes Krausser submitted at the University of Cambridge.

Contents

1	Introduction	1
1.1	Particle interaction	2
1.2	Harmonic approximation and vibrational density of states	3
1.3	Non-affine lattice dynamics	4
2	Disordered lattices	15
2.1	Model systems	15
2.1.1	Depleted random network	16
2.1.2	Depleted FCC	17
2.1.3	FCC with vacancies	17
2.2	Vibrational density of states	17
2.2.1	General remarks	18
2.2.2	Comparison between random network and regular depleted fcc	21
2.2.3	Comparison of different defected fcc lattices	25
2.3	Elastic Properties	27
2.3.1	Affine force field and non-affine correlator function	27
2.3.2	Static shear modulus	30
2.3.3	Complex shear modulus	33
2.4	Summary	38
3	Lattices with long range correlations	43
3.1	Model system	44
3.1.1	Local shear modulus	46
3.1.2	Correlation between local G and G^A, G^{NA}	48
3.2	Spatial correlation function	50
3.3	Numerical results for $C(r)$	57
3.3.1	High bond probability p	58

3.3.2	Critical bond probability p^*	64
3.3.3	Transition from critical to high bond probability	67
3.4	Summary	69
4	Polymer networks	75
4.1	Model systems	76
4.2	Structural analysis	78
4.3	Vibrational density of states	80
4.3.1	Projection on different motion patterns	81
4.3.2	Imaginary frequencies, collective Lennard-Jones sea and higher frequency modes	82
4.3.3	VDOS for chains with $L = 3$	84
4.3.4	VDOS for chains with $L > 3$	88
4.4	Shear modulus	94
4.4.1	The non-affine correlator function	95
4.4.2	Static shear modulus	97
4.4.3	Complex shear modulus	100
4.5	Conclusion	103
5	Conclusion	105
A	Appendix	109
A.1	Explicit form of contributions to \mathbf{H} , $\mathbf{\Xi}$ and G^A	109
A.2	Complex modulus for $Z = 6$	113
A.3	Analytic description of freely joined chains	113
A.4	Analytical description of a single chain with $L = 3$	117
	Bibliography	119

Introduction

A closed analytic description of disordered solids always appeared as difficult. Unlike regular lattices one cannot exploit periodicity to derive dispersion relation and vibrational density of states (VDOS) analytically as was done by P. Debye [1]. The same goes for elastic properties. Although one can calculate the elastic moduli of the affine deformation of a solid, leading to the famous Born-Huang-Approximation [2], it does not match the observed behaviour even in a qualitative way. Efforts to improve on this approximation go back to I.M. Lifshitz [3] and the treatment of single defected lattices with Green's function method. Further developments were made with effective medium theories such as the coherent potential approximation (CPA) [4, 5, 6] that proved very successful in qualitatively reproducing the properties of disordered systems. Recent development of the framework of non-affine lattice dynamics [7], which allows the calculations of elastic constants directly from the microscopic structure and potential energy landscape of a given system at zero temperature, opened up new possibilities for the study of disordered systems. In this work we will explore this framework and apply it to various model systems ranging from nearest neighbour depleted lattices to model polymer chains with various types of interaction potentials. As the framework involves vibrational properties of the system, we will also explore the VDOS and eigenvectors of our model systems.

The theoretical framework of this work is mostly based on the classical description of the systems with Newton's equation. The main points are therefore the modelling of particle interactions as well as finding a solution to the equation of motion for a given system. It proved convenient to transform the equation to Fourier space and analyse its eigenstates, from which one can calculate various physical properties like the static and complex elastic moduli, which we are mostly interested in. In this work we use the normal vector notation \vec{r}_i for the vector components of individual particles and bold characters \mathbf{r} to denote the compo-

nents of the whole system. Particle labels are furthermore written as subscripts and coordinate labels as superscripts, hence r_i^x denotes the x-component of the i -th particle.

1.1 Particle interaction

The interactions between atoms in a medium can in general be written as a series expansion of n-body interaction, where n indicates the number of atoms that participate in the interaction. We can write the total potential as

$$U(\vec{r}_1, \dots, \vec{r}_N) = \sum_i^N U_1(\vec{r}_i) + \sum_{i<j}^N U_2(\vec{r}_i, \vec{r}_j) + \sum_{i<j<k}^N U_3(\vec{r}_i, \vec{r}_j, \vec{r}_k) + \dots \quad , \quad (1.1)$$

where N denotes the total number of atoms in the system. We ignore the one-body term, since it only plays a role in the treatment of external fields with spatial fluctuations, which won't be covered in this work. Furthermore we only use two- and three-body interactions to model the systems, where two-body interactions have the form of pairwise potentials only depending on the relative distance $r_{ij} = |\vec{r}_i - \vec{r}_j|$ of the particles and three-body interactions appear as angular or bending interaction between neighbouring interacting bonds with $\theta_{ijk} = \arccos \frac{\vec{r}_{ij} \cdot \vec{r}_{ik}}{r_{ij} r_{ik}}$. The latter one is important to model the stiffness of polymer chains. To summarize:

$$\begin{aligned} U_2(\vec{r}_i, \vec{r}_j) &= U_2(r_{ij}) \\ U_3(\vec{r}_i, \vec{r}_j, \vec{r}_k) &= U_3(\theta_{ijk}) \end{aligned} \quad (1.2)$$

Higher orders could include dihedral interaction between planes formed by neighbouring angular bonds but are neglected in this work due to their relatively weak strength compared to pairwise and angular interactions.

1.2 Harmonic approximation and vibrational density of states

The equation of motion for N particles interacting in the above established way reads like:

$$\mathbf{M} \ddot{\mathbf{r}} = -\vec{\nabla} U(\mathbf{r})$$

$$\mathbf{r} = (\vec{r}_1, \dots, \vec{r}_N) \quad (1.3)$$

$$\mathbf{M} = \text{diag}(\vec{m}_1, \dots, \vec{m}_N),$$

with the mass matrix \mathbf{M} . Since we study systems at low temperature that are close to mechanical equilibrium at \mathbf{r}_0 , we can expand the potential energy around that minimum:

$$U(\mathbf{r}) \approx U(\mathbf{r}_0) + \vec{\nabla} U(\mathbf{r}_0)(\mathbf{r} - \mathbf{r}_0) + \frac{1}{2}(\mathbf{r} - \mathbf{r}_0)^T \mathbf{H}(\mathbf{r}_0) (\mathbf{r} - \mathbf{r}_0)$$

$$\mathbf{H}(\mathbf{r}_0) = \left(\frac{\partial^2 U(\mathbf{r})}{\partial \vec{r}_i \partial \vec{r}_j} \right)_{i,j=1,\dots,N} \Bigg|_{\mathbf{r} \rightarrow \mathbf{r}_0} = \mathbf{H}. \quad (1.4)$$

Here \mathbf{H} denotes the Hessian of the system and the last equality denotes that the Hessian is evaluated at the rest configuration. Inserting (1.4) into (1.3) gives us:

$$\mathbf{M} \ddot{\mathbf{r}} = -\vec{\nabla} U(\mathbf{r}_0) - \mathbf{H}(\mathbf{r} - \mathbf{r}_0)$$

$$\rightarrow \mathbf{M} \ddot{\mathbf{u}} = -\mathbf{H} \mathbf{u} \quad ; \quad \mathbf{u} = \mathbf{r} - \mathbf{r}_0. \quad (1.5)$$

The second equality holds true since we expanded the potential around a local energy minimum, which gives us $\vec{\nabla} U(\vec{r}_0) = 0$. The last line of (1.5) is called the harmonic approximation of our equation of motion. We now perform a Fourier

transform on it to get:

$$\omega_k^2 \mathbf{M} \hat{\mathbf{v}}_k = \mathbf{H} \hat{\mathbf{v}}_k \quad (1.6)$$

$$\hat{\mathbf{v}}_k = \mathcal{F}(\mathbf{u}).$$

This equation is a generalized eigenvalue problem, which can be solved numerically with standardized methods. By doing so we get the eigenfrequencies ω_k and corresponding eigenvectors $\hat{\mathbf{v}}_k$ of our system. The distribution of eigenfrequencies, known as vibrational density of states (VDOS) is formally defined as:

$$D(\omega) = \frac{1}{dN} \sum_{k=1}^{dN} \delta(\omega - \omega_k), \quad (1.7)$$

where d is the spatial dimension of our system. According to (1.7) the VDOS is normalized to 1, which is the convention we use for the remainder of the work.

1.3 Non-affine lattice dynamics

The main interest of our research is to study the shear modulus of disordered solids, which is defined as the ratio between the applied stress to the resulting strain. The following part, describing the mathematical and conceptual framework of its calculation, closely follows the formalism of A. Lemaître and C. Maloney [7]. The general idea is that after a initial affine deformation, which is just an linear transformation of the coordinates due to a deformation tensor, the particles undergo a second non-affine relaxation into a nearby energy minimum. This process is continuous and the particles actually follow an equilibrium trajectory during the deformation process.

We start with the initial deformation where every particle i undergoes an affine displacement $\vec{r}_i \rightarrow \vec{r}'_i = \mathbf{F} \vec{r}_i$ with the deformation tensor \mathbf{F} for pure shear:

$$\mathbf{F} = \begin{pmatrix} \cos(\gamma/2) & \sin(\gamma/2) & 0 \\ \sin(\gamma/2) & \cos(\gamma/2) & 0 \\ 0 & 0 & 1 \end{pmatrix}, \quad (1.8)$$

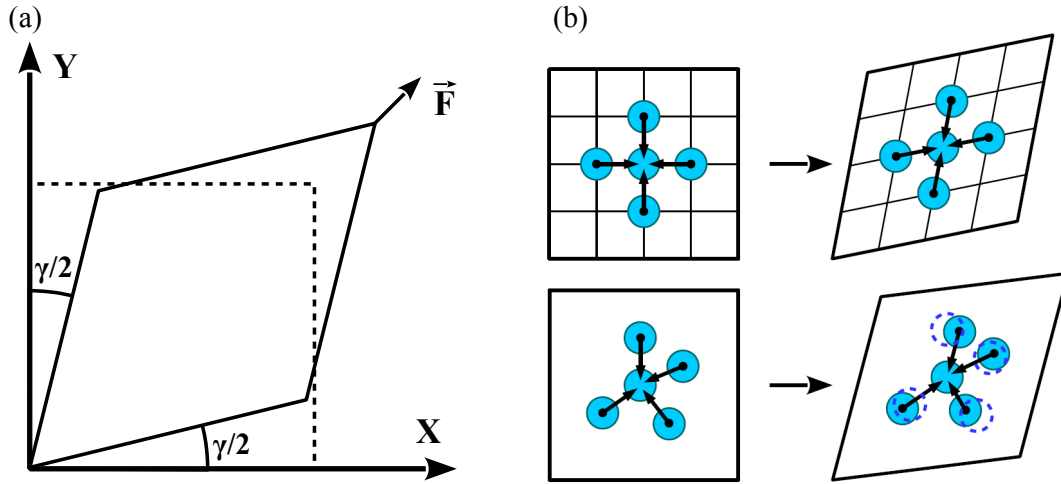


Figure 1.1: (a) Sketch of the shear deformation corresponding to (1.8). (b) difference between lattices and disordered systems. After an affine deformation the latter in general is not in equilibrium any more, as the built up forces don't balance each other out as in the case of a perfect lattice.

where γ is the shear angle. To calculate the shear modulus it is useful to define the *Green-Saint Venant strain tensor* $\boldsymbol{\eta}$

$$\boldsymbol{\eta} = \frac{1}{2}(\mathbf{F}^T \mathbf{F} - \mathbf{1}) = \frac{1}{2} \begin{pmatrix} 0 & \sin \gamma & 0 \\ \sin \gamma & 0 & 0 \\ 0 & 0 & 0 \end{pmatrix}. \quad (1.9)$$

In general elastic constants are defined as second derivatives of the energy of a transformation $U(\mathbf{r}, \boldsymbol{\eta}(\gamma)) = U(\mathbf{r}, \gamma)$ with respect to the strain. We use the shear deformation as an example but the formalism works for different types of deformations.

To be able to calculate the shear modulus for our system we have to determine the change of energy in dependence of the shear strain. One part arises from the affine displacement due to (1.8). In the absence of inversion symmetry (IS) the system will not be in mechanical equilibrium after the affine deformation. So each atom will perform a non-affine relaxation to its rest position in the sheared system. We can specify the trajectory of this process by the condition that no force acts on

each atom i at any time.

$$\vec{f}'_i = -\frac{\partial U'(\mathbf{r}', \gamma)}{\partial \vec{r}'_i} = -\frac{\partial U(\mathbf{r}, \gamma)}{\partial \vec{r}_i} \mathbf{F}^{-1} \stackrel{!}{=} 0 \quad \longrightarrow \quad \frac{\partial U(\mathbf{r}, \gamma)}{\partial \vec{r}_i} = 0. \quad (1.10)$$

Here U' refers to the fact that it is defined in terms of coordinates after the transformation (1.8) with the identity $U'(\mathbf{r}', \gamma) = U(\mathbf{r}, \gamma)$ holding true. We want to know how this condition changes under the shear deformation, so we derive (1.10) with respect to γ

$$\frac{\partial^2 U}{\partial \vec{r}_i \partial \vec{r}_j} \cdot \frac{\mathcal{D} \vec{r}_j}{\mathcal{D} \gamma} + \frac{\partial^2 U}{\partial \vec{r}_i \partial \gamma} = 0. \quad (1.11)$$

The symbol \mathcal{D} indicates that the derivatives taken satisfy (1.10), meaning that it is taken along the equilibrium trajectory. In the limit $\gamma \rightarrow 0$ this involves the Hessian \mathbf{H} of our system and the *affine force field* Ξ

$$\left. \frac{\partial^2 U}{\partial \vec{r}_i \partial \vec{r}_j} \right|_{\gamma \rightarrow 0} = \mathbf{H}_{ij}. \quad (1.12)$$

$$\left. \frac{\partial^2 U}{\partial \vec{r}_i \partial \gamma} \right|_{\gamma \rightarrow 0} = -\Xi_i. \quad (1.13)$$

So we can express the solution of (1.11)

$$\left. \frac{\mathcal{D} \mathbf{r}}{\mathcal{D} \gamma} \right|_{\gamma \rightarrow 0} = \mathbf{H}^{-1} \Xi = \delta \mathbf{r}. \quad (1.14)$$

As we can see, the non-affine displacement is just a linear response to the affine force field, which also acts as a measure for the local inversion symmetry breaking. Now it is possible to calculate the shear modulus accordingly as the second

derivative of the energy after the strain.

$$G = \frac{1}{V} \left. \frac{\mathcal{D}^2 U}{\mathcal{D}\gamma^2} \right|_{\gamma \rightarrow 0}, \quad (1.15)$$

where V denotes the volume of the system. As in (1.11) the derivative has to be taken along the trajectory that satisfies (1.10). The second derivative is calculated as follows

$$\begin{aligned} \left. \frac{\mathcal{D}}{\mathcal{D}\gamma} \frac{\mathcal{D}U}{\mathcal{D}\gamma} \right|_{\gamma \rightarrow 0} &= \left. \frac{\mathcal{D}}{\mathcal{D}\gamma} \left(\frac{\partial U}{\partial \gamma} + \frac{\partial U}{\partial \mathbf{r}} \cdot \frac{\mathcal{D}\mathbf{r}}{\mathcal{D}\gamma} \right) \right|_{\gamma \rightarrow 0} = \left. \frac{\mathcal{D}}{\mathcal{D}\gamma} \frac{\partial U}{\partial \gamma} \right|_{\gamma \rightarrow 0} \\ &= \left. \left(\frac{\partial^2 U}{\partial \gamma^2} + \frac{\partial^2 U}{\partial \mathbf{r} \partial \gamma} \cdot \frac{\mathcal{D}\mathbf{r}}{\mathcal{D}\gamma} \right) \right|_{\gamma \rightarrow 0} = \left. \frac{\partial^2 U}{\partial \gamma^2} \right|_{\gamma \rightarrow 0} - \boldsymbol{\Xi} \mathbf{H}^{-1} \boldsymbol{\Xi}. \end{aligned} \quad (1.16)$$

$$G = \frac{1}{V} \left(\left. \frac{\partial^2 U}{\partial \gamma^2} \right|_{\gamma \rightarrow 0} - \boldsymbol{\Xi} \mathbf{H}^{-1} \boldsymbol{\Xi} \right) = G^A - G^{NA}. \quad (1.17)$$

In the first line of (1.16) we used the equilibrium condition $\frac{\partial U}{\partial \mathbf{r}} = 0$. The affine term is the well known Born-Huang-approximation [2]. The negative non-affine term softens the material due to the relaxation process (1.14).

To calculate the non-affine part of the shear modulus we have to deal with the inverse of the Hessian. Since this is generally difficult to obtain we will derive an explicit expression for G^{NA} including the eigenvalues λ_k and the normalized eigenvectors $\hat{\mathbf{v}}_k$ of the original Hessian:

$$\begin{aligned} G^{NA} &= \frac{1}{V} \boldsymbol{\Xi} \mathbf{H}^{-1} \boldsymbol{\Xi} = \frac{1}{V} \boldsymbol{\Xi} \cdot \left(\mathbf{H}^{-1} \sum_k \hat{\boldsymbol{\Xi}}_k \hat{\mathbf{v}}_k \right) \\ &= \frac{1}{V} \boldsymbol{\Xi} \cdot \left(\sum_{\substack{k \\ \lambda_k \neq 0}} (\boldsymbol{\Xi} \cdot \hat{\mathbf{v}}_k) \frac{1}{\lambda_k} \hat{\mathbf{v}}_k \right) = \frac{1}{V} \sum_{\substack{k \\ \lambda_k \neq 0}} \frac{(\boldsymbol{\Xi} \cdot \hat{\mathbf{v}}_k)^2}{\lambda_k}. \end{aligned} \quad (1.18)$$

Let's look at the affine force field of a disordered system as it is shown Fig. 1.2.

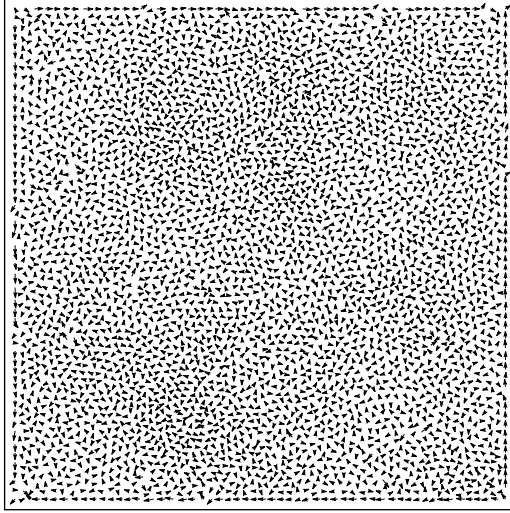


Figure 1.2: The affine force field $\vec{\Xi}$ for the shear deformation of a 2D disordered system. One can see the random character of the field as there are very little correlations between neighbored components.

Due to the random behaviour we can assume that the projection of this field onto eigenstates ($\vec{\Xi} \cdot \hat{\mathbf{v}}_k$) is a self-averaging quantity. So for a large number of atoms in our system we can introduce a frequency dependent correlator $\Gamma(\omega)$ as an average performed over eigenfrequencies $\omega_k \in [\omega, \omega + \delta\omega]$

$$\Gamma(\omega) = \left\langle (\vec{\Xi} \cdot \hat{\mathbf{v}}_k)^2 \right\rangle_{\omega_k \in [\omega, \omega + \delta\omega]} . \quad (1.19)$$

With that we can reformulate (1.18) in the thermodynamic limit

$$G^{NA} = \frac{1}{V} \sum_{\substack{k \\ \lambda_k \neq 0}} \frac{(\vec{\Xi} \cdot \hat{\mathbf{v}}_k)^2}{\lambda_k} \stackrel{N/V \rightarrow \infty}{=} \text{const.} \quad d \frac{N}{V} \int_0^\infty \frac{D(\omega)\Gamma(\omega)}{\omega^2} d\omega . \quad (1.20)$$

Here d denotes the spatial dimension of our system. This leaves us with three quantities to calculate: \mathbf{H} , $\vec{\Xi}$ and G^A . As all of them are defined as the second

derivative of the potential energy we write down the general form

$$\begin{aligned}\frac{\partial^2 U(z)}{\partial x \partial y} &= \frac{d^2 U(z)}{dz^2} \frac{\partial z}{\partial x} \frac{\partial z}{\partial y} + \frac{dU(z)}{dz} \frac{\partial^2 z}{\partial x \partial y} \\ &= \mathbf{c} \frac{\partial z}{\partial x} \frac{\partial z}{\partial y} + \mathbf{t} \frac{\partial^2 z}{\partial x \partial y},\end{aligned}\tag{1.21}$$

with stiffness \mathbf{c} and tension \mathbf{t} . The stiffness is also referred to as *spring constant* κ as it fulfils this role in the harmonic approximation. In our case z is either the distance between two particles r_{ij} or the angle formed by two bonds θ_{ijk} and x, y are either spatial components of particle positions r_i^a or the shear angle γ . This gives us the three possible combinations to calculate the three above mentioned quantities:

$$\begin{aligned}\mathbf{H}_{ij}^{ab} &= \frac{\partial^2 U(z)}{\partial r_i^a \partial r_j^b} = \mathbf{c} \frac{\partial z}{\partial r_i^a} \frac{\partial z}{\partial r_j^b} + \mathbf{t} \frac{\partial^2 z}{\partial r_i^a \partial r_j^b}. \\ \Xi_i^a &= \frac{\partial^2 U(z)}{\partial r_i^a \partial \gamma} = \mathbf{c} \frac{\partial z}{\partial r_i^a} \frac{\partial z}{\partial \gamma} + \mathbf{t} \frac{\partial^2 z}{\partial r_i^a \partial \gamma}. \\ G^A &= \frac{\partial^2 U(z)}{\partial \gamma^2} = \mathbf{c} \frac{\partial z}{\partial \gamma} \frac{\partial z}{\partial \gamma} + \mathbf{t} \frac{\partial^2 z}{\partial \gamma^2}.\end{aligned}\tag{1.22}$$

Note that all derivatives are evaluated at $\gamma \rightarrow 0$. We derive the explicit dependence on the shear angle from the deformation tensor:

$$\vec{r}'_{ij} = \mathbf{F} \vec{r}_{ij} = \begin{pmatrix} r_{ij}^x \cos(\gamma/2) + r_{ij}^y \sin(\gamma/2) \\ r_{ij}^y \cos(\gamma/2) + r_{ij}^x \sin(\gamma/2) \\ r_{ij}^z \end{pmatrix}.\tag{1.23}$$

$$r'_{ij} = \sqrt{r_{ij}^2 + 2r_{ij}^x r_{ij}^y \sin \gamma}.$$

With that we can calculate the relevant derivatives, whose explicit forms are shown in the Appendix A.1.

Next we look at the complex shear modulus G^* , also called viscoelastic shear modulus. To calculate it, we assume our system is submerged in a viscous medium, apply an oscillatory shear deformation on the system and calculate the elastic response. To dissipate the energy put in by the driving force we assume viscous damping proportional to the relative velocity $\dot{\mathbf{r}}' - \mathbf{u}(\mathbf{r}')$ with the affine flow $\mathbf{u}(\mathbf{r}') = \dot{\mathbf{F}} \mathbf{r} = \dot{\mathbf{F}} \mathbf{F}^{-1} \mathbf{r}'$. This gives us the following equation of motion:

$$\mathbf{M} \ddot{\mathbf{r}}' = \mathbf{f}' - \nu (\dot{\mathbf{r}}' - \mathbf{u}(\mathbf{r}')), \quad (1.24)$$

with the mass matrix $\mathbf{M} = \text{diag}(m_1, \dots, m_N)$ and the friction coefficient matrix $\nu = \text{diag}(\nu_1, \dots, \nu_N)$. Again primed quantities denote the dynamic positions and unprimed quantities the reference configuration. With $\mathbf{r}' = \mathbf{F} \mathbf{r}$ we can write this in terms of the reference configuration:

$$\mathbf{M} \ddot{\mathbf{r}} = \mathbf{f}' - \mathbf{M} \ddot{\mathbf{F}} \mathbf{r} - 2 \mathbf{M} \dot{\mathbf{F}} \dot{\mathbf{r}} - \nu \mathbf{F} \dot{\mathbf{r}}. \quad (1.25)$$

The term $\mathbf{M} \ddot{\mathbf{F}} \mathbf{r}$ breaks translation invariance of the above equation as it spatially couples particle motion with the coordinates as was noted by Anderson, Ray and Rahman [8, 9]. In [10] a formalism was introduced that allows to cancel the spatially dependent terms from the equation of motion. Following that we can rewrite (1.25) as:

$$\mathbf{M} \ddot{\mathbf{r}} = \mathbf{f}' - 2 \mathbf{M} \dot{\mathbf{F}} \dot{\mathbf{r}} - \nu \mathbf{F} \dot{\mathbf{r}}. \quad (1.26)$$

Under the assumption of small strain $|\mathbf{F} - \mathbf{1}| \ll 1$ we expand this equation around a known equilibrium state \mathbf{r} in terms of small displacements $\mathbf{x} = \mathbf{r}(t) - \mathbf{r}(0)$; $\mathbf{r}(0) = \mathbf{r}$

and get:

$$\begin{aligned}
m_i \frac{d^2 \vec{x}_i}{dt^2} &= \frac{\partial f'_i}{\partial \vec{r}_j} \vec{x}_j + \frac{\partial f'_i}{\partial \gamma} \gamma - \nu_i \frac{d \vec{x}_i}{dt}, \\
m_i \frac{d^2 \vec{x}_i}{dt^2} + \nu_i \frac{d \vec{x}_i}{dt} + \mathbf{H}_{ij} \vec{x}_j &= \vec{\Xi}_i \gamma(t), \\
\mathbf{M} \frac{d^2 \mathbf{x}}{dt^2} + \nu \frac{d \mathbf{x}}{dt} + \mathbf{H} \mathbf{x} &= \mathbf{\Xi} \gamma(t).
\end{aligned} \tag{1.27}$$

We have written the first two lines in terms of components to make clear how the Hessian \mathbf{H} and affine force field $\mathbf{\Xi}$ enter the equation. We now have a simple damped harmonic oscillator with the affine force field as the emerging driving force from a small deformation, which is exactly the role it played when we first introduced it. Note that we explicitly included the time dependence of the small deformation γ in the last step to emphasize that we have a dynamically driven system and the deformation can have an arbitrary time dependence as long as it stays small. To solve (1.27) we perform a Fourier transform:

$$-\mathbf{M} \Omega^2 \tilde{\mathbf{x}} + i \Omega \nu \tilde{\mathbf{x}} + \mathbf{H} \tilde{\mathbf{x}} = \mathbf{\Xi} \tilde{\gamma}. \tag{1.28}$$

Here we assumed a driving force $\gamma(t) = \tilde{\gamma} \sin \Omega t$. We further decompose the Fourier components and the affine force field into eigenvectors $\hat{\mathbf{v}}_k$ of the Hessian:

$$\begin{aligned}
\tilde{\mathbf{x}} &= \sum_k \hat{\mathbf{x}}_k \hat{\mathbf{v}}_k \quad ; \quad \mathbf{\Xi} = \sum_k \hat{\mathbf{\Xi}}_k \hat{\mathbf{v}}_k = \sum_k (\mathbf{\Xi} \cdot \hat{\mathbf{v}}_k) \hat{\mathbf{v}}_k, \\
\left[(\omega_k^2 - \Omega^2) \mathbf{M} + i \Omega \nu \right] \hat{\mathbf{x}}_k \hat{\mathbf{v}}_k &= \hat{\mathbf{\Xi}}_k \hat{\mathbf{v}}_k \tilde{\gamma}, \\
\hat{\mathbf{x}}_k &= (\mathbf{\Xi} \cdot \hat{\mathbf{v}}_k) \hat{\mathbf{v}}_k^T \left[(\omega_k^2 - \Omega^2) \mathbf{M} + i \Omega \nu \right]^{-1} \hat{\mathbf{v}}_k \tilde{\gamma}.
\end{aligned} \tag{1.29}$$

From there we can calculate the difference Δt between the stress at γ and $\gamma = 0$ in first order expansion:

$$\begin{aligned}
\Delta t &= \frac{1}{V} \left[\frac{\partial U}{\partial \gamma}(\mathbf{r}(t), \gamma) - \frac{\partial U}{\partial \gamma}(\mathbf{r}, 0) \right] \\
&= \frac{1}{V} \left[\frac{\partial^2 U}{\partial \gamma^2} \gamma + \frac{\partial^2 U}{\partial \gamma \partial \mathbf{r}} \mathbf{r}(t) - \frac{\partial^2 U}{\partial \gamma \partial \mathbf{r}} \mathbf{r}(0) \right] \\
&= \frac{1}{V} \left[\frac{\partial^2 U}{\partial \gamma^2} \gamma + \frac{\partial^2 U}{\partial \gamma \partial \mathbf{r}} \mathbf{x}(t) \right].
\end{aligned} \tag{1.30}$$

Again by Fourier transform we get the stress response in frequency space:

$$\begin{aligned}
\tilde{\Delta t}(\Omega) &= \frac{1}{V} \left[\frac{\partial^2 U}{\partial \gamma^2} \tilde{\gamma} + \frac{\partial^2 U}{\partial \gamma \partial \mathbf{r}} \tilde{\mathbf{x}}(\Omega) \right] = \frac{1}{V} \left[\frac{\partial^2 U}{\partial \gamma^2} \tilde{\gamma} - \boldsymbol{\Xi} \tilde{\mathbf{x}}(\Omega) \right] \\
&= G^A \tilde{\gamma} - \frac{1}{V} \sum_k \hat{\boldsymbol{\Xi}}_k \hat{\mathbf{x}}_k \\
&= G^A \tilde{\gamma} - \frac{1}{V} \sum_k \hat{\boldsymbol{\Xi}}_k^2 \hat{\mathbf{v}}_k^T \left[(\omega_k^2 - \Omega^2) \mathbf{M} + i \Omega \nu \right]^{-1} \hat{\mathbf{v}}_k \tilde{\gamma} \\
&= G^*(\Omega) \tilde{\gamma} \\
\rightarrow G^*(\Omega) &= G^A - \frac{1}{V} \sum_k (\boldsymbol{\Xi} \cdot \hat{\mathbf{v}}_k)^2 \hat{\mathbf{v}}_k^T \left[(\omega_k^2 - \Omega^2) \mathbf{M} + i \Omega \nu \right]^{-1} \hat{\mathbf{v}}_k.
\end{aligned} \tag{1.31}$$

Here we inserted the definition of the affine force field (1.13) and the expansion $\boldsymbol{\Xi} \tilde{\mathbf{x}} = \sum_{k,k'} \hat{\boldsymbol{\Xi}}_{k'} \hat{\mathbf{v}}_{k'} \hat{\mathbf{x}}_k \hat{\mathbf{v}}_k = \sum_{k,k'} \hat{\boldsymbol{\Xi}}_{k'} \hat{\mathbf{x}}_k \delta_{k,k'} = \sum_k \hat{\boldsymbol{\Xi}}_k \hat{\mathbf{x}}_k$, where we used the orthonormality of eigenvectors as well as the solution of $\hat{\mathbf{x}}_k$ from (1.29). (1.31) gives us the viscoelastic modulus for small oscillatory deformations. For equal particles $\mathbf{M} = m\mathbf{1}$ and $\nu = \nu\mathbf{1}$, the expression simplifies to:

$$G^*(\Omega) = G^A - \frac{1}{V} \sum_k \frac{(\boldsymbol{\Xi} \cdot \hat{\mathbf{v}}_k)^2}{m(\omega_k^2 - \Omega^2) + i\nu\Omega}. \tag{1.32}$$

We can see that for $\Omega \rightarrow 0$ it coincides with the definition of the shear modulus from (1.18), which is why we also call this case the static shear modulus. Although it appears as if the static modulus depends on the mass one has to keep in mind that $\omega_k^2 \sim 1/m$ so the mass cancels out as it should. We can split the complex modulus into the real part (storage modulus) and the imaginary part (loss modulus) $G^*(\Omega) = G'(\Omega) + i G''(\Omega)$:

$$G'(\Omega) = G^A - \frac{1}{V} \sum_k \frac{m (\boldsymbol{\Xi} \cdot \hat{\mathbf{v}}_k)^2 (\omega_k^2 - \Omega^2)}{m^2 (\omega_k^2 - \Omega^2)^2 + \nu^2 \Omega^2},$$

$$G''(\Omega) = \frac{1}{V} \sum_k \frac{\nu (\boldsymbol{\Xi} \cdot \hat{\mathbf{v}}_k)^2 \Omega}{m^2 (\omega_k^2 - \Omega^2)^2 + \nu^2 \Omega^2}.$$
(1.33)

In the thermodynamic limit we can write (1.33) as integrals involving $D(\omega)$ and $\Gamma(\omega)$:

$$G'(\Omega) = G^A - d \frac{N}{V} \int_0^\infty \frac{m D(\omega) \Gamma(\omega) (\omega^2 - \Omega^2)}{m^2 (\omega^2 - \Omega^2)^2 + \nu^2 \Omega^2} d\omega,$$

$$G''(\Omega) = d \frac{N}{V} \int_0^\infty \frac{\nu D(\omega) \Gamma(\omega) \Omega}{m^2 (\omega^2 - \Omega^2)^2 + \nu^2 \Omega^2} d\omega.$$
(1.34)

Disordered lattices

Disordered systems are difficult to analyse analytically as they lack any kind of long range symmetry or periodicity. Tools were however developed to approximate the features of realistic systems by simpler model systems. One very interesting class of models for amorphous solids are disordered lattices, where the disorder is implemented by e.g. bond cutting or particle displacements. In general particle interactions are restricted to nearest neighbour only, which is justified for systems, where long range interactions, e.g. by electronic contributions, can be neglected. Examples for those are colloidal glasses or systems with very strong short range interactions. Depleted lattices have the advantage of showing many typical features of disordered solids while at the same time having a regular spatial structure. This allows a relatively easy implementation of effective medium theories such as CPA [4, 5, 6]. Furthermore they allow for a controlled transition from order to disorder and the observation of various interesting quantities such as particle vibration patterns and displacement fields during deformations along this transition.

In the following chapter, which is mostly based on [11, 12, 13], quantities are calculated by averaging over ten realisations each unless stated otherwise.

2.1 Model systems

In this work we will discuss three types of disordered lattices: a) random networks, where particles are not arranged on a lattice, b) depleted fcc lattices, where bonds are cut and c) fcc lattices with vacancies, where particles are removed. Two dimensional sketches of the systems are shown in Fig. 2.1.

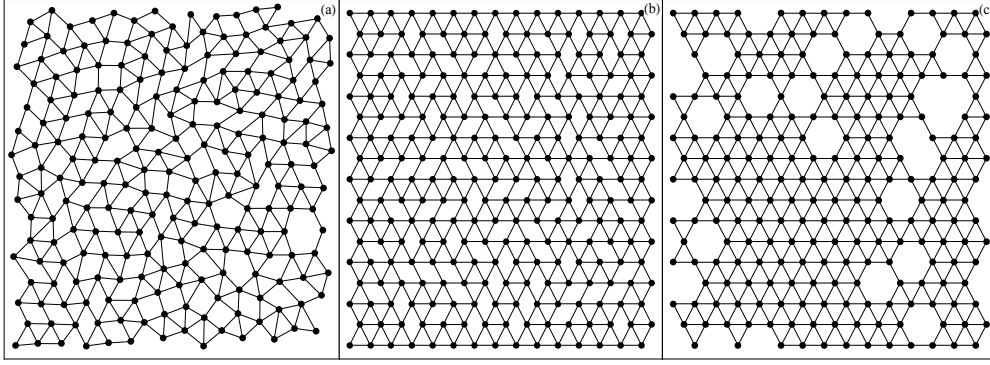


Figure 2.1: A 2D sketch of the three systems used in this work. a) A random network, where particles are arranged in a spatially disordered way, b) a depleted fcc lattice, where single bonds are removed and c) a defected fcc lattices, where whole particles are removed.

2.1.1 Depleted random network

We use a random network (RN) created by first randomly placing $N = 4000$ soft spheres with mass $m = 1$ in a box and letting them interact via a truncated LJ potential $V(r) = (1/r^{12} - 2/r^6 + 0.031) \Theta(2 - r)$. The system is brought to a metastable lower energy state by a Monte Carlo energy-relaxation algorithm, which produces a narrow nearest neighbour bond length distribution around $r_0 = 0.94$. The volume of the box is chosen such to create a dense network with an average coordination number $\langle Z \rangle = 10$, that fluctuates throughout the network. Since we are interested in the effect of the coordination number on the system, we cut bonds from the initial configuration. To limit spatial fluctuations of the shear modulus G in the system we cut bonds in an adaptive way to achieve a narrow coordination number distribution. We studied systems with average coordination numbers from $\langle Z \rangle = 9$ down to $\langle Z \rangle = 6$. The density is kept at a constant value $N/V = 1.467$ and we implemented periodic boundary conditions to avoid surface effects. To make the RN more comparable with the fcc lattices, we assume that each bond is at rest length and model the interaction between the particles by harmonic springs according with spring constant $\kappa = 1$.

2.1.2 Depleted FCC

The second system we studied is a depleted fcc lattice with lattice constant $a = 1$, which gives us a nearest neighbour bond length of $r_0 = 1/\sqrt{2}$. Again we use $N = 4000$ particles with mass $m = 1$, a volume $V = 1000$ and hence a density of $\rho = 4$. The bond cutting was performed in two different ways: a) similar to the RN we cut bonds so that (almost) each site has the same coordination number (regular depleted fcc) and b) we cut bonds with a given probability $p = \langle Z \rangle / 12$ which gives us a system with a binomial distributed coordination number that has on average $\langle Z \rangle$ bonds per particle (random depleted fcc).

2.1.3 FCC with vacancies

The third type of systems that we looked at is a fcc lattice with vacancies. The initial lattice is the same as in 2.1.2 but instead of removing bonds we remove a certain proportion c of particles. In contrast to the other systems the bond defects are not completely uncorrelated as each vacancy removes multiple bonds in a specific pattern. Another key difference is the changing density of the system. Whereas in the other model systems the number of particles and therefore the density stays constant, the density of the vacancy fcc depends on the number of removed particles $\rho' = N'/V = N(1 - c)/V = \rho(1 - c)$. The coordination number is by default distributed comparable to the randomly depleted fcc.

2.2 Vibrational density of states

In the first part we look at the vibrational density of states and compare the different systems. We are especially interested in the low-frequency part as it has a large influence on the elastic constants due to the $1/\omega^2$ factor in (1.20). We thereby compare similar average coordination numbers to see the differences between the different configurations. To aid clarity we will denote the average coordination number as $\langle Z \rangle = Z$.

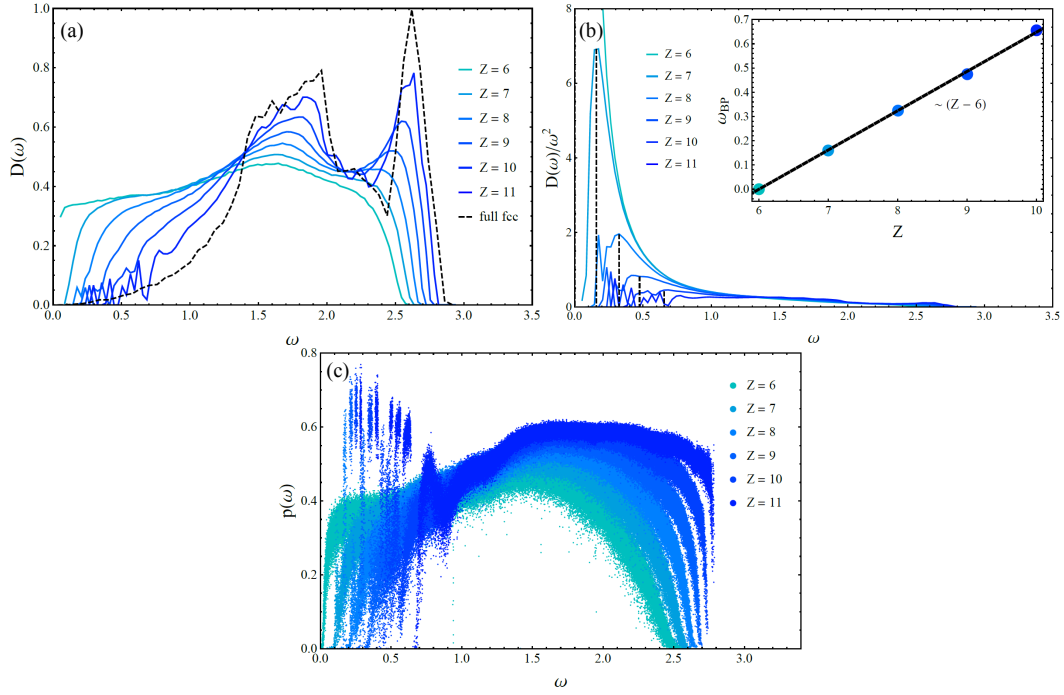


Figure 2.2: (a): VDOS of our random depleted fcc lattice for different average coordination numbers Z . By comparing to the VDOS of a perfect fcc we can identify the peaks as remnants of the two van-Hove singularities of the fcc lattice. (b): Reduced VDOS plots of the same systems, which show the boson peak anomaly. The dashed lines indicate the position, which is plotted against the average coordination number in the inset. Our numerical results reproduce the well known $\omega_{BP} \sim (Z - 6)$ scaling. (c): Participation ratio of the systems.

2.2.1 General remarks

In Fig. 2.2 we see the VDOS for the random depleted fcc, which has the typical features of a disordered system, especially the Boson Peak (BP) anomaly in the reduced VDOS $D(\omega)/\omega^2$. This phenomenon is well known for disordered solids [14, 15, 16] and was recently found even in non-centrosymmetric crystals such as α -Quartz [17]. As expected the frequency of the BP scales as $\omega_{BP} \sim Z - Z^* = Z - 6$, where $Z^* = 6$ denotes the critical connectivity at which the number of constraints (i.e. bonds) is equal to the degrees of freedom (dimension times number of particles):

$$\frac{NZ^*}{2} = dN \longrightarrow Z^* = 2d. \quad (2.1)$$

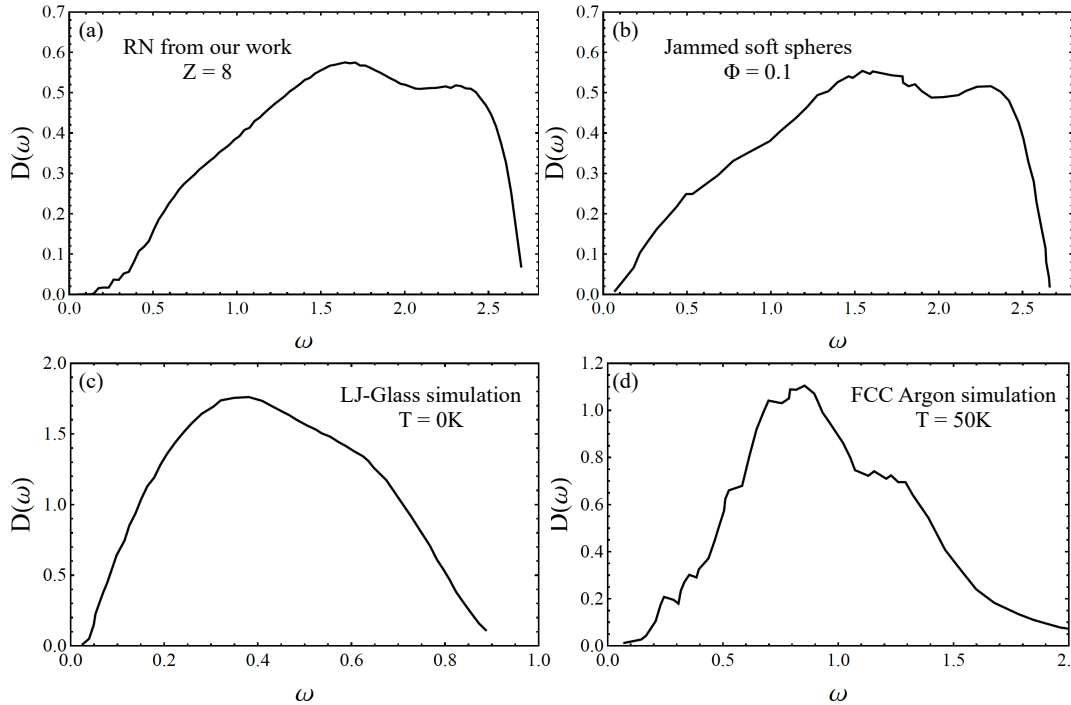


Figure 2.3: Comparison of VDOS between our random network (a) and simulations of soft spheres (b), Lennard-Jones glass (c) and crystalline Argon (d). All plots were created with digitized data from the original plots. In (b,c) the spectrum is obtained in the same way as in our work, while in (d) it was calculated as the Fourier transform of the velocity autocorrelation function. We can see that all systems show similar features as the VDOS obtained from our system.

We also see that at the critical point $D(\omega \rightarrow 0) \neq 0$, which means there are modes with zero energy present in the system, i.e. particles can move relative to each other without additional energy. This is usually associated with mechanical failure as we will see in the later section when we discuss the shear modulus of our systems. Another important feature of the VDOS is the low frequency regime below ω_{BP} , which we call the Debye-regime as it follows the famous $D(\omega) \sim \omega^2$ law found by Debye. Due to the limited system size and the regular structure of the lattice, the eigenvalues tend to cluster at low frequencies, which is why the Debye regime is not very well visible [18]. It was derived for perfect lattices by using the discrete translational symmetry and the associated modes are perfect plane waves, known as phonons. Although this symmetry is broken in our depleted fcc the lattice sites are still similar in structure to each other and the system shows some regularity on long distances. Therefore modes with long wavelengths $\lambda \sim 1/\omega$

can pass through the system almost without being scattered. This breaks down as soon as the modes are being scattered by the defects in the lattices, which happens right before the BP anomaly, where the VDOS deviates from the Debye law.

Another remnant of the perfect fcc lattice are the two peaks visible at higher frequencies. In The perfect fcc they are the two van-Hove singularities stemming from the structure of the Brillouin zone of the reciprocal lattice. Although there is no notion of a Brillouin zone in the depleted lattice the remnants of the corresponding peaks can still be seen.

One quantity that shows this transition is the participation ratio $p(\omega)$, which tells us if the oscillations of a given mode (eigenvector) are localized at a few sites or delocalized over the whole system. As phonons are collective lattice excitations they are delocalized. We mentioned before that in defected systems there are no real phonons as there is no translational symmetry. Still, the term phonon-like is useful, since the modes are close in behaviour to actual phonons and it allows us to distinguish them from other modes in the VDOS, such as diffusons or locons [19, 20, 21]. $p(\omega)$ is defined as:

$$p(\omega) = p(\omega_k) = \frac{1}{N} \frac{\left(\sum_{i=1}^N |\vec{v}_{k,i}|^2 \right)^2}{\sum_{i=1}^N |\vec{v}_{k,i}|^4}. \quad (2.2)$$

The participation ratio has two limits: $p(\omega) = 1$, if the amplitude of a mode is equal at all sites and $p(\omega) = 1/N$, if only one site is participating at a given mode. With the participation ratio we can clearly distinguish four different regimes: a) the low frequency Debye regime with delocalized phonon-like modes, b) the localization transition, where modes are starting to get scattered due to defects, c) the diffusive regime, where the components of the eigenvectors are randomly distributed over the whole system and d) the localized modes close to the maximum frequency, also called locons [21]. We can see this transition very well in Fig. 2.2(c). The localization transition is believed to be closely connected to the Ioffe-Regel transition [22, 23, 24], although there are doubts about the exact connection. The results for our model systems are in good agreement with the findings of [23, 24] for similar systems, which indicates that the same basic mechanisms are at work.

In Fig. 2.3 we can see the VDOS from our depleted random network with $Z = 8$ next to spectra from other work. The spectrum of (b) is calculated from a jammed system of soft spheres with packing fraction above the critical point $\phi - \phi_c = 0.1$ in the same way as our VDOS by diagonalizing the Hessian [25]. (c) shows the spectrum from a simulation of a binary Lennard-Jones glass at $T = 0K$, again calculated from the eigenvalues of the Hessian [26]. The system in (d) is a simulation of fcc Argon at $T = 50K$ and the VDOS is obtained from the Fourier transform of the velocity autocorrelation function [27]. We can see that all VDOS show similar features such as a low frequency Debye part and two van-Hove singularity remnants. Naturally the system most similar to our own (b) shows the biggest similarity. In the jammed system the first van-Hove remnant is at lower frequencies and thus begins to merge with the Boson peak anomaly, while the second one is suppressed compared to our results. This can be explained by the polydispersity of the system which increases the disorder of the system and weakens the features of the perfect lattice. The simulated Argon shows the most noise as it was obtained from Fourier transform. Aside from that the spectrum shows similar features as the one from our simple model system. All those comparisons show that the nearest neighbour lattice model indeed is a reasonable model for disordered solids and gives reliable results for the VDOS.

2.2.2 Comparison between random network and regular depleted fcc

In Fig. 2.4 we see the VDOS of our two regular depleted systems in comparison. The most interesting feature is the similarity in the low frequency regime, which is unexpected due to the very different spatial structure of the two systems. We can show this difference with the bond orientation order parameter F_6 [28, 29], which can be calculated as follows:

$$F_6 = \frac{1}{N} \sum_{i=1}^N \frac{1}{Z_i} \sum_{j=1}^{Z_i} S_{6,ij} \tag{2.3}$$

$$S_{6,ij} = \frac{\sum_{m=-6}^6 Y_{6m}(\theta_{ij}, \phi_{ij}) Y_{6m}^*(\theta_{ij}, \phi_{ij})}{\left| \sum_{m=-6}^6 Y_{6m}(\theta_{ij}, \phi_{ij}) \right|^2} .$$

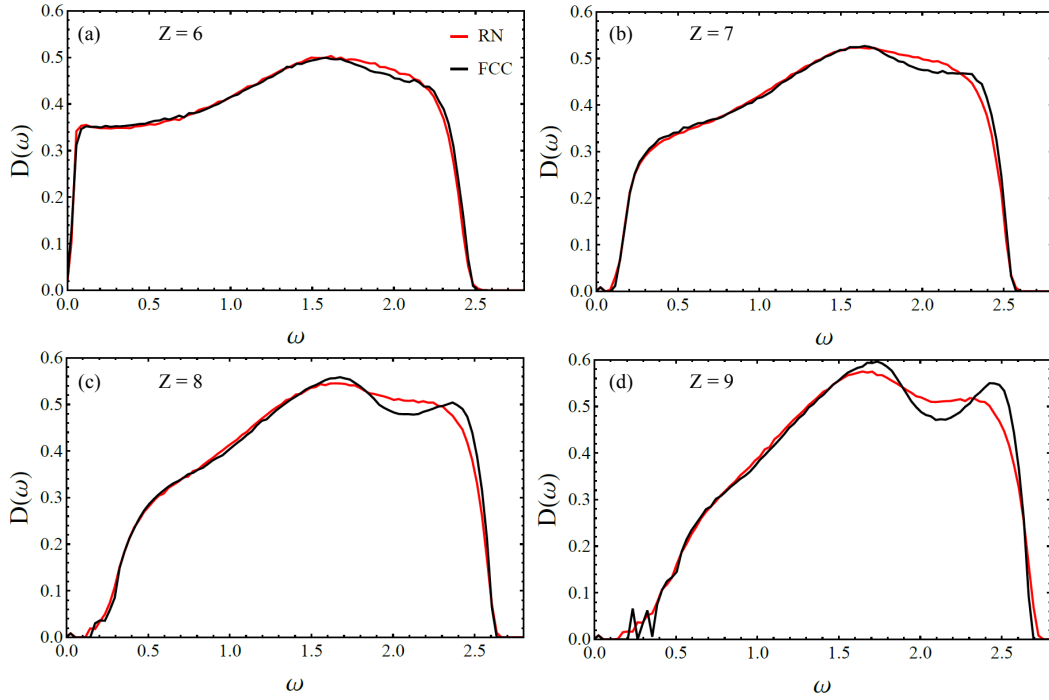


Figure 2.4: Comparisson of VDOS between regular depleted random network (red) and fcc (black). We can easily see the striking similarities at low frequencies. The fcc has a noisier Debye regime, since, due to its regular structure, the eigenfrequencies are clustering more at low frequencies. Differences arise at the van-Hove remnants, again due to the structural differences.

Here (θ_{ij}, ϕ_{ij}) denote the angles of the bond between i and j measured against some reference coordinate system (in general Cartesian). The F_6 parameter measures how much a system resembles a perfect fcc lattice and is usually used as a measure for disorder. As we can see in Fig. 2.5, this parameter fails to reproduce the striking similarities of our two model systems.

Therefore we introduced a different parameter F_{ISB} based on the breaking of inversion symmetry. An easy way to implement this is to use the affine force field Ξ , which is a measure for the local symmetry breaking, although it falls short of capturing the effect of mass disorder. Since we do have only one mass in our system it is still worthwhile to study the affine force field. We use the definition of Ξ_{ab} for central forces where all bonds are at rest position r_0 and have equal

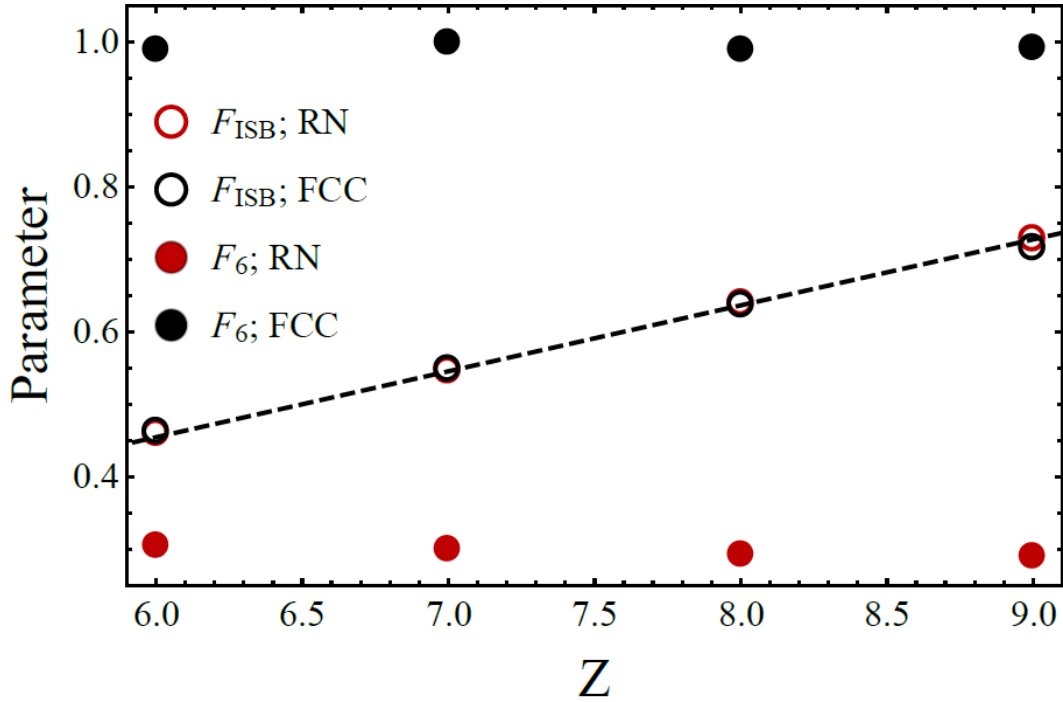


Figure 2.5: Comparison of F_6 between regular depleted random network (full circles). While the fcc has a bond orientational order of almost 1, the random network has a very low value around 0.3. This reflects the structural differences of both systems. In contrast, the parameter F_{ISB} proposed in this work (open circles) reflects the similarities in inversion symmetry breaking very well and follows the analytical form of (2.7) (dashed line).

spring constant κ :

$$\vec{\Xi}_{ab,i} = -\kappa r_0 \sum_{j=1}^{Z_i} \hat{n}_{ij}^a \hat{n}_{ij}^b \hat{n}_{ij} \quad (2.4)$$

$$F_{ISB} = 1 - \frac{\sum_{a,b} |\Xi_{ab}|^2}{\sum_{a,b} |\Xi_{ab,ref}|^2}$$

Here \hat{n}_{ij} is the unit bond vector between i and j . In section 1.3 we have looked at non-affine lattice dynamics in the framework of shear deformation with the corresponding affine force field Ξ_{xy} . To get a general order parameter we consider contributions Ξ_{ab} from all possible linear deformations $a, b = x, y, z$. We measure

the sum of all affine force fields associated with those deformations against a reference random configuration, where there are no restrictions for relative bond orientations, i.e. excluded volume.

$$\begin{aligned}
\sum_{a,b} |\Xi_{ab}|^2 &= \sum_{a,b} \sum_{i=1}^N \left| \kappa r_0 \sum_{j=1}^{Z_i} \hat{n}_{ij}^a \hat{n}_{ij}^b \hat{n}_{ij} \right|^2 \\
&= \kappa^2 r_0^2 \sum_{a,b} \sum_{i=1}^N \sum_{j,k=1}^{Z_i} \hat{n}_{ij}^a \hat{n}_{ij}^b \hat{n}_{ik}^a \hat{n}_{ik}^b (\hat{n}_{ij} \cdot \hat{n}_{ik}) \\
&= \kappa^2 r_0^2 \sum_{i=1}^N \sum_{j,k=1}^{Z_i} (\hat{n}_{ij} \cdot \hat{n}_{ik})^3 \\
&= \kappa^2 r_0^2 \left(NZ + \sum_{i=1}^N \sum_{j \neq k}^{Z_i} (\hat{n}_{ij} \cdot \hat{n}_{ik})^3 \right).
\end{aligned} \tag{2.5}$$

For the random case the second term averages to zero as we pick the bonds random and independent of each other. Therefore we get:

$$\begin{aligned}
\sum_{a,b} |\Xi_{ab,\text{ref}}|^2 &= \kappa^2 r_0^2 NZ. \\
F_{ISB} &= 1 - \frac{\sum_{a,b} |\Xi_{ab}|^2}{\sum_{a,b} |\Xi_{ab,\text{ref}}|^2} = -\frac{1}{NZ} \sum_{i=1}^N \sum_{j \neq k}^{Z_i} (\hat{n}_{ij} \cdot \hat{n}_{ik})^3.
\end{aligned} \tag{2.6}$$

So the breaking of inversion symmetry is directly related to the relative orientation of the bonds around each particle. In the case of the regular depleted fcc F_{ISB} coincides with another quantity related to inversion symmetry, which is the fraction of bonds having an opposing bond. It can be calculated by just considering one bond and the probability for it having an opposing bond:

$$p(\text{opposing bond}) = \frac{\binom{1}{1} \binom{10}{Z-2}}{\binom{11}{Z-1}} = \frac{Z-1}{11}. \tag{2.7}$$

As can be seen in Fig. 2.5 the behaviour of F_{LSB} not only mirrors the similarities between our two regular depleted systems very nicely, but also follows the function of bond opposing probability for the regular depleted fcc. This shows that inversion symmetry plays an important role in the description of disordered materials, especially around the boson peak anomaly. It also provides an argument to use depleted lattice systems as a general model for glassy systems, for which there are various analytical and semi-analytical tools, e.g. CPA.

2.2.3 Comparison of different defected fcc lattices

Next we compared the three model systems based on defected fcc lattices with each other to study the effects of different types of bond disorder. First we studied the distribution of the coordination number Z in the random depleted fcc and the fcc with vacancies. In the case of the randomly depleted fcc it is quite simple: For a given lattice site there is a chance of p for each bond being depleted and a chance of $1 - p$ for the bond being intact. The probability of having z bonds is therefore:

$$p_{\text{depl}}(z) = \binom{12}{z} (1-p)^z p^{12-z} \quad (2.8)$$

$$\langle Z \rangle_{\text{depl}} = \sum_{z=0}^{12} z \binom{12}{z} (1-p)^z p^{12-z} = 12(1-p).$$

The distribution for the vacancy case works in the same way. Here the probability for a bond being cut depends on whether the second particle is removed or not. The probability for this being c and $1 - c$. Analogous to (2.8) we can write:

$$p(z)_{\text{vac}} = \binom{12}{z} (1-c)^z c^{12-z} \quad (2.9)$$

$$\langle Z \rangle_{\text{vac}} = \sum_{z=0}^{12} z \binom{12}{z} (1-c)^z c^{12-z} = 12(1-c).$$

So both systems have a binomial coordination number distribution, which makes them quite different from the regular depleted fcc, which has (almost) a delta

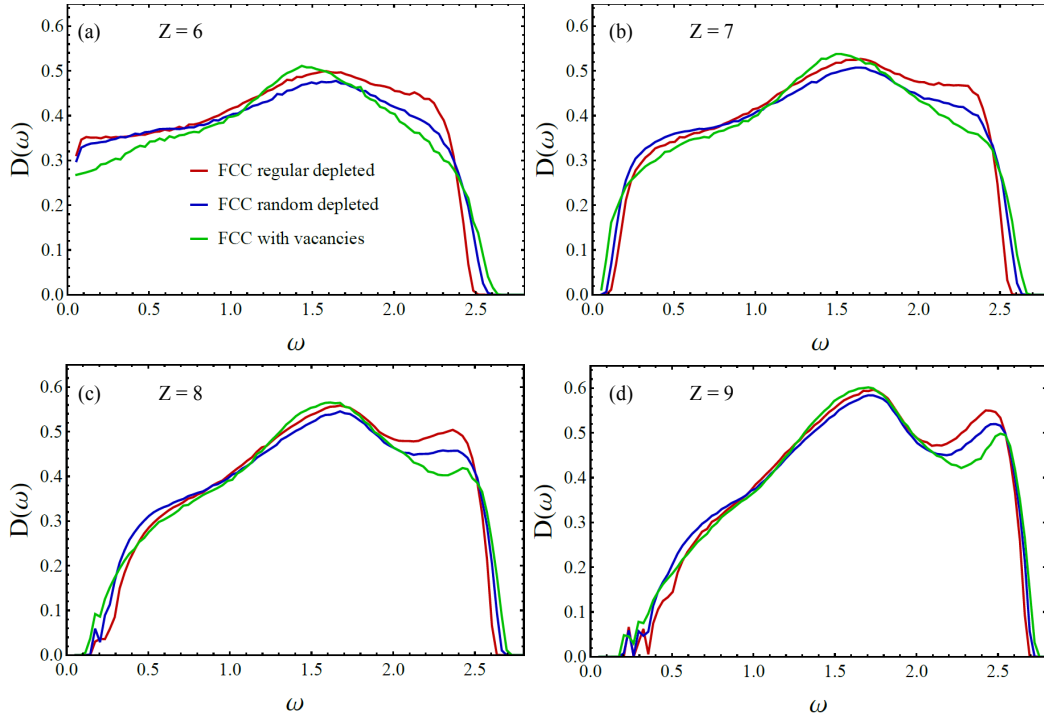


Figure 2.6: Comparison of our three different fcc models for different Z . When looking at the high frequency van-Hove remnant we can see the disorder hierarchy of the three systems. The regular depleted fcc is the most ordered with the most pronounced peak, whereas the vacancy system has the lowest. The random depleted system lies in between having the coordination number distribution from one and the single bond cutting structure from the other.

distributed coordination number. In Fig. 2.6 we see the VDOS of the three systems in comparison. Although they are based on the exact same lattice their VDOS looks quite different, especially when compared to the striking resemblance of the regular depleted random network and the regular depleted fcc, which had quite different spatial structures yet very similar VDOS. This hints at the fact that the connectivity structure of the system is more relevant for the vibrations possible than the spatial structure of the underlying network, which agrees with the observations from Sec. 2.2.2, where similar VDOS were obtained due to similar connectivity structure but very different spatial structure. This is supported by the observation that, although having the same Z and the same distribution $p(z)$ the randomly depleted fcc has a quite different VDOS than the fcc with vacancies. In the latter the missing bonds are not entirely uncorrelated as the removal of one particle removes bonds in a specific pattern. This is in stark contrast to the

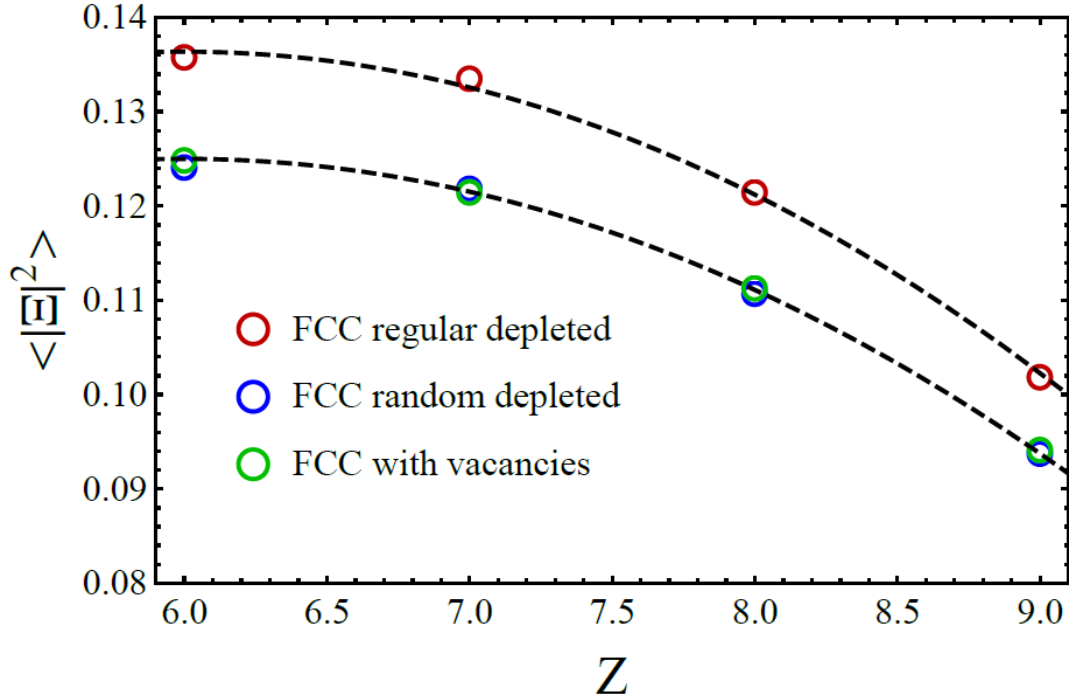


Figure 2.7: Comparison of the affine force field strengths of our systems. As you can see they follow nicely the analytic prediction from (2.10) and (2.12).

explicit independent removal of individual bonds and affects the distributions of supported vibrations in the system.

2.3 Elastic Properties

Next we will examine the shear modulus of our model systems. First we will study the corresponding affine force field Ξ and the related correlator function $\Gamma(\omega)$. From there we will calculate the static shear modulus as well as the complex modulus resulting from oscillatory shear and compare the different systems with each other.

2.3.1 Affine force field and non-affine correlator function

A very important part of the shear modulus is the non-affine relaxation process leading to G^{NA} introduced in Section 1.3. It is guided by the affine force field which also is a measure of inversion symmetry as shown before. For the regular

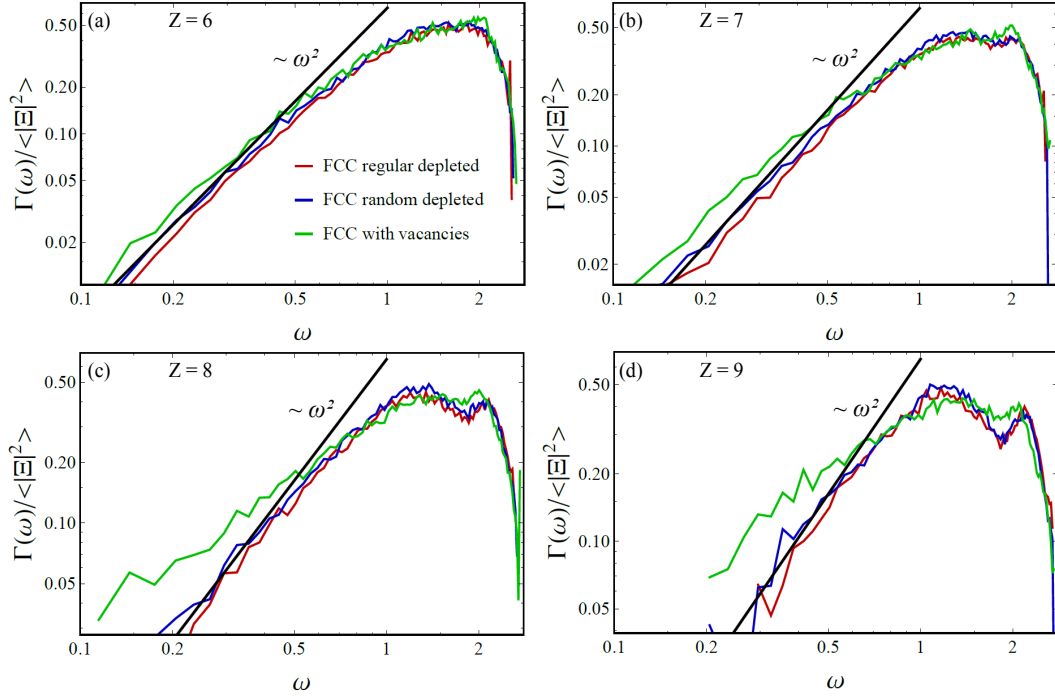


Figure 2.8: Comparison of $\Gamma(\omega)$ of our systems. As expected the depleted systems scale like $\sim \omega^2$. Away from the critical point $Z = 6$ the fcc with vacancies shows a diverging behaviour.

depleted fcc we can evaluate the affine force field exactly by using the definition in (2.4) and averaging over all possible configurations:

$$\langle |\Xi|^2(Z) \rangle = 2 \kappa^2 r_0^2 \sum_{i=0}^4 \sum_{j=0}^2 \frac{(2j-i)^2}{8} \frac{\binom{2}{j} \binom{2}{i-j} \binom{8}{Z-i}}{\binom{12}{Z}} = \kappa^2 r_0^2 \frac{Z(12-Z)}{11 \cdot 12}. \quad (2.10)$$

We get this result by using the fact that in a fcc only the four bonds lying in the x-y-plane are contributing to the affine force field, of which two contribute $-\kappa r_0 \hat{n}_{ij}^x \hat{n}_{ij}^y \hat{n}_{ij}$ and two contribute $+\kappa r_0 \hat{n}_{ij}^x \hat{n}_{ij}^y \hat{n}_{ij}$ to Ξ . If we look at only one direction (e.g. x) we have i bonds in the x-y plane, of which j bonds give a positive and $i-j$ bonds a negative contribution. Another $Z-i$ bonds lie not in the x-y plane with a total of $\binom{12}{Z}$ possible configurations. Since we are interested in the square of the affine force field each configuration has the weight $(2j-i)^2 (\hat{n}_{ij}^x \hat{n}_{ij}^y \hat{n}_{ij}^x)^2 = (2j-i)^2/8$, since $\hat{n}_{ij} = (\pm 1, \pm 1, 0)/\sqrt{2}$, counted twice for x- and y-direction, which gives us the prefactor 2.

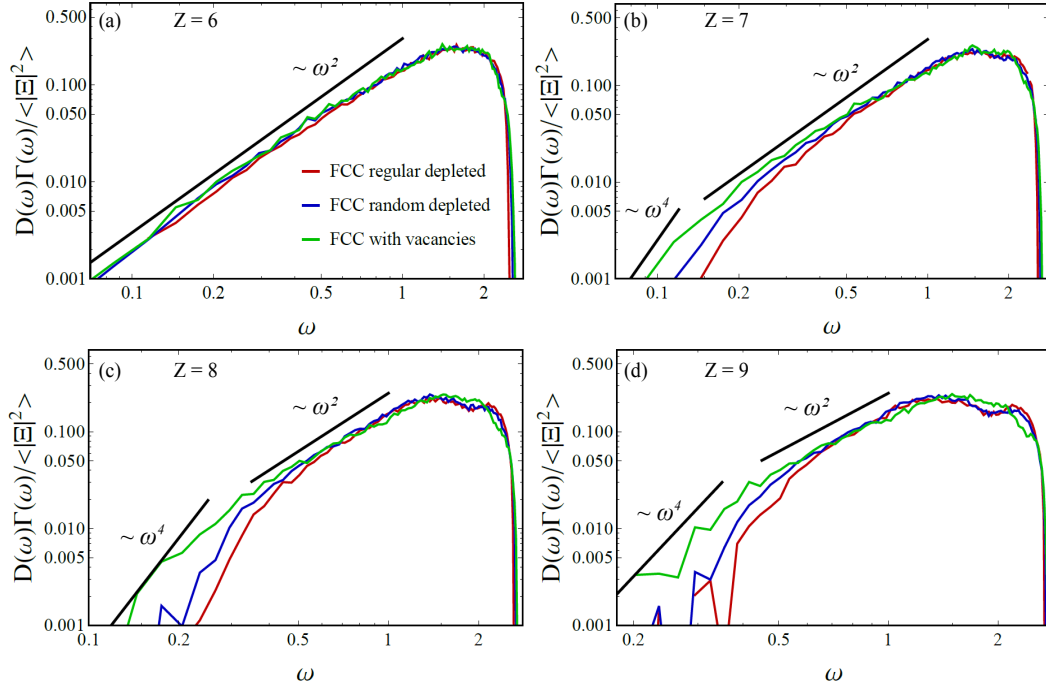


Figure 2.9: Comparison of $D(\omega)\Gamma(\omega)$ of our systems. We can see the change in low frequency scaling from $\sim \omega^2$ to $\sim \omega^4$ caused by the developing Debye regime. It is important to note that the differences between the vacancy fcc and the other two systems lessen for this combined quantity $D(\omega)\Gamma(\omega)$, which is the defining quantity for the calculation of shear modulus G .

It is interesting to see how the strength of the affine force field changes with the distribution of $p(z)$. In a large enough system we can assume that $|\Xi|^2 = N_z \langle |\Xi|^2(z) \rangle$. Hence we get:

$$\begin{aligned}
 \langle |\Xi|^2 \rangle &= \kappa^2 r_0^2 \sum_{z=0}^{12} \frac{N_z z(12-z)}{N \cdot 11 \cdot 12} = \frac{\kappa^2 r_0^2}{11 \cdot 12} \sum_{z=0}^{12} p(z) z(12-z) \\
 &= \frac{\kappa^2 r_0^2}{11 \cdot 12} (12 \langle Z \rangle - \langle Z^2 \rangle) = \kappa^2 r_0^2 \frac{\langle Z \rangle (12 - \langle Z \rangle) - \sigma_z^2}{11 \cdot 12}.
 \end{aligned} \tag{2.11}$$

This is surprising, since one would have expected that additional disorder in the system, due to distribution of the coordination number, would lead to an increase of $|\Xi|^2$. An intuitive explanation for this behaviour is the fact that sites with

lower coordination number Z can still have configurations with a high degree of inversion symmetry, whereas the opposite is not true as highly coordinated sites cannot go below a certain threshold of base symmetry. For our two model systems with binomially distributed Z we can evaluate σ_z^2 and $\langle |\Xi|^2 \rangle$ directly:

$$\sigma_z^2 = 12p(1-p) = \frac{\langle Z \rangle (12 - \langle Z \rangle)}{12}. \quad (2.12)$$

$$\langle |\Xi|^2 \rangle = \kappa^2 r_0^2 \frac{\langle Z \rangle (12 - \langle Z \rangle) - \sigma_z^2}{11 \cdot 12} = \kappa^2 r_0^2 \frac{\langle Z \rangle (12 - \langle Z \rangle)}{12 \cdot 12}.$$

As we can see in Fig. 2.7 this fits the numerical results very well.

From the affine force field we can evaluate the correlator function $\Gamma(\omega)$ according to (1.19), which acts as a weight for the different modes when calculating G^{NA} . Results are shown in Fig. 2.8, where we can see that $\Gamma(\omega) \propto \omega^2$ is approximately true for low frequencies, as was found by A. Zaccone [31]. Another important point is that, if normalized with $\langle |\Xi|^2 \rangle$, correlators of the different fcc systems have the same magnitude and general behaviour. Both properties become even clearer, when we look at the product $D(\omega)\Gamma(\omega)$, which plays an important role in the non-affine integral (1.20), highlighting the importance of inversion symmetry breaking in non-affine relaxation. In Fig. 2.9 we can see that $D(\omega)\Gamma(\omega)$ shows two different scalings for low frequencies: $\sim \omega^4$ and $\sim \omega^2$. The first scaling is a combination of the Debye regime $D(\omega) \sim \omega^2$ and the scaling of the Gamma function $\Gamma(\omega) \sim \omega^2$. As we get closer to the critical point at $Z = 6$, the Debye regime vanishes and the VDOS scales like $D(\omega) \sim 1$ for low frequencies. This difference will become very important later on when we will look at the complex modulus of our systems.

2.3.2 Static shear modulus

We finally look at the shear modulus of our fcc lattices. The affine part is calculated according to (1.22). We can explicitly write down the expression under the assumption that only pairwise interactions at rest position are taking place:

$$G^A = \frac{1}{V} \sum_{i \neq j} \frac{\partial^2 U(r_{ij})}{\partial \gamma^2} = \frac{\kappa}{V} \sum_{i \neq j} \left(\frac{\partial r_{ij}}{\partial \gamma} \right)^2 = \frac{\kappa r_0^2}{V} \sum_{i \neq j} \left(\hat{n}_{ij}^x \hat{n}_{ij}^y \right)^2. \quad (2.13)$$

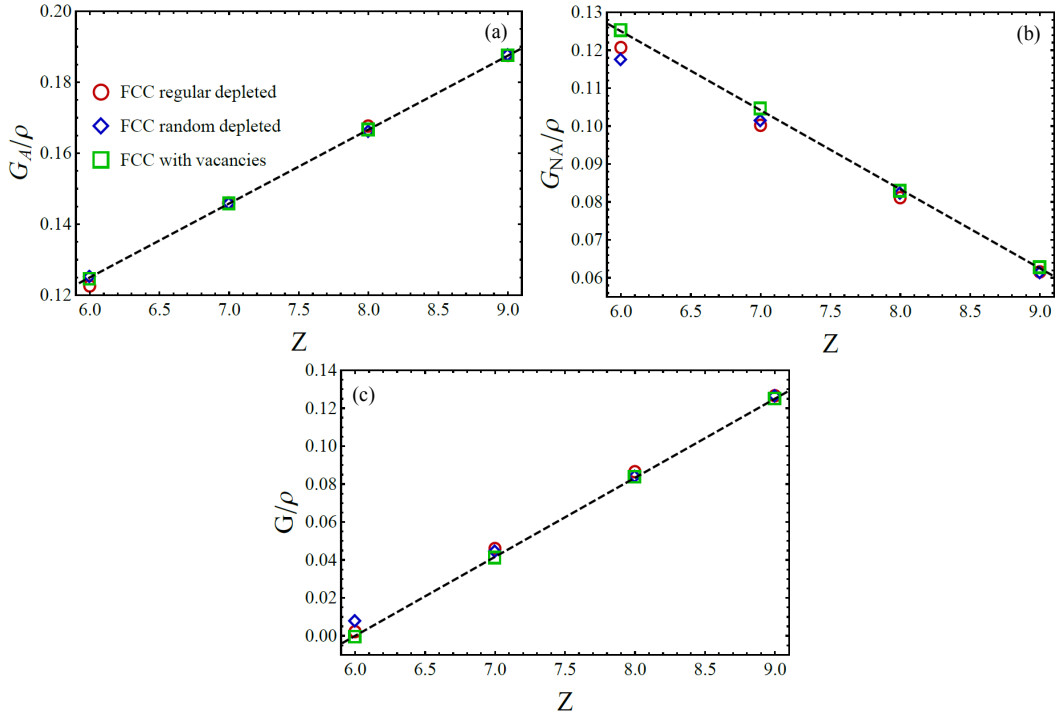


Figure 2.10: Results for the shear modulus G of our three fcc systems, normalized to the density ρ . Dashed line denotes the analytic result. As we can see within numerical error all three systems show the same behaviour.

We can calculate this in the same way as the quantities before by averaging over all possible configurations. The four bonds in the x-y plane each contribute $\kappa r_0^2/4$, whereas all other bonds contribute nothing. Hence we get for a large number of particles:

$$\begin{aligned}
 G^A(Z) &= \frac{1}{2} \frac{N}{V} \langle G_i^A \rangle = \frac{1}{2} \frac{N}{V} \sum_{j=0}^4 j \frac{\kappa r_0^2}{4} \frac{\binom{4}{j} \binom{8}{Z-j}}{\binom{12}{Z}} \\
 &= \frac{N}{V} \kappa r_0^2 \frac{Z}{24} = \frac{\kappa}{a} \frac{Z}{12}.
 \end{aligned} \tag{2.14}$$

Here a is the lattice constant of our fcc and we used the fact that there are 4 atoms per cell in a fcc, which gives us $Nr_0^2/V = a^2/2 \cdot 4/a^3 = 2/a$. The non-affine part G^{NA} cannot be calculated in a similar analytic fashion. But from the numerical results (Fig. 2.10) we can guess a linear fitting by using the two configurations at

$Z = 12$ (perfect lattice) and $Z = 6$ (isostatic point):

$$Z = 12 : G^{NA} = 0.$$

$$Z \leq 6 : G^{NA} = G^A.$$

$$\rightarrow G^{NA}(Z) = \begin{cases} \frac{N}{V} \kappa r_0^2 \frac{12 - Z}{24} = \frac{\kappa}{a} \frac{12 - Z}{12}, & \text{if } Z > 6 \\ \frac{N}{V} \kappa r_0^2 \frac{Z}{24} = \frac{\kappa}{a} \frac{Z}{12}, & \text{if } Z \leq 6 \end{cases} \quad (2.15)$$

$$\rightarrow G(Z) = G^A(Z) - G^{NA}(Z) = \begin{cases} \frac{N}{V} \kappa r_0^2 \frac{Z - 6}{12} = \frac{\kappa}{a} \frac{Z - 6}{6}, & \text{if } Z > 6 \\ 0, & \text{if } Z \leq 6 \end{cases}$$

This fits the numerical results very well and reproduces the $G \propto Z - 6$ scaling in three dimensions found in [30, 31, 32]. We can also see that the shear modulus in a depleted lattice is, aside from Z , determined by the ratio of the spring constant and lattice constant. Since all parts of the shear modulus are linear in Z , it is reasonable to expect that the results from (2.14) and (2.15) also hold true for the random depleted lattice when replacing $Z \rightarrow \langle Z \rangle$. We can see from our results that this and the coordination number distribution have no impact on the shear modulus G for the random depleted fcc. When it comes to the fcc with vacancies the situation is different due to the change in density N/V as we remove particles from the system. To get the right results we have to correct the density according to section 2.1.3:

$$\frac{N'}{V} = (1 - c) \frac{N}{V} = \frac{\langle Z \rangle}{12} \frac{N}{V}. \quad (2.16)$$

Since this factor enters all parts of the shear modulus as a constant factor, we just have to multiply the results from the depleted lattice by $\langle Z \rangle / 12$:

$$\begin{aligned}
 G_{\text{vac}}^A &= \frac{\kappa \langle Z \rangle^2}{a 12^2} = \frac{\kappa}{a} (1 - c)^2. \\
 G_{\text{vac}}^{NA} &= \frac{\kappa \langle Z \rangle}{a 12} \frac{12 - \langle Z \rangle}{12} = \frac{\kappa}{a} c (1 - c). \\
 G_{\text{vac}} &= \frac{\kappa \langle Z \rangle}{a 12} \frac{\langle Z \rangle - 6}{6} = \frac{\kappa}{a} (1 - c)(1 - 2c).
 \end{aligned} \tag{2.17}$$

This fits the numerical results very well as can be seen in Fig. 2.10. To summarize: If normalized by the density, all three different fcc systems show the same shear modulus, which mirrors the similarities in the average affine force field $\langle |\Xi|^2 \rangle$ and $D(\omega)\Gamma(\omega)$ as well as the inversion symmetry breaking related to $\langle |\Xi|^2 \rangle$.

2.3.3 Complex shear modulus

Next we look at the complex modulus of our model systems. Since the mass of our particles is $m = 1$, we can simplify the expression for $G^*(\Omega)$ so we only have the friction ν as a free parameter:

$$\begin{aligned}
 G^*(\Omega) &= G^A - \frac{1}{V} \sum_k \frac{(\Xi \cdot \hat{\mathbf{v}}_k)^2}{\omega_k^2 - \Omega^2 + i\nu\Omega}. \\
 &\rightarrow G^A - 3 \frac{N}{V} \int_0^\infty \frac{D(\omega)\Gamma(\omega)}{\omega^2 - \Omega^2 + i\nu\Omega} d\omega.
 \end{aligned} \tag{2.18}$$

The complex modulus has the two limits $G^*(0) = G^A - G^{NA} = G$ and $G^*(\infty) = G^A$. The lower limit makes sense as one assumption of the non-affine lattice dynamics formalism was a very slow shear deformation so the particles can follow their equilibrium trajectories to the non-affine positions. This is realized by the driving frequency approaching zero. In the upper limit the opposite is the case and the particles have no time to relax to their non-affine positions, which is why only the affine part of the deformations takes place. The real part of the shear modulus

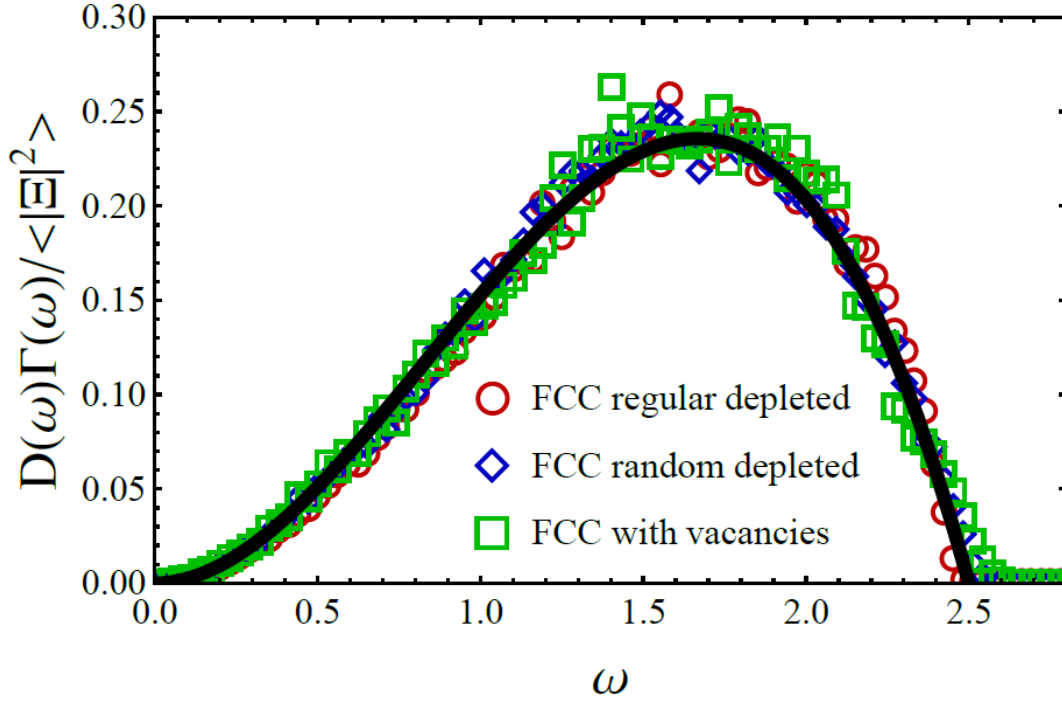


Figure 2.11: Fitting of $D(\omega)\Gamma(\omega)/\langle|\Xi|^2\rangle$ at the isostatic point $Z = 6$. We can see that the function $D(\omega)\Gamma(\omega) \sim \omega^2(\omega_D - \omega)$ (thick black line) agrees quite well with the numerical data. For this fit we chose $\omega_D = 2.5$.

shows a transition between those two values. First we study the influence of the friction, which mainly governs the peak position Ω_{peak} of $G''(\Omega)$ and therefore the frequency at which the transition from $G'(\Omega) \sim G$ to $G'(\Omega) \sim G^A$ takes place. To get a feeling for the general behaviour of Ω_{peak} , we just consider the contribution of one frequency $\omega = \text{const.}$ in (2.18) and set $(\Xi \cdot \hat{\mathbf{v}}_k)^2 \sim 1$, as its value doesn't change the scaling. From there we get:

$$G''(\Omega) \sim \frac{\nu \Omega}{(\omega^2 - \Omega^2)^2 + \nu^2 \Omega^2}.$$

$$\left. \frac{dG''(\Omega)}{d\Omega} \right|_{\Omega_{\text{peak}}} = 0. \quad (2.19)$$

$$\Omega_{\text{peak}}^2 = \frac{1}{6} \left[2\omega^2 - \nu^2 + |\nu^2 - 2\omega^2| \sqrt{1 + \frac{12\omega^4}{(\nu^2 - 2\omega^2)^2}} \right].$$

To show the scaling for large friction, we assume $\nu^2 \gg 2\omega^2$ and expand the root as $\sqrt{1+x} \approx 1 + \frac{1}{2}x$. From that we get:

$$\Omega_{\text{peak}}^2(\nu \rightarrow \infty) \approx \frac{1}{6} \left[-\nu^2 + |\nu^2| \left(1 + \frac{1}{2} \frac{12\omega^4}{\nu^4} \right) \right] = \frac{\omega^4}{\nu^2}.$$

$$\Omega_{\text{peak}}(\nu \rightarrow \infty) \sim \frac{1}{\nu}. \quad (2.20)$$

$$\Omega_{\text{peak}}(\nu \rightarrow 0) = \omega = \text{const.}$$

These scalings are well reproduced by our numerical results for G'' as shown in Fig. 2.12. Quantitatively, the actual position and height of the peaks are of course not matching perfectly as the calculation of $G^*(\Omega)$ involves the non-trivial function $D(\omega)\Gamma(\omega)$. The peak in $G''(\Omega)$ coincides with the transition of $G'(\omega)$ between G and G^A .

However, close to the critical point $Z = 6$ this function is well approximated by:

$$D(\omega)\Gamma(\omega) = a \cdot \omega^2(\omega_D - \omega). \quad (2.21)$$

for all our lattice systems, as can be seen in Fig. 2.11. We can give some insight into the relation between the cut-off or Debye frequency ω_D and the prefactor a . As we are at the critical point, the static shear modulus $G^*(0)$ has to vanish, which leads us to:

$$G^*(0) = G^A(Z = 6) - 3 \frac{N}{V} \int_0^{\omega_D} \frac{a \cdot \omega^2(\omega_D - \omega)}{\omega^2} d\omega$$

$$= \frac{1}{2} - 12 \frac{a\omega_D^2}{2} = 0 \quad \rightarrow \quad a\omega_D^2 = \frac{1}{12}. \quad (2.22)$$

Here we used the results from our depleted fcc lattice. Since the density drops out, the result is also valid for the fcc with vacancies.

Since ω_D is set by the system, it is not a free parameter, which leaves us only

with the friction as parameter of interest. To analyse its effect on the system, particularly $G''(\Omega)$, we will examine both frequency regimes, $\Omega \ll \omega_D$ and $\Omega \gg \omega_D$, with either very small or large friction. The maximum frequency ω_D of the system acts a useful measure to determine if the driving frequency is small or large compared to the system's eigenfrequencies.

We start with the high frequency limit, where we assume $\Omega \gg \omega_D \rightarrow \Omega^2 - \omega^2 \approx \Omega^2$. With the approximation from before we can rewrite the equation for G'' as:

$$\begin{aligned}
G''(\Omega) &= \frac{3}{12\omega_D^2} \frac{N}{V} \int_0^{\omega_D} \frac{\nu \Omega \omega^2 (\omega_D - \omega)}{(\omega^2 - \Omega^2)^2 + \nu^2 \Omega^2} d\omega \\
&\approx \frac{1}{\omega_D^2} \int_0^{\omega_D} \frac{\nu \Omega \omega^2 (\omega_D - \omega)}{\Omega^4 + \nu^2 \Omega^2} d\omega \\
&= \frac{1}{\omega_D^2} \frac{\nu}{\Omega(\Omega^2 + \nu^2)} \frac{\omega_D^4}{12} \tag{2.23} \\
&= \frac{\omega_D^2}{12} \frac{\nu}{\Omega(\Omega^2 + \nu^2)} \approx \begin{cases} \frac{\omega_D^2}{12} \frac{\nu}{\Omega^3} & , \Omega \gg \nu, \omega_D \\ \frac{\omega_D^2}{12} \frac{1}{\nu \Omega} & , \nu \gg \Omega \gg \omega_D \end{cases}
\end{aligned}$$

So depending on the friction we have two different scalings, with the crossover happening at $\Omega \approx \nu$. Since we assumed $\Omega \gg \omega_D$ it follows that the intermediate regime $G''(\Omega) \sim \Omega^{-1}$ only appears if $\nu \gg \omega_D$, which is in agreement with our numerical results. To determine the behaviour at low frequencies we use the approximation (2.21) to evaluate the integral in (2.18). Since the result is rather long and not easy to read we gave the full expression in Appendix A.2. The dominant term for low Ω is:

$$\begin{aligned}
G''(\Omega) &\approx \frac{1}{2\omega_D} \sqrt{\frac{1}{2} (\Omega \sqrt{\Omega^2 + \nu^2} + \Omega^2)} \\
&\times \arctan 2 \left[\Omega \sqrt{\Omega^2 + \nu^2} - \omega_D^2, \omega_D \sqrt{2 (\Omega \sqrt{\Omega^2 + \nu^2} - \Omega^2)} \right]. \tag{2.24}
\end{aligned}$$

Here $\arctan2(x, y)$ denotes the angle ϕ of the complex number $z = x + iy$. The argument of $\arctan2$ has a singularity at $\Omega = \sqrt{(\sqrt{\nu^4 + 4\omega_D^4} - \nu^2)/2} \sim \omega_D$. The last equality holds true for low friction ν , in which case we get a sharp drop of G'' at that frequency. This drop coincides with an overshoot in $G'(\Omega)$ at the same frequency. For higher friction the drop is replaced by the $G''(\Omega) \sim \Omega^{-1}$ scaling found earlier. Finally we look at the low frequency limit $\Omega \ll \omega_D$ and get:

$$\begin{aligned}
 G''(\Omega \ll \omega_D) &\approx \frac{1}{2\omega_D} \sqrt{\frac{1}{2} (\Omega\sqrt{\Omega^2 + \nu^2} + \Omega^2)} \arctan2[-\omega_D^2, 0] \\
 &= \frac{\pi}{2\omega_D} \sqrt{\frac{1}{2} (\Omega\sqrt{\Omega^2 + \nu^2} + \Omega^2)} = \begin{cases} \frac{\pi}{2\omega_D} \sqrt{\frac{1}{2} \nu \Omega}, & \text{if } \Omega \ll \nu, \omega_D \\ \frac{\pi}{2\omega_D} \Omega, & \text{if } \nu \ll \Omega \ll \omega_D \end{cases} \quad (2.25)
 \end{aligned}$$

In the first line we used the fact that a negative real number has an angle $\phi = \pi$. Again, depending on the friction, we get two different scalings with the crossover at $\Omega \sim \nu/2$. Since we assumed $\Omega \ll \omega_D$, the $G''(\Omega) \sim \Omega$ scaling only appears for $\nu \ll \omega_D$. This also means that only one of the two scalings $G''(\Omega) \sim \Omega, \Omega^{-1}$ can be present at any given parameter combination, since the friction can only be larger or smaller than ω_D but not both at the same time.

In Fig. 2.12 we show the different scalings in comparison to the numerical results. As you can see we have very good agreement at $Z = 6$ for the scalings as well as for crossover frequencies. The deviation at very low frequencies is a finite size effect. Due to the limited size of our model systems the possible wavelength of phonon like excitations has an upper boundary, which is of the order of the system size, corresponding to a minimum frequency ω_{min} . We now look at $\Omega \ll \omega_{min}$, also assuming that $\nu \Omega \ll 1$, which allows us to rewrite the sum of (2.18) as:

$$\begin{aligned}
 G''(\Omega) &= \frac{1}{V} \sum_k \frac{\nu \Omega (\boldsymbol{\Xi} \cdot \hat{\mathbf{v}}_k)^2}{(\omega_k^2 - \Omega^2)^2 + \nu^2 \Omega^2} \\
 &\approx \frac{1}{V} \nu \Omega \sum_k \frac{(\boldsymbol{\Xi} \cdot \hat{\mathbf{v}}_k)^2}{\omega_k^4} \approx \nu \Omega. \quad (2.26)
 \end{aligned}$$

The exact prefactor depends on the individual system as the smallest eigenvalue depends on the type of disorder. From the crossover of this false scaling and the correct $G''(\Omega) \sim \Omega^{1/2}$ scaling we can estimate that our results for $G^*(\Omega)$ are only reliable above a certain threshold.

For coordination numbers away from the critical point we find that the high frequency scaling obtained from (2.23) still holds true, as the behaviour of $D(\omega)\Gamma(\omega)$ plays no role for the behaviour of $G^*(\Omega)$. For low driving frequencies Ω the situation is different as the approximation (2.21) no longer holds true for low eigenfrequencies ω . However we can use the Debye approximation $D(\omega) \sim \omega^2$ for systems above the isostatic point and $\Gamma(\omega) \sim \omega^2$ found by Zaccane [31] to estimate the low frequency scaling of $G''(\Omega)$:

$$G''(\Omega) \sim 3 \frac{N}{V} \int_0^{\omega_D} \frac{\nu \Omega \omega^4}{(\omega^2 - \Omega^2)^2 + \nu^2 \Omega^2} d\omega \sim \Omega. \quad (2.27)$$

As we can see the $G''(\Omega) \sim \Omega^{1/2}$ scaling disappears and we only get the linear scaling for low frequencies. This is in agreement with results found by Tighe [33, 34] and Yucht et. al [35], where the anomalous square root scaling was found close to the isostatic point both in effective medium calculations and simulations.

2.4 Summary

In this chapter we investigated different types of nearest neighbour spring networks. One key result is the comparison between the VDOS of a depleted fcc with a depleted random network which, despite of severe structural differences (see Fig. 2.5), show a striking similarity especially in the low frequency region, where the Boson peak anomaly appears. Furthermore we devised a new parameter based on inversion symmetry breaking that reflects the similarity of the systems observed in the VDOS. This demonstrates that rather the degree of inversion symmetry breaking rather than the pure geometric deviation from the fcc lattice structure (as measured by the widely used F_6 parameter) plays the crucial role in the vibrational properties of disordered systems.

As another key result we were able to show that various types of introduced disorder (regular depletion, random depletion, vacancies) in the fcc lattice do not

change the behaviour of the static shear modulus despite all three systems showing different connectivity structure. When approaching the isostatic point $Z = 6$ even the function $D(\omega)\Gamma(\omega)$ collapses onto one simple function that can be used to evaluate the complex modulus $G^*(\Omega)$ analytically. We then explored the different scalings in the complex modulus and were able to demonstrate that the change of the low frequency scaling of the imaginary part $G''(\Omega)$ from $\sim \Omega$ for $Z > 6$ to $\sim \Omega^{1/2}$ at $Z = 6$, which has been observed in simulations and effective medium calculations [33, 34, 35], can be traced back to the change in the vibrational spectrum. At the isostatic point the low frequency Debye-scaling $D(\omega) \sim \omega^2$ changes to $D(\omega) \sim 1$ which, combined with the unchanged scaling of the non-affine correlator $\Gamma(\omega) \sim \omega^2$, leads to a change in scaling of the combined function $D(\omega)\Gamma(\omega)$ from $\sim \omega^4$ to ω^2 . This change directly corresponds to the aforementioned change in the low frequency scaling of $G''(\Omega)$.

The framework we used here has of course several shortcomings of which the most problematic is the limited range of scalings for $G''(\Omega)$. By assuming a power law scaling for $D(\omega)\Gamma(\omega)$ we can evaluate (1.34) and find:

$$\begin{aligned}
 G''(\Omega) &= d \frac{N}{V} \int_0^\infty \frac{\nu D(\omega)\Gamma(\omega) \Omega}{m^2(\omega^2 - \Omega^2)^2 + \nu^2 \Omega^2} d\omega \rightarrow \int_0^\infty \frac{D(\omega)\Gamma(\omega) \Omega}{(\omega^2 - \Omega^2)^2 + \Omega^2} d\omega \\
 &= \int_0^\infty \frac{\omega^a \Omega}{(\omega^2 - \Omega^2)^2 + \Omega^2} d\omega \sim \Omega^b
 \end{aligned} \tag{2.28}$$

$$b = \begin{cases} -1 & , a \leq -1 \\ \frac{1}{2}(a-1) & , -1 < a < 1 \\ 1 & , a \geq 3 \end{cases}$$

As we can see the scaling of $G''(\Omega)$ is restricted to powers in the interval $[-1, 1]$ and is therefore not able to reproduce results outside this range.

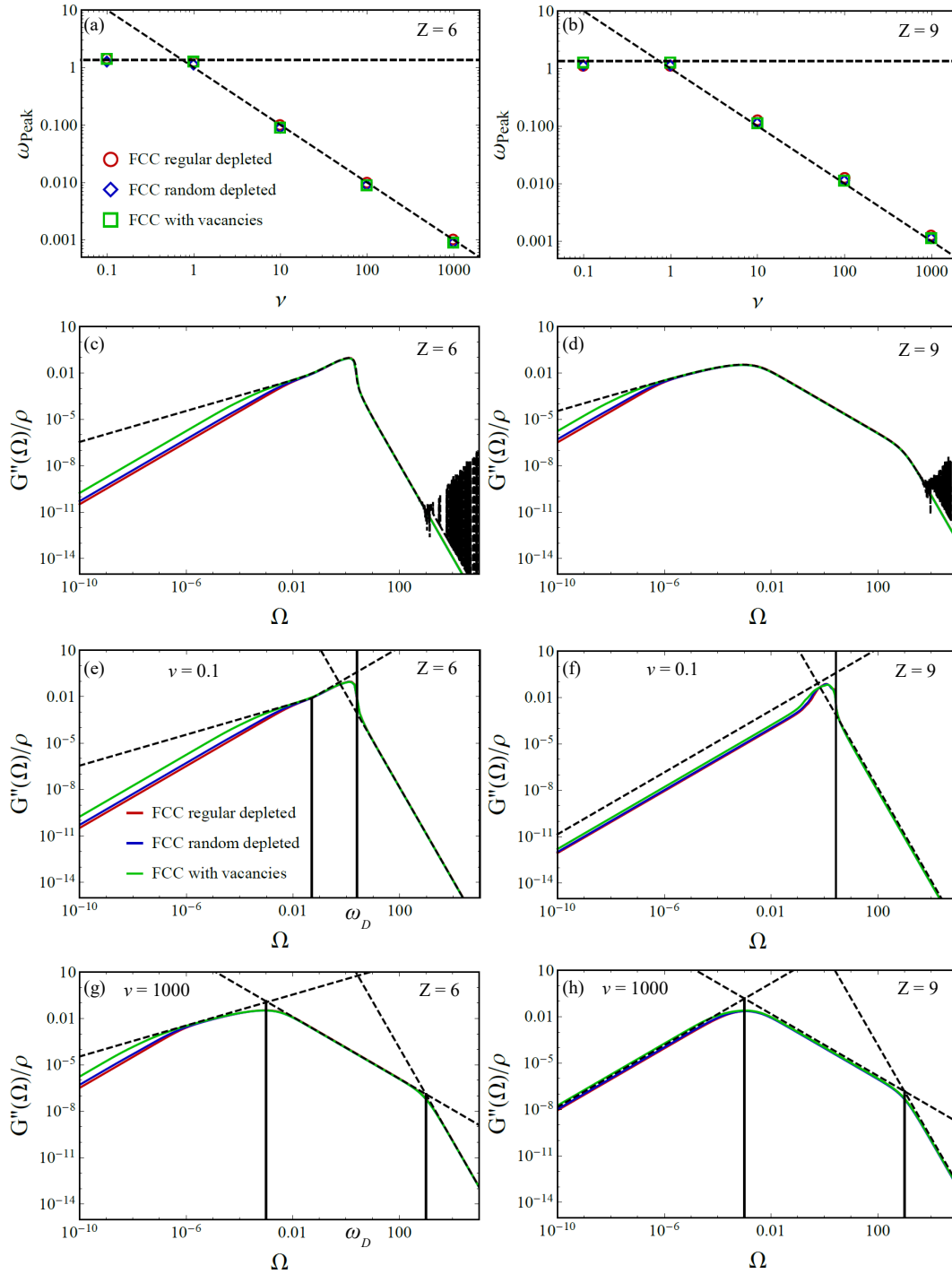


Figure 2.12: (a,b): scaling of the peak position in $G''(\Omega)$ with the friction ν . The numerical results are in agreement with the analytical estimate from (2.20). (c,d): Comparison between numerical results and the analytical function obtained by using our fit $D(\Omega)\Gamma(\Omega) \sim \omega^2(\omega_D - \omega)$. We see very good agreement up to the point where the numerical result breaks down due to finite size of the system and eigenvalue gap that follows from it. (e-h): Comparison of the scalings found in (2.23) and (2.25). Black lines show the crossover points as described in the text. We find very good agreement for all of the results.

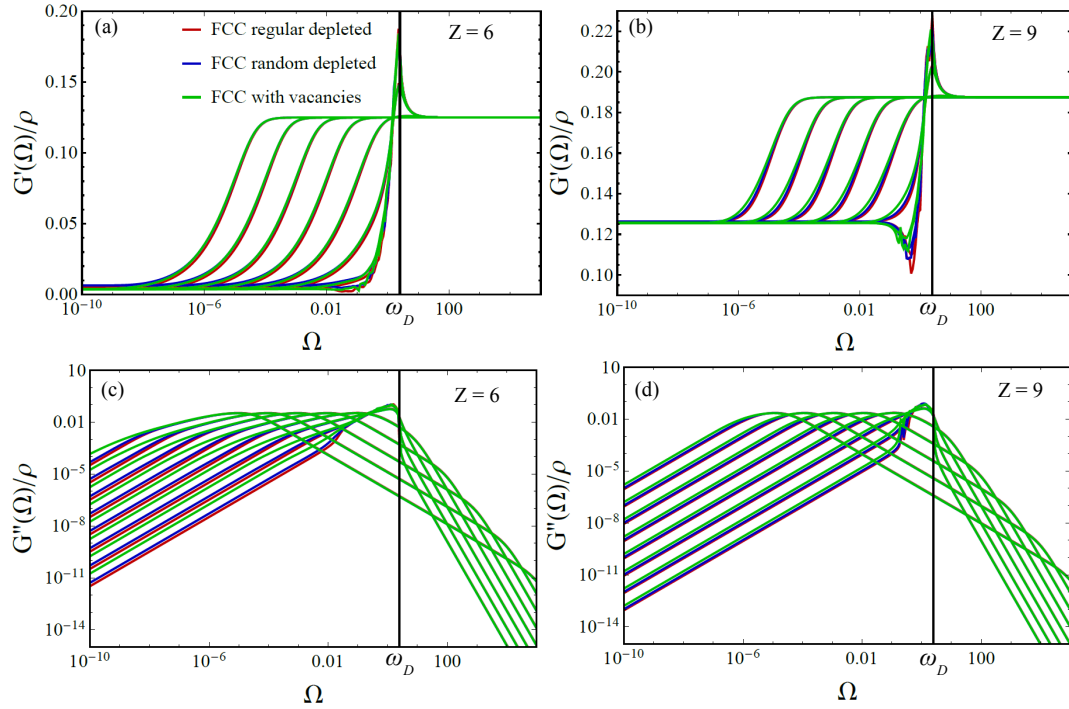


Figure 2.13: (a,b): $G'(\Omega)$ for frictions ranging from $\nu = 10^{-2}$ to $\nu = 10^5$ with stepsize being one order of magnitude (The transition at the lowest frequency belongs with $\nu = 10^5$). Above $\nu \sim \omega_D$ the friction has no impact on the shape of the curve but just shifts the transition to lower frequencies. We can see that an overshoot arises at $\Omega = \omega_D$ when the jump in $G''(\Omega)$ occurs. Again we can see the equality of all three fcc systems in $G'(0)$, $G'(\infty)$ and the transition in between. For $Z = 9$ differences appear due to the different behaviour of $D(\omega)\Gamma(\omega)$. (c,d): $G''(\Omega)$ for the same parameters as in (a,b). We can clearly see the disappearance of the sharp jump at $\Omega = \omega_D$ for $\nu > \omega_D$ as predicted in the text. In its place the $\Gamma''(\Omega) \sim \Omega^{-1}$ scaling arises and broadens with the friction. We can also see the presence of a $\Gamma''(\Omega) \sim \Omega^{1/2}$ scaling at the critical point, which is absent for $Z = 9$. In general the results are in agreement with all analytical findings related to the friction.

Lattices with long range correlations

In the following chapter we looked at the influence of long range interaction in depleted spring networks. Standard nearest neighbour spring networks are a very useful model to study the properties of disordered systems, but have shortcomings in capturing certain aspects that are observed e.g. in molecular dynamics (MD) simulations. One such quantity is the spatial autocorrelation of the local shear modulus. While nearest neighbour networks show only very short ranged spatial correlation, simulations with long range potentials show a long range spatial correlation decaying with a power law [36, 37, 38]. Since effective medium approximations often work with heterogeneous elasticity to implement disorder [39, 40], it is important how strong and over which range those heterogeneities correlate. The physical consequence of those heterogeneities is the scattering of phonons which e.g. leads to sound attenuation. In the case of uncorrelated scatterers the result is Rayleigh scattering, which leads to a sound attenuation $\sim -k^{d+1}$, where k is the phonon's wave vector and d the spatial dimension of the system. In the case of power law correlations between the scatterers this was found to change to $\sim -k^{d+1} \log k$ [37] as a result of anomalous scattering. The goal of this work, performed together with Johannes Krausser during his PhD at the University of Cambridge [41], is to extend the depleted lattice model from the chapter before to long range interaction and study the (spatial) correlation of various quantities related to the local shear modulus with the future goal to study this anomalous scattering of phonons in an easily controllable model system. We decided to use a two dimensional system in order to increase the number of particles and make it easier to visualize the results in two dimensional grids.

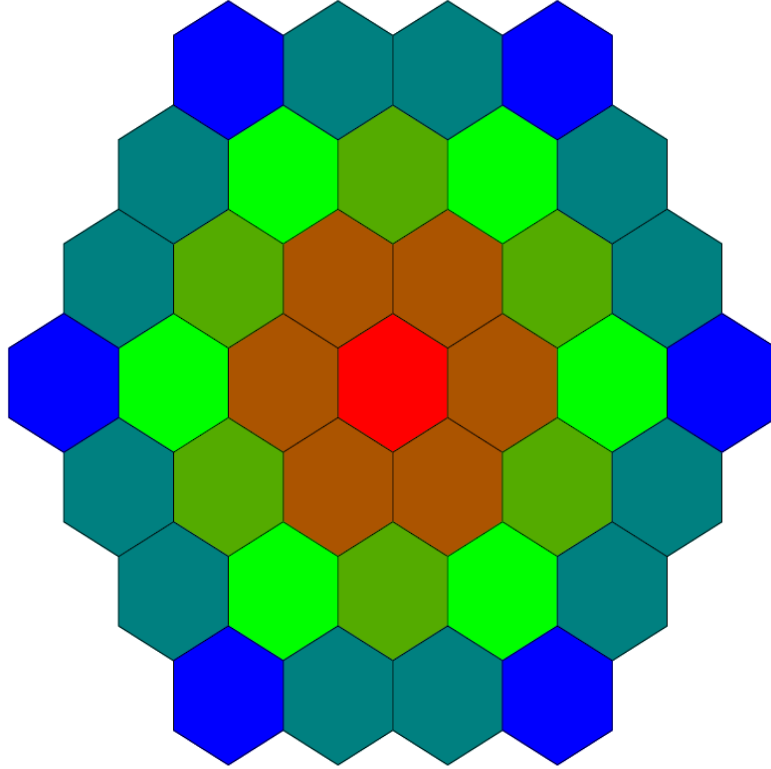


Figure 3.1: Shell structure of the triangular lattice. The first five shells are shown with the central site coloured red.

3.1 Model system

The model we are using is a random depleted triangular lattice as depicted in Fig. 3.1 and 3.2. Long range interactions are implemented by harmonic potentials with varying rest length r_0 and spring constant $\kappa(r_0)$ to avoid internal stresses and make the introduction of disorder by bond depletion possible and plausible. For a given system bonds are considered up to a cut-off radius R_c which, since we have a lattice system, corresponds to a maximum number of included shells S with $S = 1$ corresponding to the nearest neighbour system. In this work we study lattices with $S = 1, 2, 5, 15$ to give an overview over the influence of those long range springs on the spatial correlation in the system. Sketches of our systems are shown in Fig. 3.2. The potential for one shell reads:

$$U(r) = \frac{\kappa(r_0)}{2}(r - r_0)^2. \quad (3.1)$$

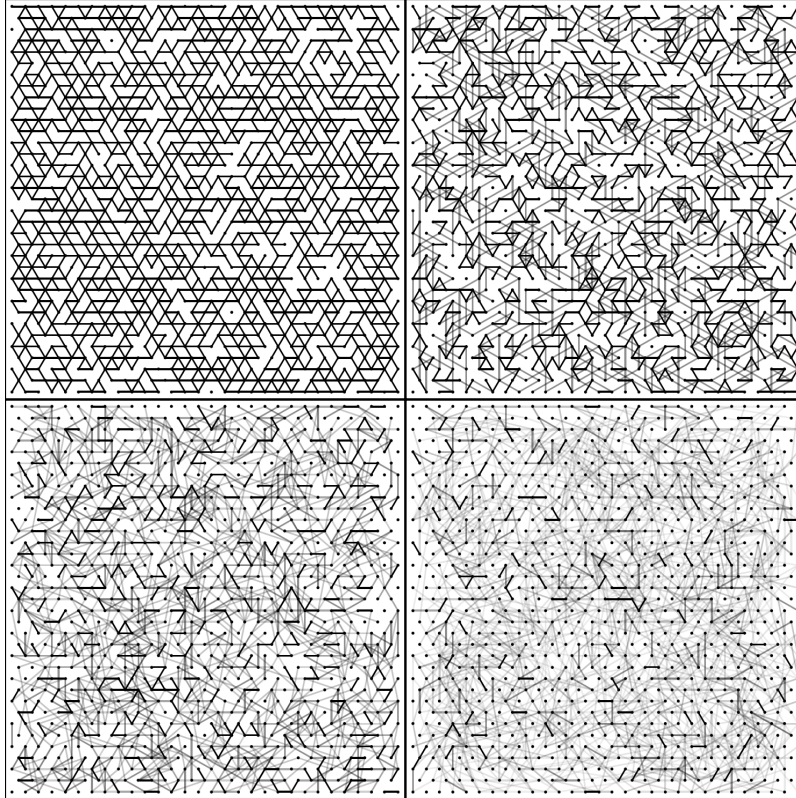


Figure 3.2: Model systems with $Z = 4$ and $S = 1, 2, 5, 15$ (from top left to bottom right). The relative opacity of bonds corresponds to the relative spring constant.

In this work we will restrict ourselves to power law decay of the spring constant $\kappa(r_0) \sim r_0^a$. The system is depleted randomly, meaning that each bond has a certain bond probability p for existing and $(1-p)$ for being broken. The resulting average coordination number depends on the total number of bonds Z_m available, which in turn depends on the number of shells involved or the range of interaction considered. In general it can be calculated as for the random depleted fcc:

$$Z = \sum_{z=0}^{Z_m} z \binom{Z_m}{z} (1-p)^z p^{Z_m-z} = Z_m (1-p). \quad (3.2)$$

The critical connectivity $Z^* = 2d = 4$ (see (2.1)) does neither depend on the number of shells involved nor the decay of the spring constant. Since we use the bond probability p as one main parameter it is convenient to introduce the critical

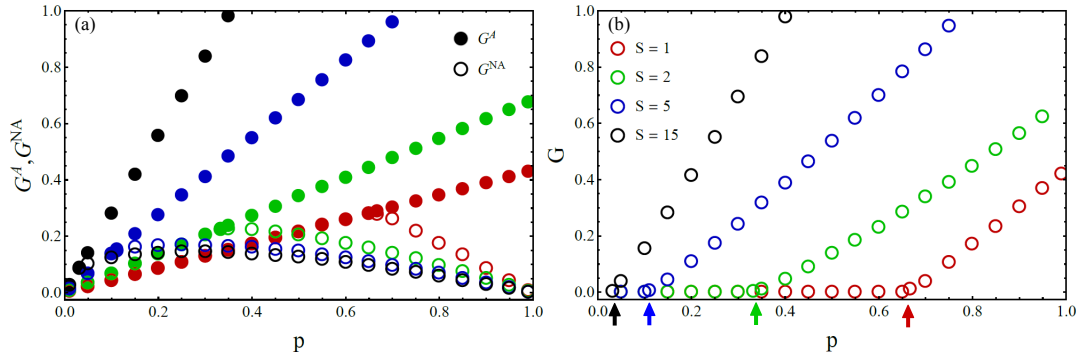


Figure 3.3: (a): Affine and non-affine part of the shear modulus. (b): Total shear modulus G in dependence of the bond probability p . The theoretical critical bond probabilities are indicated by correspondingly coloured arrows. As we can see the shear modulus actually goes to zero at those values, which verifies our theoretical prediction.

bond occupancy p^* :

$$p^* = \frac{4}{Z_m}. \quad (3.3)$$

To verify (3.3) we have calculated the shear modulus for different bond probabilities and shells $S = 1, 2, 5, 15$. The results are shown in Fig. 3.3 in dependence of p , with $Z_m(1) = 6$, $Z_m(2) = 12$, $Z_m(5) = 36$, $Z_m(15) = 126$. As predicted the critical point lies at $p^* = 4/Z_m$, which gives the explicit critical bond probabilities $p^*(S)$: $p^*(1) = 2/3$, $p^*(2) = 1/3$, $p^*(5) = 1/9$, $p^*(15) = 2/63$.

3.1.1 Local shear modulus

We used the formalism derived in Chap. 1 to calculate the affine and non-affine part of the shear modulus. To study spatial correlation of the shear modulus G it is necessary to first define the quantity locally. The complete affine part can be calculated using (2.13) since we only have pair bonds at rest. The contribution from particle i is calculated straightforwardly by considering only bonds connected to i . As each bond connects two sites its contribution is split among both sites

equally, adding a factor of 1/2:

$$G_i^A = \frac{1}{2V} \sum_{j=1}^{Z_i} \kappa(r_{ij}) (r_{ij} \hat{n}_{ij}^x \hat{n}_{ij}^y)^2 = \frac{1}{2V} \sum_{j=1}^{Z_i} \kappa_{ij} (r_{ij} \hat{n}_{ij}^x \hat{n}_{ij}^y)^2. \quad (3.4)$$

The spring constant κ_{ij} and bond length r_{ij} are included in the sum to account for the existence of bonds with different lengths and varying spring constant in the system. To define the non-affine part locally we look at the displacements $\delta \mathbf{r}$ (1.14) that govern the non-affine relaxation. The local displacement of particle i is obtained by considering the corresponding components of the normal mode expansion from (1.18) of (1.14):

$$\left. \frac{\mathcal{D}\mathbf{r}}{\mathcal{D}\gamma} \right|_{\gamma \rightarrow 0} = \delta \mathbf{r} = \mathbf{H}^{-1} \Xi = \sum_k \frac{\Xi \cdot \hat{\mathbf{v}}_k}{\lambda_k} \hat{\mathbf{v}}_k \quad (3.5)$$

$$\delta \vec{r}_i = \sum_k \frac{\Xi \cdot \hat{\mathbf{v}}_k}{\lambda_k} \hat{v}_{k,i}.$$

Here $\hat{v}_{k,i}$ is the d -dimensional component of the eigenvector $\hat{\mathbf{v}}_k$ belonging to particle i . We follow (1.18) further to calculate the local non-affine modulus:

$$G^{NA} = \frac{1}{V} \Xi \mathbf{H}^{-1} \Xi = \frac{1}{V} \Xi \cdot \delta \mathbf{r} = \sum_{i=1}^N \frac{1}{V} \vec{\Xi}_i \cdot \delta \vec{r}_i = \sum_{i=1}^N G_i^{NA} \quad (3.6)$$

$$G_i^{NA} = \frac{1}{V} \vec{\Xi}_i \cdot \delta \vec{r}_i = \frac{1}{V} \sum_k \frac{\Xi \cdot \hat{\mathbf{v}}_k}{\lambda_k} (\vec{\Xi}_i \cdot \hat{v}_{k,i}).$$

It is important to note that G_i^{NA} is, unlike G_i^A , not a completely local quantity as it involves the affine force field Ξ as well as the eigenvalues and eigenvectors of the whole system. This however reflects the physical meaning of the non-affine relaxation as it is a collective reorganisation of the system. It still make sense to speak of the local non-affine modulus as G_i^{NA} describes the modulus related to the energy of deformation released by particle i through its non-affine displacement. The total local shear modulus is just the difference of affine and non-affine part,

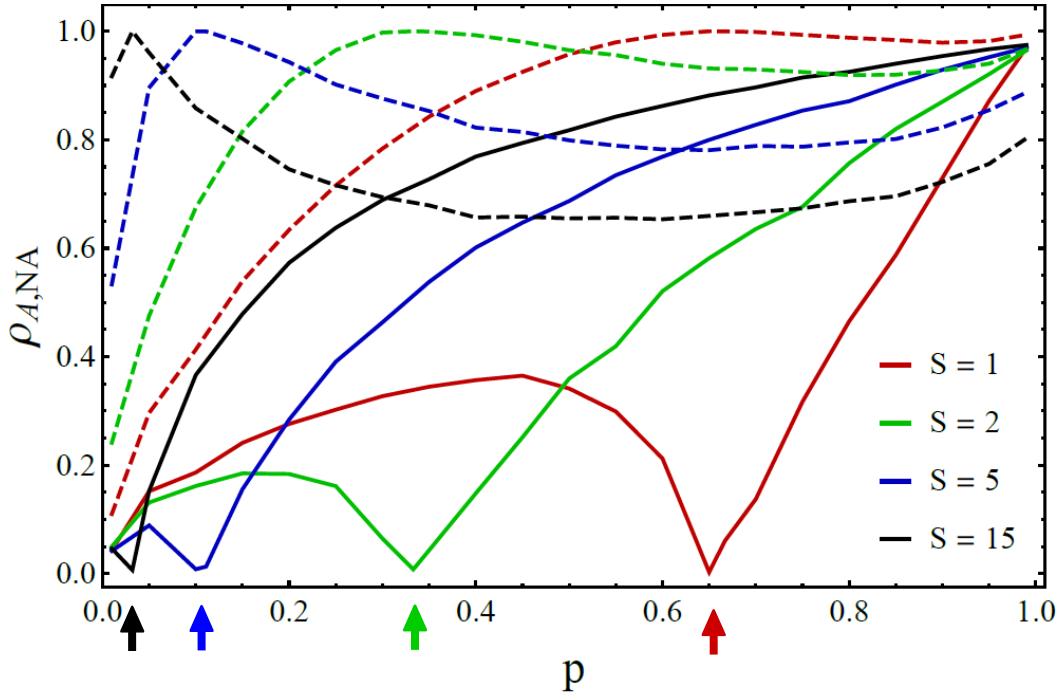


Figure 3.4: Correlation coefficients ρ_A, ρ_{NA} in dependence of p . Dashed lines show $-\rho_{NA}$ while solid lines show ρ_A . The critical bond probabilities are indicated by correspondingly coloured arrows. As we can see $\rho_{NA} = -1$ at the critical point. While ρ_A goes to 1 at $p = 1$, ρ_{NA} approaches lower values depending on the interaction length.

as described before:

$$G_i = G_i^A - G_i^{NA}. \quad (3.7)$$

A similar definition is used for thermal systems using the stress fluctuation instead of the affine force field [42].

3.1.2 Correlation between local G and G^A, G^{NA}

As we can see in Fig. 3.3 the affine part of the shear modulus is always larger or equal to the non-affine part, when calculated for the whole system. This however does not reflect the local behaviour. It is a well known phenomenon that the fluctuations of the non-affine displacement field $\delta \mathbf{r}$ diverge at the critical point [43], which leads to local G^{NA} showing the same behaviour. The affine part shows no

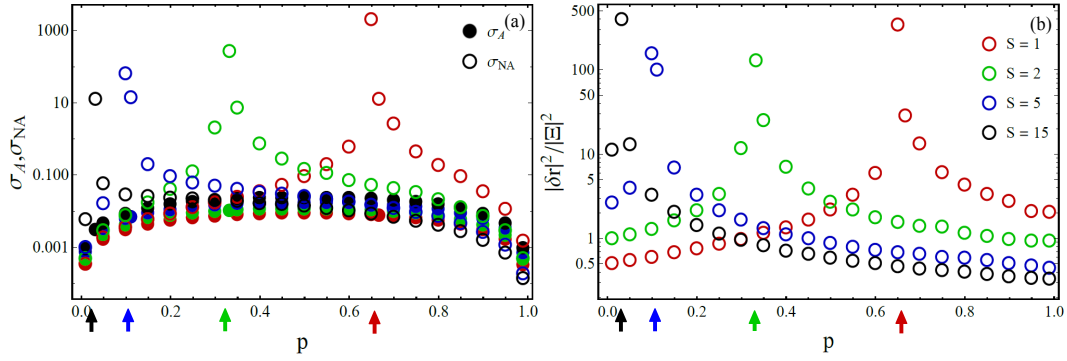


Figure 3.5: (a): Standard deviation of G^A, G^{NA} in dependence of p . The critical bond probabilities are indicated by correspondingly coloured arrows. As we can see the non-affine fluctuations diverge at p^* , while the affine fluctuations are small. (b): Ratio of the non-affine displacement field $\delta\mathbf{r}$ and the affine force field Ξ . The ratio diverges at the critical point and decays for higher p . We also observe smaller values for higher shells at a given p .

such divergence, which leads the shear modulus to be locally dominated by its non-affine part, although when summed up G^A and G^{NA} have equal value. To study the local dependence we calculate the correlation coefficients ρ_A, ρ_{NA} (3.8) between the local shear modulus and its affine and non-affine part. By comparing the two we see if the affine or non-affine contribution is dominant. The results are shown in Fig. 3.4. Since the non-affine part enters negatively in the calculation of G , ρ_{NA} is negative. As we are interested in the strength of the correlation we show the negative correlation coefficient to make it more easily comparable with the affine one. As we can see the correlation is sensitive to the bond probability. At the critical point, indicated by arrows, the local shear modulus anti-correlates completely with its non-affine part due to the divergence of the fluctuations.

As the local non-affine modulus is proportional to $\delta\mathbf{r}$ this leads to a strongly fluctuating G_i^{NA} as can be seen in Fig. 3.5. This behaviour is not mirrored by the affine part, which is why the local shear modulus is dominated by its non-affine part. With increasing p those fluctuations decrease and the correlation between G_i and its affine part increases, leading to a crossover between the absolute value of the two correlation coefficients for $S = 5, 15$. For $S = 1, 2$ this crossover happens at $p = 1$, where the concept of spatial correlation is meaningless as all sites have the same shear modulus. Taking this result into account we will study three different regimes of p : (i) high p , where $\rho_A > \rho_{NA}$ for $S = 5, 15$ and $\rho_A \approx \rho_{NA} \approx 1$

for $S = 1, 2$, (ii) the critical point p^* , where $\rho_A = 0$ and $\rho_{NA} = -1$ and (iii) intermediate p , where $\rho_A \approx \rho_{NA} < 1$.

3.2 Spatial correlation function

Next we will look at the spatial correlation function $C(r)$. It is a distance dependent expansion of the Pearson correlation coefficient ρ_{xy} that measures how close two quantities x and y , represented by a group of N points (x_i, y_i) , are to a linear dependence. It is defined as:

$$\rho_{xy} = \frac{\langle x_i y_i \rangle - \langle x \rangle \langle y \rangle}{\sqrt{(\langle x^2 \rangle - \langle x \rangle^2)(\langle y^2 \rangle - \langle y \rangle^2)}} \quad (3.8)$$

$$\langle x^n \rangle = \frac{1}{N} \sum_{i=1}^N x_i^n \quad ; \quad \langle y^n \rangle = \frac{1}{N} \sum_{i=1}^N y_i^n \quad ; \quad \langle x_i y_i \rangle = \frac{1}{N} \sum_{i=1}^N x_i y_i .$$

The value $\rho_{xy} = \pm 1$ means that all points (x_i, y_i) lie on the line $y = \pm m x + t$ and knowing one immediately determines the other. Values $|\rho_{xy}| < 1$ lead to uncertainty in this relation, which means that knowing one quantity only gives a general idea, depending on ρ_{xy} , of the value of the other quantity, with the limit being $\rho_{xy} = 0$, where the quantities are uncorrelated and no conclusions are possible. We are interested in the correlation of local shear modulus G at two different sites i and j , separated by the distance r . Therefore we consider all pairs (G_i, G_j) with $r_{ij} = r$ and calculate the correlation coefficient. Since the shells, and hence r_{ij} , are not equally spaced, we consider the interval $r_{ij} \in [r, r + dr]$ to get a smooth spatial correlation function $C(r)$:

$$C(r) = \rho_{G_i G_j} \Big|_{r_{ij} \in [r, r+dr]} = \frac{\langle G_i G_j \rangle - \langle G_i \rangle \langle G_j \rangle}{\sqrt{(\langle G_i^2 \rangle - \langle G_i \rangle^2)(\langle G_j^2 \rangle - \langle G_j \rangle^2)}} \Big|_{r_{ij} \in [r, r+dr]} . \quad (3.9)$$

The averages here are to be taken over the number of pairs $r_{ij} \in [r, r + dr]$ and not the number of particles N . To deal with the averages we go back one step and consider only pairs in a certain shell S with $r_{ij} = r_S$. Since our system is a perfect triangular lattice, all sites have the same number of neighbours Z_S with distance

r_S from them. It is important to note that the pairs here must not be confused with bonds used to calculate the local shear modulus in (3.7). The pairs are used to calculate the spatial correlation of the shear modulus and are an inherent quantity of the base lattice the sites are located on. Since we are not removing any particles in this work, there are always all possible pairs apparent and any summation over pairs is not affected by bond depletion. The total number of pairs with $r_{ij} = r_S$ is therefore $NZ_S/2$ which leads to:

$$\begin{aligned} \langle G_i^n \rangle &= \frac{2}{NZ_S} \sum_{ij} G_i^n \Big|_{r_{ij}=r_S} = \frac{2}{NZ_S} \frac{1}{2} \sum_{i=1}^N \sum_{j=1}^{Z_S} G_i^n \\ &= \frac{1}{NZ_S} \sum_{i=1}^N Z_S G_i^n = \frac{1}{N} \sum_{i=1}^N G_i^n. \end{aligned} \quad (3.10)$$

The factor $1/2$ comes from the double counting of pairs that happens by splitting the sum in the second step. Since (3.10) holds true for arbitrary combinations of shells S we can verify that the average over pairs with a given distance is actually the same as just the average value. Since G_i and G_j are interchangeable we can write:

$$\langle G_i^n \rangle = \langle G_j^n \rangle = \langle G^n \rangle. \quad (3.11)$$

With that we can write the spatial correlation function for one shell S as:

$$C_S = \frac{\langle G_i G_j \rangle - \langle G \rangle^2}{\langle G^2 \rangle - \langle G \rangle^2} \Big|_{r_{ij}=r_S}. \quad (3.12)$$

For the case of the affine shear modulus G^A we can simplify this expression further, by using that G^A is just a simple sum of contributions from single bonds in the system. We first split the local affine shear modulus in contributions from all

shells up to the cutoff radius R_c corresponding to S_c :

$$\begin{aligned}
G_i^A &= \sum_{r=1}^{S_c} G_{i,r}^A \\
\langle (G^A)^2 \rangle - \langle G^A \rangle^2 &= \frac{1}{N} \sum_{i=1}^N G_i^2 - \left(\frac{1}{N} \sum_{i=1}^N G_i^A \right)^2 \\
&= \frac{1}{N} \sum_{i=1}^N \left(\sum_{r=1}^{S_c} G_{i,r}^A \right)^2 - \left(\frac{1}{N} \sum_{i=1}^N \sum_{r=1}^{S_c} G_{i,r}^A \right)^2 \\
&= \sum_{r=1}^{S_c} \frac{1}{N} \sum_{i=1}^N (G_{i,r}^A)^2 + \sum_{r \neq r'} \frac{1}{N} \sum_{i=1}^N G_{i,r}^A G_{i,r'}^A - \left(\sum_{r=1}^{S_c} \frac{1}{N} \sum_{i=1}^N G_{i,r}^A \right)^2 \\
&= \sum_{r=1}^{S_c} \langle (G_r^A)^2 \rangle + \sum_{r \neq r'} \langle G_r^A \rangle \langle G_{r'}^A \rangle - \left(\sum_{r=1}^{S_c} \langle (G_r^A)^2 \rangle + \sum_{r \neq r'} \langle G_r^A \rangle \langle G_{r'}^A \rangle \right) \\
&= \sum_{r=1}^{S_c} \left(\langle (G_r^A)^2 \rangle - \langle G_r^A \rangle^2 \right).
\end{aligned} \tag{3.13}$$

Hereby we used the fact that the contribution to the shear modulus of one shell $G_{i,s}$ is independent of the contribution from another shell $G_{i,s'}$. This is due to the fact that bonds are depleted independently of another and with the same probability for all shells. The last term we have to analyse is the numerator of

(3.12). We will for once restrict the calculation to one shell S :

$$\begin{aligned}
\langle G_i^A G_j^A \rangle - \langle G \rangle^2 \Big|_{r_{ij}=r_S} &= \frac{2}{NZ_S} \sum_{ij} G_i^A G_j^A - \left(\frac{1}{N} \sum_{i=1}^N G_i^A \right)^2 \\
&= \frac{1}{NZ_S} \sum_{i=1}^N \sum_{j=1}^{Z_S} G_i^A G_j^A - \left(\frac{1}{N} \sum_{i=1}^N \sum_{r=1}^{S_c} G_{i,r}^A \right)^2 \\
&= \frac{1}{NZ_S} \sum_{i=1}^N \sum_{j=1}^{Z_S} \left(\sum_{r=1}^{S_c} G_{i,r}^A \right) \left(\sum_{r=1}^{S_c} G_{j,r}^A \right) - \left(\sum_{r=1}^{S_c} \frac{1}{N} \sum_{i=1}^N G_{i,r}^A \right)^2 \\
&= \frac{1}{NZ_S} \sum_{i=1}^N \sum_{j=1}^{Z_S} \left(G_{i,S}^A G_{j,S}^A + \sum_{r,r' \neq S} G_{i,r}^A G_{j,r'}^A \right) - \left(\sum_{r=1}^{S_c} \langle G_r^A \rangle \right)^2.
\end{aligned} \tag{3.14}$$

To understand the split in $r = S$ and $r, r' \neq S$ we take a moment to think about how correlations between different sites can be created in our model. In general correlation between two sites i and j can be introduced by something that, if changed, changes the values at both sites simultaneously. One way of doing this is to have a bond between the two sites, which would influence G^A at both sites if changed or removed. As we are interested in correlations at the distance of a certain shell S it makes sense to treat the contributions $G_{i,S}^A$ and $G_{j,S}^A$ special as they contain exactly those bonds that connect i and j . Another way of introducing correlation could be a site k that has a bond both to i and j . If this site would be displaced or removed it would change the shear modulus at both sites simultaneously, which would introduce correlation. We can ignore this, since we restrict ourselves to bond depletion for introducing disorder and removing the bond r_{ik} does not change G_j^A . Correlation for G^A is therefore only introduced if two sites share a bond, which means for a given shell S only contributions from this shell can contribute to the spatial correlation function. We continue to simplify

the above expression:

$$\begin{aligned}
& \langle G_i^A G_j^A \rangle - \langle G \rangle^2 \Big|_{r_{ij}=r_S} \\
&= \frac{1}{N Z_S} \sum_{i=1}^N \sum_{j=1}^{Z_S} \left(G_{i,S}^A G_{j,S}^A + \sum_{r,r' \neq S} G_{i,r}^A G_{j,r'}^A \right) - \left(\sum_{r=1}^{S_c} \langle G_r^A \rangle \right)^2 \\
&= \langle G_{i,S}^A G_{j,S}^A \rangle + \frac{1}{N Z_S} \sum_{i=1}^N \sum_{j=1}^{Z_S} \sum_{r,r' \neq S} G_{i,r}^A G_{j,r'}^A - \left(\langle G_S^A \rangle^2 + \sum_{r,r' \neq S} \langle G_r^A \rangle \langle G_{r'}^A \rangle \right) \quad (3.15) \\
&= \langle G_{i,S}^A G_{j,S}^A \rangle - \langle G_S^A \rangle^2 + \sum_{r,r' \neq S} \frac{2}{N Z_S} \sum_{ij} G_{i,r}^A G_{j,r'}^A - \sum_{r,r' \neq S} \langle G_r^A \rangle \langle G_{r'}^A \rangle \\
&= \langle G_{i,S}^A G_{j,S}^A \rangle - \langle G_S^A \rangle^2.
\end{aligned}$$

Now we only have to consider one shell, which allows us to further decompose $G_{i,S}^A$ into contributions from single bonds. One crucial point is that each bond contributing to $G_{i,S}^A$ also contributes to one of its bond neighbours in shell S . By summing over all bond neighbours of site i we count every contribution to $G_{i,S}^A$ exactly once:

$$\sum_{j=1}^{Z_S} G_{j,S}^A = G_{i,S}^A + \mathcal{R}_S. \quad (3.16)$$

The rest \mathcal{R}_S is the sum of remaining bonds in shell S . Since bonds are depleted independently of each other the summed contribution of the remaining bonds is independent of the value of $G_{i,S}^A$. Independently of the bond probability they will form $Z_S - 1$ sets of G_S^A (although not $G_{i,S}^A$!) and therefore have the average value

$\langle \mathcal{R}_S \rangle = (Z_S - 1) \langle G_S^A \rangle$. We can write:

$$\begin{aligned}
& \langle G_i^A G_j^A \rangle - \langle G \rangle^2 \Big|_{r_{ij}=r_S} \\
&= \langle G_{i,S}^A G_{j,S}^A \rangle - \langle G_S^A \rangle^2 = \frac{1}{NZ_S} \sum_{i=1}^N \sum_{j=1}^{Z_S} G_{i,S}^A G_{j,S}^A - \langle G_S^A \rangle^2 \\
&= \frac{1}{NZ_S} \sum_{i=1}^N G_{i,S}^A \sum_{j=1}^{Z_S} G_{j,S}^A - \langle G_S^A \rangle^2 = \frac{1}{NZ_S} \sum_{i=1}^N G_{i,S}^A [G_{i,S}^A + \mathcal{R}_S] - \langle G_S^A \rangle^2 \\
&= \frac{1}{NZ_S} \sum_{i=1}^N G_{i,S}^A \sum_{j=1}^{Z_S} G_{j,S}^A - \langle G_S^A \rangle^2 = \frac{1}{Z_S} \left[\langle (G_S^A)^2 \rangle + \langle G_S^A \rangle \langle \mathcal{R}_S \rangle \right] - \langle G_S^A \rangle^2 \\
&= \frac{1}{Z_S} \left[\langle (G_S^A)^2 \rangle + (Z_S - 1) \langle G_S^A \rangle^2 - Z_S \langle G_S^A \rangle^2 \right] \\
&= \frac{1}{Z_S} \left[\langle (G_S^A)^2 \rangle - \langle G_S^A \rangle^2 \right].
\end{aligned} \tag{3.17}$$

We can trace back the correlation of G^A for a given shell S to the fluctuation in the contribution from this shell. This immediately makes clear that there will be no correlations in the affine shear modulus for $r > R_c$. The total correlation function for G^A at shell S reads:

$$C_S = \frac{\langle G_i^A G_j^A \rangle - \langle G^A \rangle^2}{\langle (G^A)^2 \rangle - \langle G^A \rangle^2} \Big|_{r_{ij}=r_S} = \frac{1}{Z_S} \frac{\langle (G_S^A)^2 \rangle - \langle G_S^A \rangle^2}{\sum_{r=1}^{S_c} [\langle (G_r^A)^2 \rangle - \langle G_r^A \rangle^2]}. \tag{3.18}$$

When looking at long distances in the triangular lattice, the spacing between individual shells becomes very small, leading to an increasing number of bonds for a given interval $[r, r + \delta r]$. Those bonds approach an isotropic angle distribution, which is why we can make a long range approximation for the scaling of (3.18). We therefore assume an isotropic distribution of bonds on a circle C_j around a site i with radius r . Each bond contributes $\frac{1}{2V} \kappa(r) (r \hat{n}_{ij}^x \hat{n}_{ij}^y)^2$ according to (3.4), with j being an arbitrary site on the circle C_j . As we have a two dimensional system, we can switch to polar coordinates $\hat{n} = (\cos \phi, \sin \phi)$, which simplify the calculation.

We are only interested in the scaling of $C(r)$ so only the numerator of (3.18) and $Z_S = Z_{max}(r)$ has to be considered. The components can be calculated as:

$$\begin{aligned}
\langle G^A(r) \rangle &= \frac{1}{2V} \frac{1}{N} \sum_{i=1}^N \sum_{j=1}^{Z_i(r)} \kappa r^2 (\cos \phi_j \sin \phi_j)^2 = \\
&= \frac{r^2 \kappa}{2V} \frac{1}{N} \sum_{i=1}^N \sum_{j=1}^{Z_i(r)} (\cos \phi_j \sin \phi_j)^2 \\
&\xrightarrow{r \gg 1} \frac{r^2 \kappa}{2V} \frac{1}{N} \sum_{i=1}^N Z_i(r) \int_0^{2\pi} \frac{1}{2\pi} (\cos \phi \sin \phi)^2 d\phi \\
&= \frac{r^2 \kappa}{16V} \frac{1}{N} \sum_{i=1}^N Z_i(r) = \frac{r^2 \kappa}{16V} \langle Z(r) \rangle.
\end{aligned} \tag{3.19}$$

Here $Z_i(r)$ denotes the actual number of bonds to the circle of radius r around site i . Since we now are explicitly calculating G^A we have to consider the bond probability p and the varying Z_i it is causing. The second moment of $G_i^A(r)$ is a bit more lengthy but can be calculated in the same way:

$$\begin{aligned}
\langle (G^A(r))^2 \rangle &= \frac{1}{N} \sum_{i=1}^N \left[\frac{1}{2V} \sum_{j=1}^{Z_i(r)} \kappa r^2 (\cos \phi_j \sin \phi_j)^2 \right]^2 = \\
&= \frac{r^4 \kappa^2}{4V^2} \frac{1}{N} \sum_{i=1}^N \left[\sum_{j=1}^{Z_i(r)} (\cos \phi_j \sin \phi_j)^2 \right]^2 \\
&\xrightarrow{r \gg 1} \frac{r^4 \kappa^2}{4V^2} \frac{1}{N} \sum_{i=1}^N Z_i^2(r) \left[\int_0^{2\pi} \frac{1}{2\pi} (\cos \phi \sin \phi)^2 d\phi \right]^2 \\
&= \frac{r^4 \kappa^2}{256V^2} \frac{1}{N} \sum_{i=1}^N Z_i^2(r) = \frac{r^4 \kappa^2}{256V^2} \langle Z^2(r) \rangle.
\end{aligned} \tag{3.20}$$

By inserting (3.20) and (3.19) into (3.18) we get:

$$\begin{aligned}
C(r) &\sim \frac{1}{Z_{max}(r)} [\langle (G^A(r))^2 \rangle - \langle G^A(r) \rangle^2] \\
&= \frac{1}{Z_{max}(r)} \left[\frac{r^4 \kappa^2}{256V^2} \langle Z^2(r) \rangle - \left(\frac{r^2 \kappa}{16V} \langle Z(r) \rangle \right)^2 \right] \\
&= \frac{r^4 \kappa^2}{256V^2} \frac{1}{Z_{max}(r)} [\langle Z^2(r) \rangle - \langle Z(r) \rangle^2] = \frac{r^4 \kappa^2}{256V^2} \frac{Z_{max}(r) p(1-p)}{Z_{max}(r)} \quad (3.21) \\
&= \frac{r^4 \kappa^2}{256V^2} p(1-p) \\
&\rightarrow C(r) \sim r^4 \kappa^2.
\end{aligned}$$

In the third line we used the distribution of Z from (2.8) to compute the variance. We can ignore the factor $p(1-p)$ as it cancels with the denominator from (3.18), which has the same structure as the numerator and also produces a factor $p(1-p)$. Aside from that the numerator gives only a constant number as it contains the sum over all shells. In recent work a correlation function $C(r) \sim r^{-2}$ was discovered in simulations of central force glasses [36, 37, 38]. To make our results comparable we chose a power law decay of $\kappa \sim r^{-3}$, which gives us $C(r) \sim r^{4-6} = r^{-2}$ for the affine shear modulus. Although the total shear modulus involves also the non-affine part, for which no such scaling argument exists, the scaling for G^A still holds importance as it will be dominant for high bond probability and long range bonds where the non-affine part contributes small values.

3.3 Numerical results for $C(r)$

We have calculated $C(r)$ numerically for $S = 1, 2, 5, 15$ by calculating the value for each shell according to (3.12) and then averaged over values of $r_S \in [r, r + \delta r]$ to create a list with equidistant values of r . To reduce the numerical error we averaged each system over 100 different realizations.

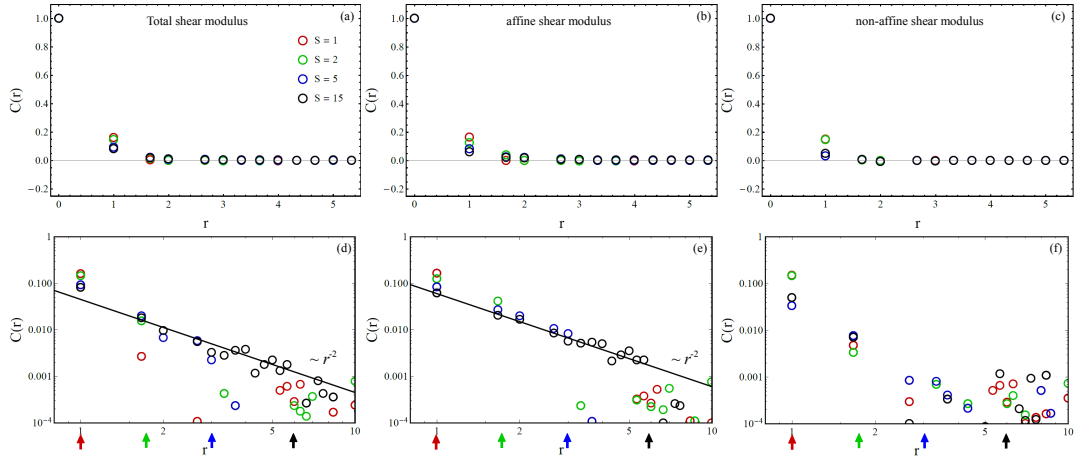


Figure 3.6: Spatial correlation function of G (a), G^A (b) and G^{NA} (c) for high bond probability p with logarithmic plots shown below. Arrows indicate the maximal interaction length R_c of the corresponding system. As we can see G^A and G follow the predicted $C(r) \sim r^{-2}$ power law for $r < R_c$, while G^{NA} decorrelates at shorter distances.

3.3.1 High bond probability p

First we looked at systems with high bond probability p far away from p^* , where $\rho_A > \rho_{NA}$. We considered $p = 0.85$ as sufficiently large for $S = 5, 15$. For $S = 1, 2$ we chose $p = 0.99$ to represent the regime where $\rho_A \approx \rho_{NA} \approx 1$, as there is no crossover between the two correlation coefficients in this case. The results are shown in Fig. 3.4. As one can see the correlation of G^A follows the predicted power law $C(r) \sim r^{-2}$ with the correlation length being equal to the cutoff radius of the interaction as indicated by the coloured arrows. G^{NA} shows no correlation beyond $r \approx 1$ for any interaction length at high bond probability. The correlation of G matches the behaviour for G^A .

This is in agreement with our expectation from the analysis of the correlation between the local G_i and G_i^A, G_i^{NA} as shown in Fig. 3.6. At high p the local shear modulus correlates with the affine rather than with the non-affine part for $S = 5, 15$, which explains why we observe a similar correlation function for G and G^A . Although the correlations ρ_A, ρ_{NA} have similar strength for $S = 1, 2$, we still observe a correlation function $C(r)$ close to the affine prediction.

In order to get further insight into the correlation of the shear modulus we will examine the spatial structure of the correlation. To do that we calculate all values $C(r_{ij})$ for one site i and write them into the corresponding sites j . This gives us

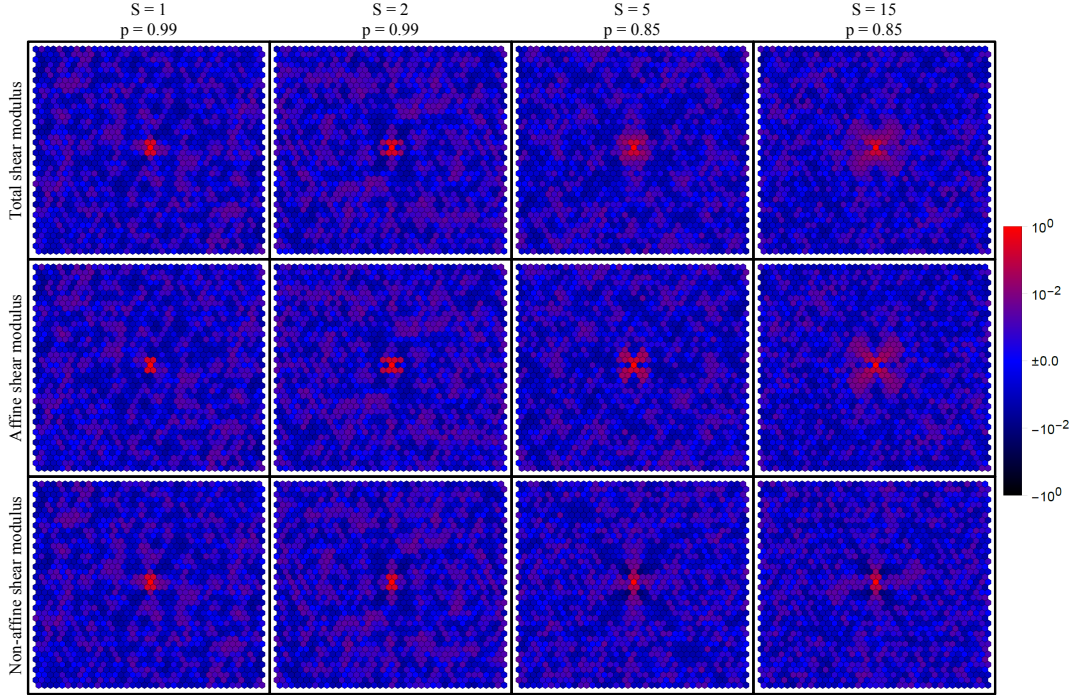


Figure 3.7: Two dimensional maps corresponding to $C(r)$ shown in Fig. 3.6. We can see the extending lobe structure for higher shells as well as the similar behaviour of G and G^A stemming from the high correlation between the two quantities.

a spatial map of correlations values. To average over the system we repeat this for all sites i and overlay the resulting maps so that particle i is always located at the centre. Afterwards we average again over 100 different realisations. The results are shown in Fig. 3.7. For G^A the correlation has a clear lobe structure whose range extends for higher shells as predicted by our model. The four lobes point along the diagonals of the coordinate system, meaning that the correlations along those directions are enhanced, while correlations along the x- and y-axes are suppressed. This phenomenon can be explained by the contributions G_{ij}^A from single bonds to the affine shear modulus given in (3.4):

$$G_{ij}^A = \frac{\kappa_{ij} r_{ij}^2}{2V} (\hat{n}_{ij}^x \hat{n}_{ij}^y)^2 \sim \sin^2 \phi \cos^2 \phi = \sin^2 2\phi. \quad (3.22)$$

Here we used the polar representation of the unit vector. We already discussed that in our model correlation of a quantity between two sites can only be intro-

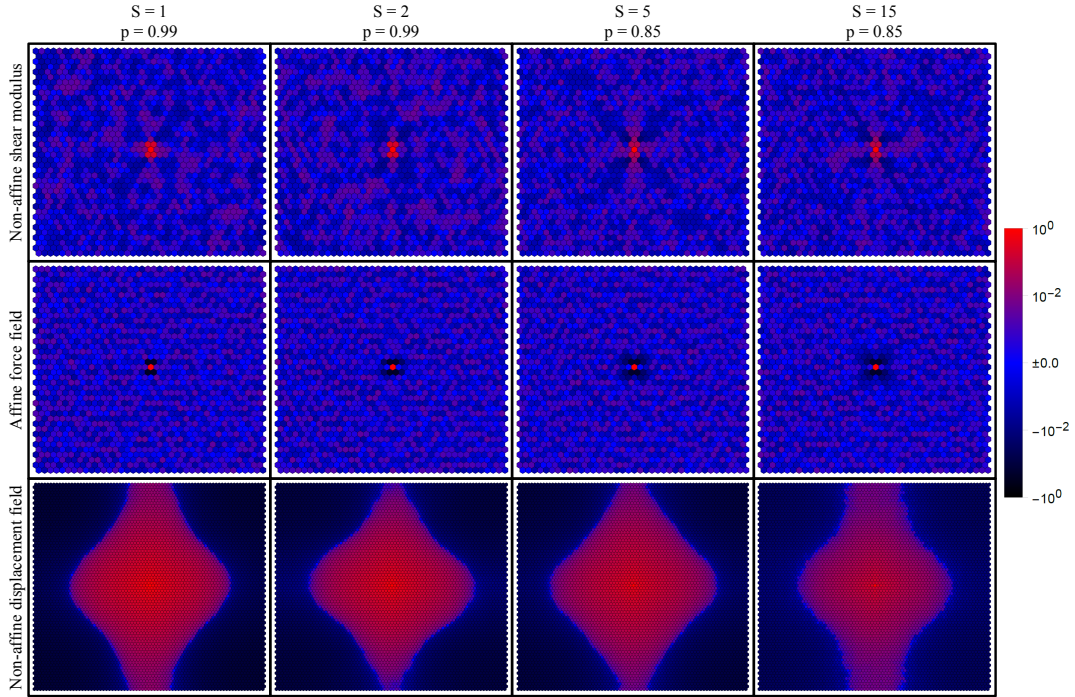


Figure 3.8: Two dimensional correlation maps of G^{NA} shown together with the correlation maps of its constituents Ξ and $\delta\mathbf{r}$. While the anti-correlation lobes of the affine force field extend further with increasing shell number S the correlation of the non-affine displacement field becomes weaker.

duced, if there is a bond between the two sites whose removal would change the value at both sites simultaneously. If we look at the contributions to G^A we notice that for $\phi = k\pi/2$, $k \in \mathcal{N}$, i.e. the x- and y-axes, the bonds do not contribute. In the context of the affine shear modulus they can therefore be treated as not existent at all, as their removal would change nothing about G^A . This also means that there cannot be any correlation in those directions as there are no possible bonds that could introduce it. Furthermore the contribution has a maximum for $\phi = \pi/4 + k\pi/2$, $k \in \mathcal{N}$, which explains why the correlation is strongest in the diagonal direction. As the spatial correlation function contains the product of $\langle G_i^A G_j^A \rangle$ we have to square the contribution from the bond connecting i and j , which leads to:

$$C(r) \sim (G_{ij}^A)^2 = \sin^4 2\phi. \quad (3.23)$$

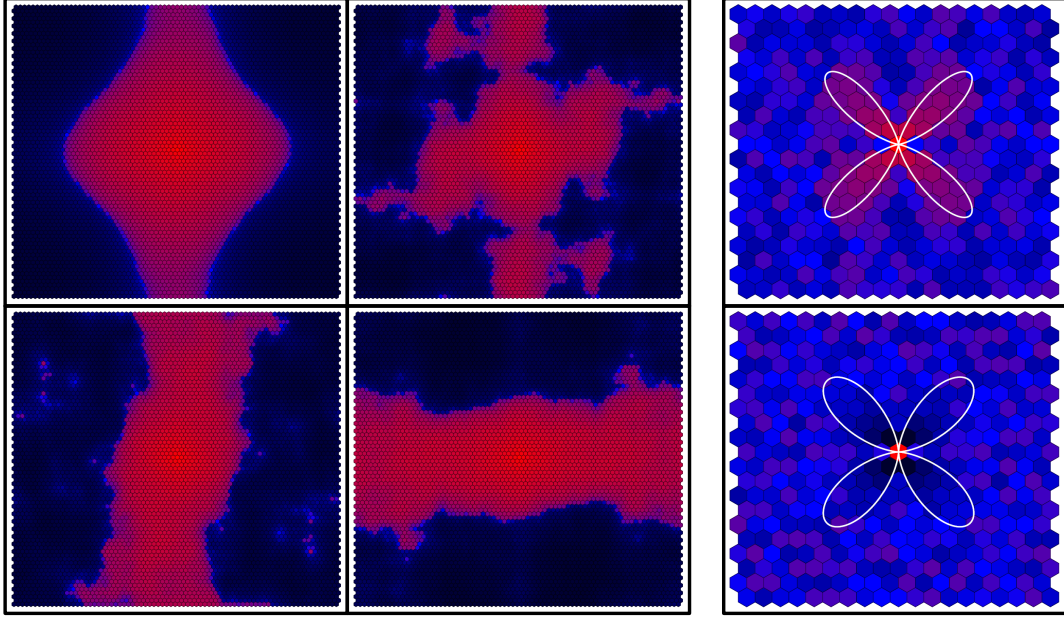


Figure 3.9: Left: non-affine displacement field of individual compared to the average over 100 realisations (top left) for $S = 15, p = 0.85$. Most of them resemble the lower ones where the correlation is either strong in the x- or y-direction. A few show correlation in both directions. Right: Lobe structure of the affine shear modulus (top) and the affine force field (bottom). White lines show the predicted behaviour $\sin^4 2\phi$ for G^A and $\sin^2 2\phi$ for Ξ .

In Fig. 3.9 we can see that the lobes observed for G^A indeed follow that behaviour. As explained before the total shear modulus correlates more strongly with the affine part at high p , which is why the spatial correlation of G mirrors G^A rather than G^{NA} .

For G^{NA} we observe a different pattern with negative correlation lobes pointing in the diagonal direction and positive lobes in the x- and y-direction. This resembles the field described in the Eshelby theory of elastic inclusion. Although it was first derived 1957 by Eshelby [44] to describe heterogenic inclusions in an infinite elastic body, its applicability at atomic level has been shown as well [45, 46]. The correlation patterns of G^{NA} presented in this work agree well with previous findings for simulations at $T > 0$ [47, 48, 49]. To understand this phenomenon better we have to look at the two components which make up G_i^{NA} , the affine force field Ξ_i and the non-affine displacement field δr_i . To capture both alignment

and strength correlation of the fields we calculate the correlation function as:

$$C_{\Xi}(r) = \frac{\langle \vec{\Xi}_i \cdot \vec{\Xi}_j \rangle - \langle \vec{\Xi} \rangle \cdot \langle \vec{\Xi} \rangle}{\langle \vec{\Xi}^2 \rangle - \langle \vec{\Xi} \rangle \cdot \langle \vec{\Xi} \rangle} \Big|_{r_{ij} \in [r, r+\delta r]} . \quad (3.24)$$

For the non-affine displacement field the expression is equivalent and we averaged in the same way as before. The results corresponding to the systems above are shown in Fig. 3.8. We can see that the two features of the correlation of G^{NA} are present separately in the correlation of the affine force field and the displacement field. The affine force field shows qualitatively the opposite behaviour to the affine modulus with anti-correlation in the diagonal direction and no correlation in the x- and y-axes. This can be understood by looking at the individual correlations that one bond \hat{n}_{ij} gives to a site i :

$$\vec{\Xi}_{ij} = -\kappa_{ij} r_{ij} \hat{n}_{ij}^x \hat{n}_{ij}^y \hat{n}_{ij} \sim \sin \phi \cos \phi \begin{pmatrix} \cos \phi \\ \sin \phi \end{pmatrix} = \sin 2\phi \begin{pmatrix} \cos \phi \\ \sin \phi \end{pmatrix} \quad (3.25)$$

The first thing to notice is that contributions to the affine force field show a similar angular dependence as for G^A in that they are 0 for bonds pointing along the x- and y-axes. This also explains why there is no correlation in the affine force field along those directions. The anti-correlation in the diagonal direction stems from the fact the sign of (3.25) changes when the bond is inverted, as we have an odd number of bond terms in the product. The above expression denotes a contribution to the site i where we consider bonds pointing from i to j . The contribution from bond $\hat{n}_{ij} = -\hat{n}_{ji}$ to site j would be $\vec{\Xi}_{ji} = -\kappa_{ji} r_{ji} \hat{n}_{ji}^x \hat{n}_{ji}^y \hat{n}_{ji} = -\vec{\Xi}_{ij}$. So each bond adds exactly opposite values to the affine force fields of the two sites it connects. Therefore Ξ shows a strong anti-correlation behaviour in the direction with the largest contributions (diagonals) and no correlation in the direction with no contributions (x,y-axes). We get the specific angular behaviour similar to G^A (3.23) by considering the square of the individual contribution, although with a negative sign:

$$C(r) \sim \vec{\Xi}_{ij} \cdot \vec{\Xi}_{ji} = -\vec{\Xi}_{ij} \cdot \vec{\Xi}_{ij} = -\sin^2 2\phi . \quad (3.26)$$

As shown in Fig. 3.9 the correlation of Ξ follows this prediction very well. The non-affine displacement field shows a quite different correlation behaviour than G^A or Ξ . We can observe a sharp transition between correlation and anti-correlation along a four-leaved shape. One important feature is the length of correlations, which extends much further than for the shear modulus or the affine force field. We can make sense of this by looking at the definition (3.5) of the local displacement field $\delta\vec{r}_i$, which involves a sum over all eigenmodes of the system. The calculation of these modes involves the full Hessian and therefore depends on the whole system. This connects the displacement fields over long distances even exceeding the maximal interaction length in the system. It also makes sense phenomenologically as the non-affine displacement is a collective reorganisation of the whole system. This requires particle motions to be in some way synchronized with each other, which is well reflected in the correlation maps of $\delta\mathbf{r}$. The observed bias in the y-direction stems from the structure of the triangular lattice. The particle density along the x-axis is larger than along the y-axis, since particles along the latter one are two shells removed from each other, while particles along the x-axis are within their first shells. From the perspective of displacement the system is stretched in the y-direction which let the lobes to appear stretched in this direction as well.

The spatial pattern of its correlation is a superposition of different patterns stemming from the individual realisations as illustrated in Fig. 3.9. We found that there are two major contributions with realisations either having strong correlations in x- or y-direction and a few systems that actually have correlations in both directions. The individual correlation pattern of $\delta\mathbf{r}$ show a similar behaviour as the shear strain correlation leading to shear banding [48]. It is important to note that this is only the correlation pattern of the displacement field and not the displacement field itself.

With those insights the correlation pattern of G^{NA} from Fig. 3.8 appears as a combination of the anti-correlation lobes from the affine force field and the (damped) positive correlation in the x- and y-direction from the displacement field. The pattern of the affine force field shows more distinctly while the pattern of the non-affine displacement field is suppressed.

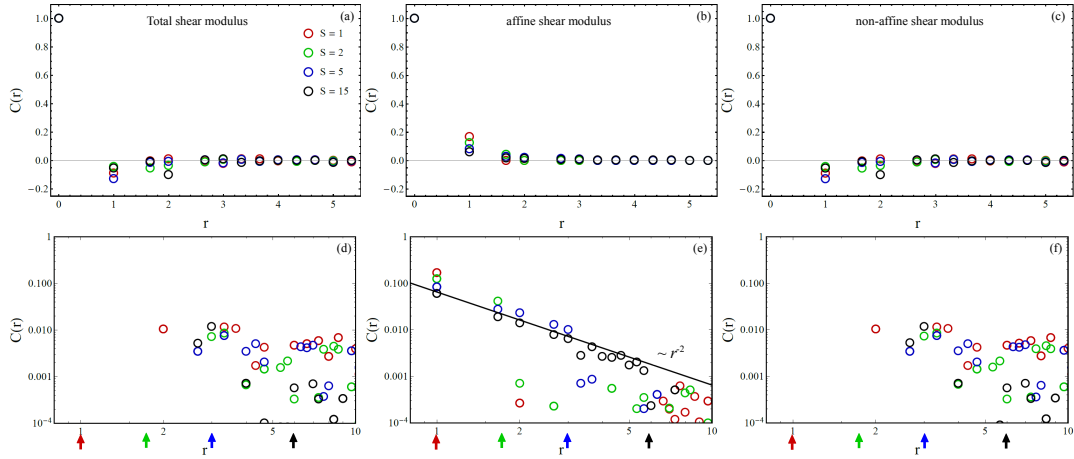


Figure 3.10: Spatial correlation function of $G(a)$, $G^A(b)$ and $G^{NA}(c)$ for critical bond probability p^* with logarithmic plots shown below. Arrows indicate the maximal interaction length R_c of the corresponding system. As we can see G^A follows the predicted $C(r) \sim r^{-2}$ power law for $r < R_c$, while G and G^{NA} show an oscillating behaviour which ranges further for lower shells.

3.3.2 Critical bond probability p^*

Next we look at the correlation of the shear modulus at the critical point. As already discussed one key feature is the diverging fluctuation of the non-affine displacement fields leading to a highly fluctuating local G_i^{NA} which in turn dominates the total local modulus. We therefore expect a different correlation behaviour, where the affine part is suppressed. In Fig. 3.10 we have plotted the radial correlation function $C(r)$ for shells $S = 1, 2, 5, 15$ with corresponding $p^* = 2/3, 1/3, 1/9, 2/63$. The affine part still follows the same power law $C(r) \sim r^{-2}$, as it is independent of p . The correlation function of G however shows an oscillating behaviour that extends longer than the interaction length of the corresponding systems, indicated by arrows. This in agreement with observations by other groups [48, 49, 47, 38]. An important fact is that the correlation at the tail is stronger for shorter interaction lengths. To study this anomaly further we look, as before, at the spatial structure of the correlation. The corresponding maps are shown in Fig. 3.11. We see that G^A shows the same spatial correlation pattern as for high p . G and G^{NA} however show a very different behaviour without a visible lobe structure in any direction and radial oscillation. As the total shear modulus shows the exact same pattern as its non-affine part, we will take a closer look at

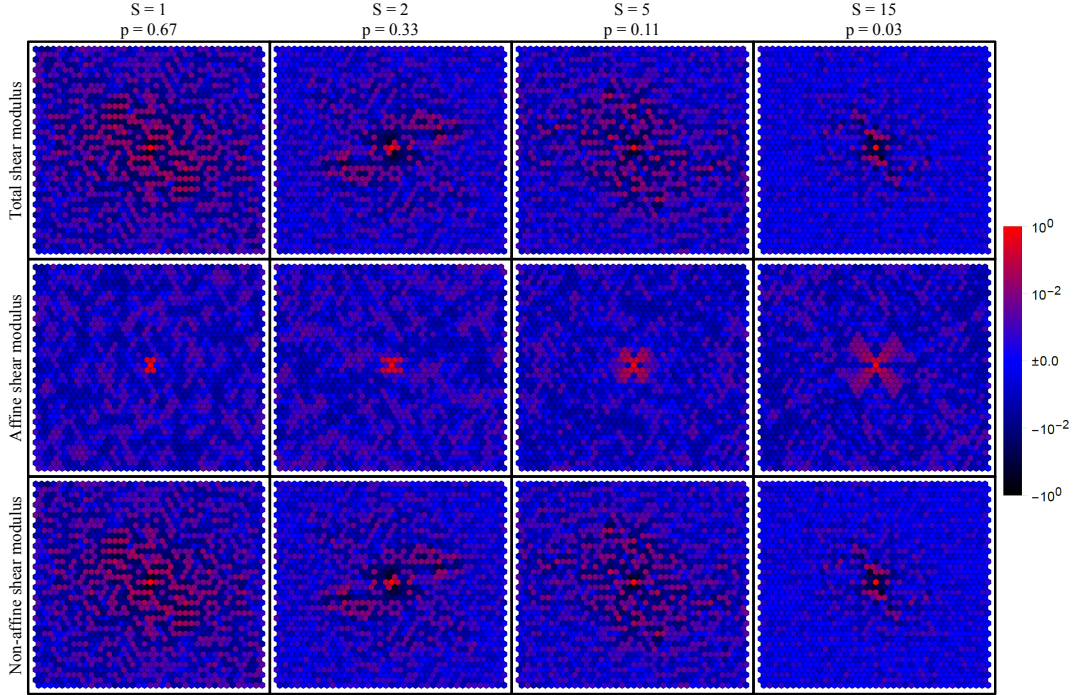


Figure 3.11: Two dimensional maps corresponding to $C(r)$ shown in Fig. 3.10. We can see the extending lobe structure in G^A for higher shells. G^{NA} shows an oscillating long range behaviour with its range decreasing for higher shells. As the local shear modulus is completely anti-correlated with its non-affine part, it shows the exact same correlation pattern.

the latter one and study the spatial correlation of Ξ and $\delta\mathbf{r}$ shown in Fig. 3.12. We can see that the affine force field shows the same correlation as for higher p , with anti-correlation lobes in the diagonals extending for longer interaction length. The displacement field $\delta\mathbf{r}$ however shows a different behaviour. Although for shell $S = 1$ it still has a pattern resembling the four-leaved structure from before, the maps of higher shells look quite different. Most importantly the correlation length and strength reduces with interaction length, which is the source of the observed correlation behaviour in G and G^{NA} . This can be explained by the structure of the corresponding lattice. In Fig. 3.13 we can see the displacement field and lattice of one system with $S = 1$ and $S = 15$. As the critical connectivity stays constant at $Z^* = 4$ the transition from $S = 1$ to $S = 15$ is a mere replacement of strong short ranged bonds by weak long ranged bonds as $\kappa \sim r^{-3}$. This leads to a system of small isolated groups with strong bonds and a more local reorganisation during the deformation process, which reduces correlation between the local non-affine

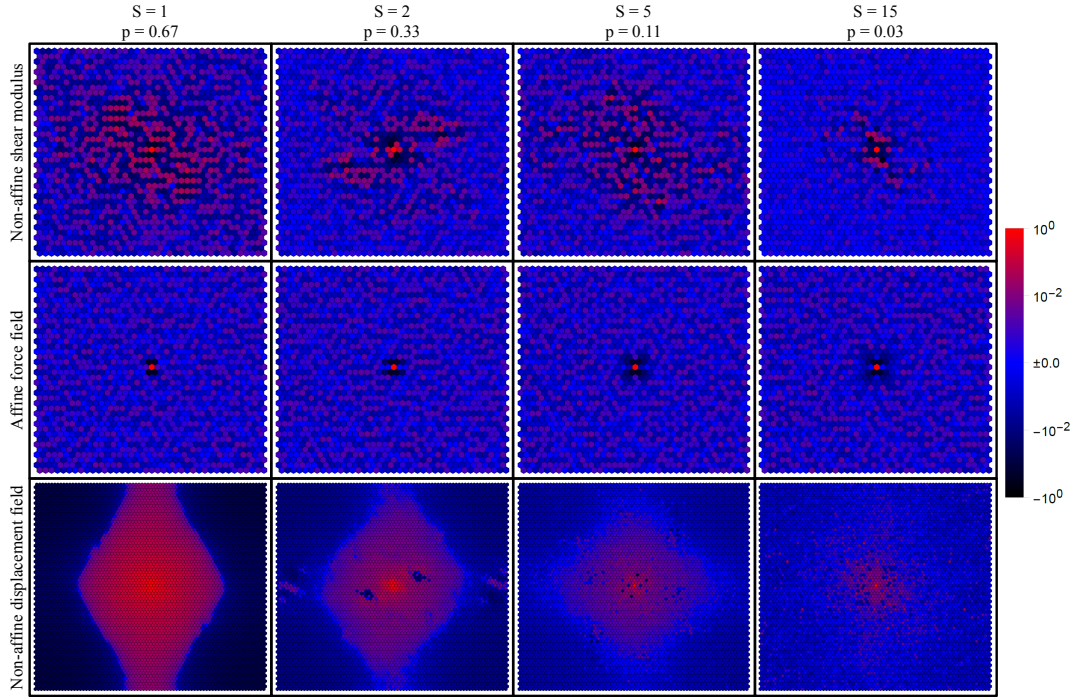


Figure 3.12: Two dimensional correlation maps at p^* of G^{NA} shown together with the correlation maps of its constituents Ξ and $\delta\mathbf{r}$. While the anti-correlation lobes of the affine force field extend further with increasing shell number S the correlation of the non-affine displacement field becomes weaker. The latter effect is stronger as p^* is smaller for higher shells.

displacement fields. This effect is reduced for higher bond probability as the strong bonds form a system-spanning skeleton that supports collective displacements. Again we can conclude that the correlation pattern of G^{NA} is a combination of the anti-correlation from the affine force field and the correlation of the displacement field. As the displacement field at the critical point is much stronger than the affine force field we see the pattern of the displacement correlation much stronger than for higher bond probability p , where the displacement field is much weaker. This distorts the lobe structure of the affine force field correlation and leaves only the anti-correlation pattern. Another consequence of the diverging displacement field at the critical point is the correlation of local G with local G^{NA} . Therefore the correlation pattern of G resembles the one of G^{NA} , with the correlation of G^A being suppressed.

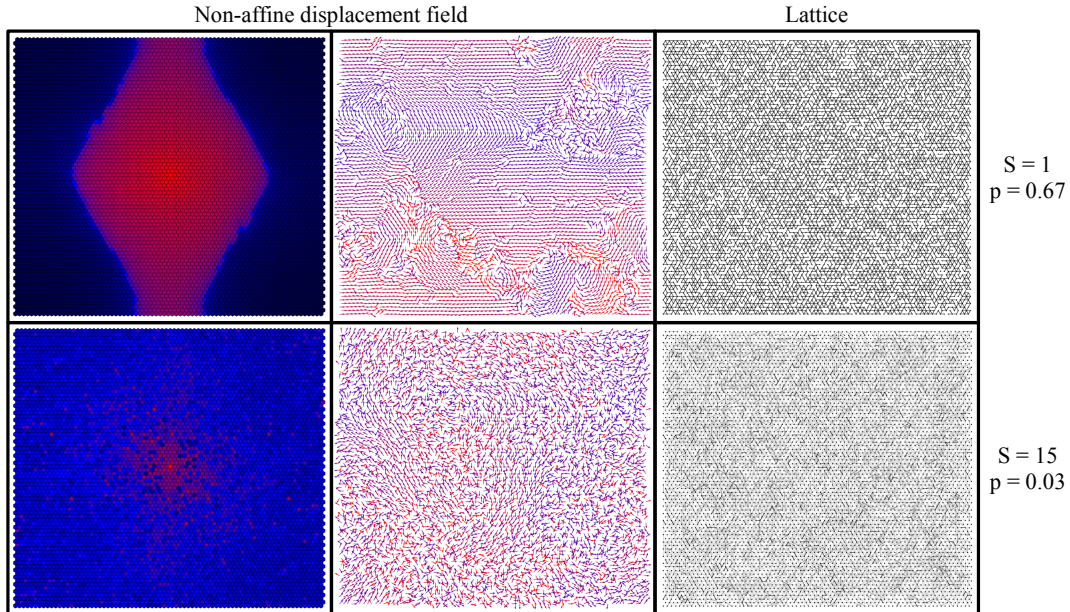


Figure 3.13: Two dimensional correlation map at p^* for $S = 1$ and $S = 15$ with one example of the displacement field and the underlying lattice. The colour of arrows indicates the strength of the field, from weak (blue) to strong (red). In the lattice opacity correlates with the strength of the bonds. We can see that for $S = 15$ the system contains only a few scattered strong bonds and a lot of weak ones. The displacement field mirrors that structure by being localized having only a short correlation length.

3.3.3 Transition from critical to high bond probability

The last regime studied in this work is taken from an intermediate range of bond probability where neither G_i^A nor G_i^{NA} is dominating the correlation behaviour of G . The values for $p(S)$ are $p(1) = 0.85, p(2) = 0.7, p(5) = 0.4, p(15) = 0.3$. The correlation functions are shown in Fig. 3.14. Again the affine shear modulus follows the power law decay shown earlier, while the correlation of G^{NA} shows oscillatory behaviour as for p^* . The range is however shorter than at the critical point and decreases further with higher shells. The total shear modulus shows a peculiar behaviour in that it shows anti-correlation for short range and correlation similar to G^A for long range. Only for $S = 1$ the correlation of G mirrors mostly G^{NA} due to the strong correlation of G with G^{NA} (see Fig. 3.15).

To see how the correlation in this transition regime of p behaves spatially, we look again at the correlation maps of G , G^A and G^{NA} . G^A shows the same lobe structure as at the critical point and high p . G^{NA} shows a lobe structure

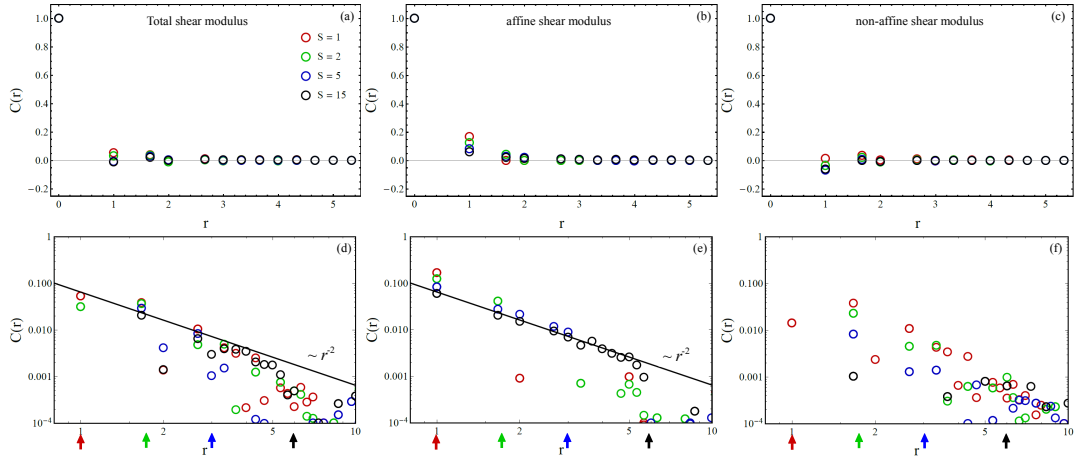


Figure 3.14: Spatial correlation function of $G(a)$, $G^A(b)$ and $G^{NA}(c)$ for intermediate bond probability p with logarithmic plots shown below. Arrows indicate the maximal interaction length R_c of the corresponding system. As we can see G^A follows the predicted $C(r) \sim r^{-2}$ power law for $r < R_c$. G follows this law only approximately while G^{NA} shows an oscillatory behaviour similar to p^* but with shorter range.

similar to high p , with anti-correlation in the diagonals and positive correlation in the x- and y-axes. Compared to high p the anti-correlation lobes appear more clearly and extend into the first shell. To get insight into this pattern we look at the correlation maps of Ξ and $\delta\mathbf{r}$, which are shown in Fig. 3.16. Similar to G^A the affine force field correlations are unaffected by p and therefore show the same behaviour as before. The non-affine displacement field correlation shows a behaviour more similar to high p with lobes in the x- and y-direction and a clear boundary between correlation and anti-correlation. The lobes arise again as a superposition of strong correlation in x- or y-direction in single realisations. G^{NA} appears as a combination of those two patterns.

The local shear modulus neither strongly correlates with G^A nor anti-correlates with G^{NA} and therefore shows parts of both correlations patterns. We can see correlation in the x- and y-directions stemming from G^{NA} . The anti-correlation in the diagonals is suppressed by the correlation from G^A with only a very short range anti-correlation remaining. This also explains the long correlation length of G that we see in Fig. 3.15, as positive correlations from G^{NA} and G^A add up. For higher or lower bond probability either the affine or non-affine part becomes dominant leading to the correlation behaviour discussed before.

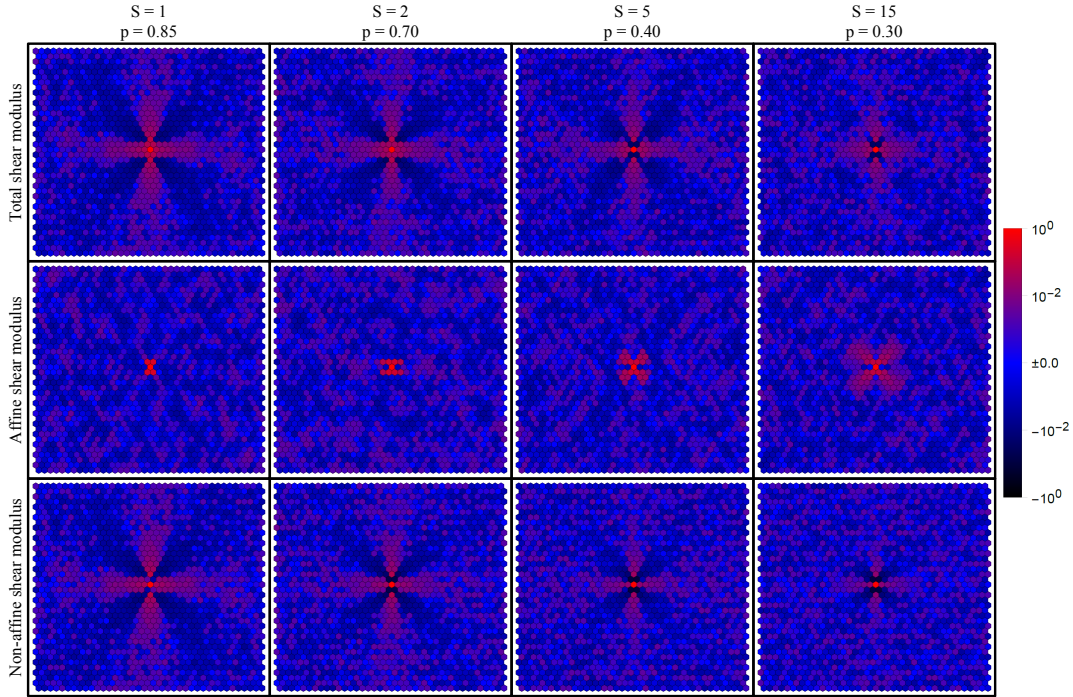


Figure 3.15: Two dimensional maps corresponding to $C(r)$ shown in Fig. 3.14. We can see the extending lobe structure in G^A for higher shells. G^{NA} shows strong anti-correlation in the diagonals and correlation along x- and y-axis with its range decreasing for higher shells. The correlation pattern of G appears as an overlap of G^A and G^{NA} with the latter contributing more as $\rho_{NA} > \rho_A$. Since $\rho_{NA}, \rho_A < 1$ we still see some contribution from G^A .

3.4 Summary

In this work the influence of interaction range on the spatial correlation of shear modulus G in dependence of the bond probability p was studied on the example of a random depleted triangular lattice. The correlation maps of all relevant quantities ($G, G^A, G^{NA}, \Xi, \delta\mathbf{r}$) are plotted in Fig. 3.17-3.21. We found that the implementation of longer bonds introduces correlation in the affine part of the shear modulus G^A and the affine force field Ξ at the length of the maximal bond length. Both show a lobe structure with positive correlation (G^A) and anti-correlation (Ξ) in the diagonal direction that is independent of p . This stems from the individual contribution of bonds to both quantities, which is maximal in the direction of the diagonal and zero in x- and y-direction. In the case of a power law decay of the spring constant, the correlation of G^A decays according (3.21). The p dependence

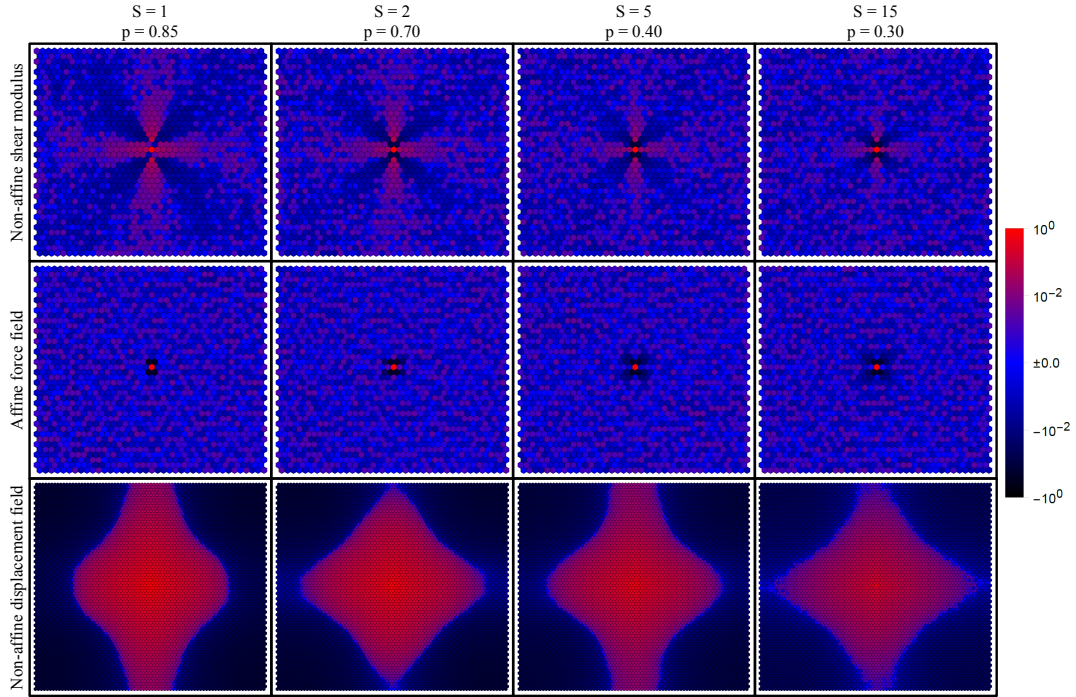


Figure 3.16: Two dimensional correlation maps at intermediate p of G^{NA} shown together with the correlation maps of its constituents Ξ and $\delta\mathbf{r}$. While the anti-correlation lobes of the affine force field extend further with increasing shell number S the correlation of the non-affine displacement field becomes weaker, leading to the decreasing correlation length of G^{NA} .

of the correlation is introduced by the non-affine displacement field $\delta\mathbf{r}$, which in turn is mostly determined by the dominant $S = 1$ bonds. Therefore similar bond probabilities give similar correlation patterns for $\delta\mathbf{r}$. As the critical bond probability drastically decreases with the number of included shells the correlation length of $\delta\mathbf{r}$ is reduced for longer interaction at p^* .

The correlation pattern of the local shear modulus depends on two important interplays. First there is the affine force field and the non-affine displacement field, which make up the non-affine shear modulus. As p increases the ratio $\langle\delta\mathbf{r}\rangle/\langle\Xi\rangle$ decreases and the anti-correlation lobes of Ξ show up in the pattern of G^{NA} . In addition to that the positive correlation in x- and y-direction from $\delta\mathbf{r}$ are suppressed and the range of this correlation in G^{NA} decreases.

The other important interplay takes place between G^A and G^{NA} . When lowering p the affine part decreases while the non-affine part increases. Furthermore the spatial fluctuation of G^{NA} increases which leads to the shear modulus being

locally dominated by its non-affine part (although in total G^{NA} might be small). Therefore the correlation pattern of G changes from resembling the affine part to resembling the non-affine part. In the latter regime the correlation length is mostly determined by the non-affine displacement field, which decreases with longer interaction length. So with longer interaction we have an increase of correlation length for high p close to the full lattice due to the decrease of correlation between G and G^{NA} . For lower p closer to the critical point we have a decrease of correlation length due to the decreasing correlation in the displacement field.

To summarize there are two main results in this chapter. One is the analytical link between the spatial correlation of the affine shear modulus and the spring constant:

$$C(r, \phi) \sim r^4 \kappa^2 \sin^4 2\phi. \quad (3.27)$$

The other is the demonstration of the non-monotonic correlation of G both with regard to the interaction range and the bond probability as well as its aforementioned back tracing to the interplay of the local affine shear modulus with the affine force field and the non-affine displacement fields, which in turn depend on the structure of the lattice both in terms of interaction range and decay. Another important point is the demonstration that power law correlations observed in simulations can indeed be found in simple depleted lattice models, if appropriately tuned. This opens the possibility to study anomalous properties of disordered solids that are based on phonon scattering such as sound attenuation on lattice models. The next step would be to analyse the phonon scattering based on the correlation function (3.27) and determine quantities like sound attenuation from it.

It is also important to note that the latter results from the choice of power law decay for the spring constant, as it introduces very weak bonds for long range interaction which hinder correlation length. For a different choice of spring constant behaviour the results for low p might be different.

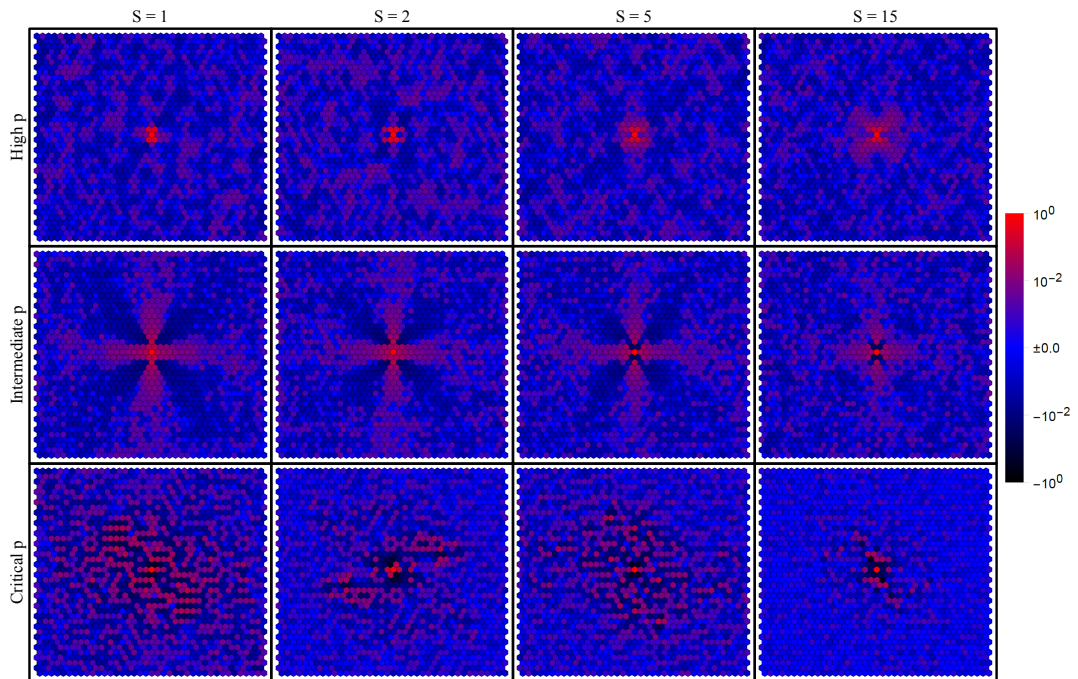


Figure 3.17: Two dimensional correlation maps of G .

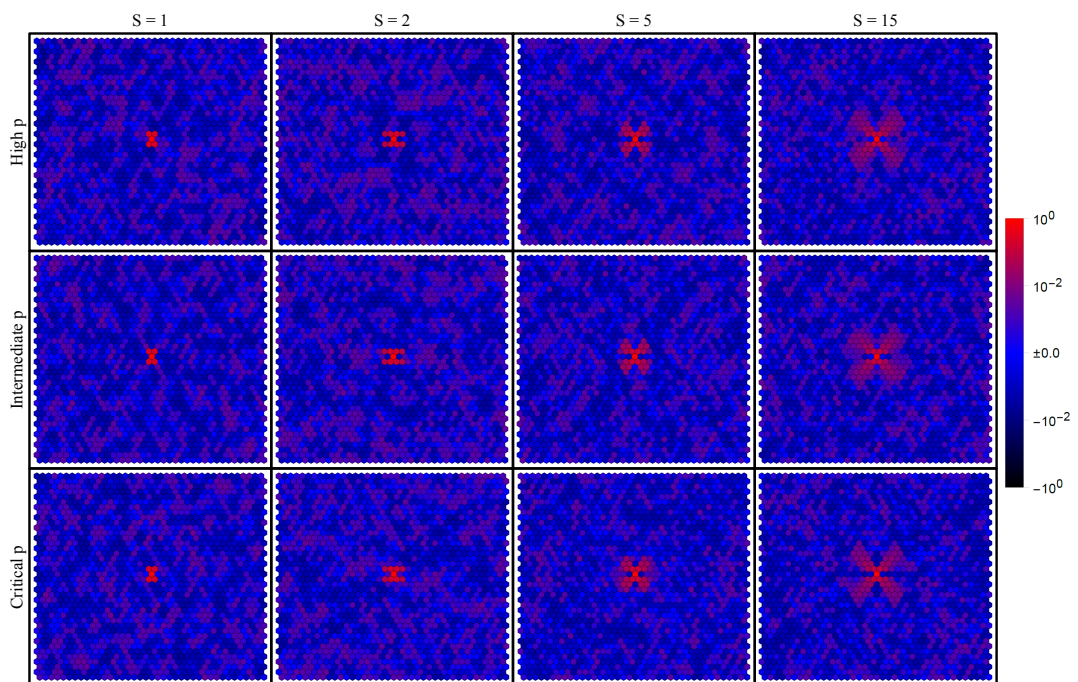


Figure 3.18: Two dimensional correlation maps of G^A .

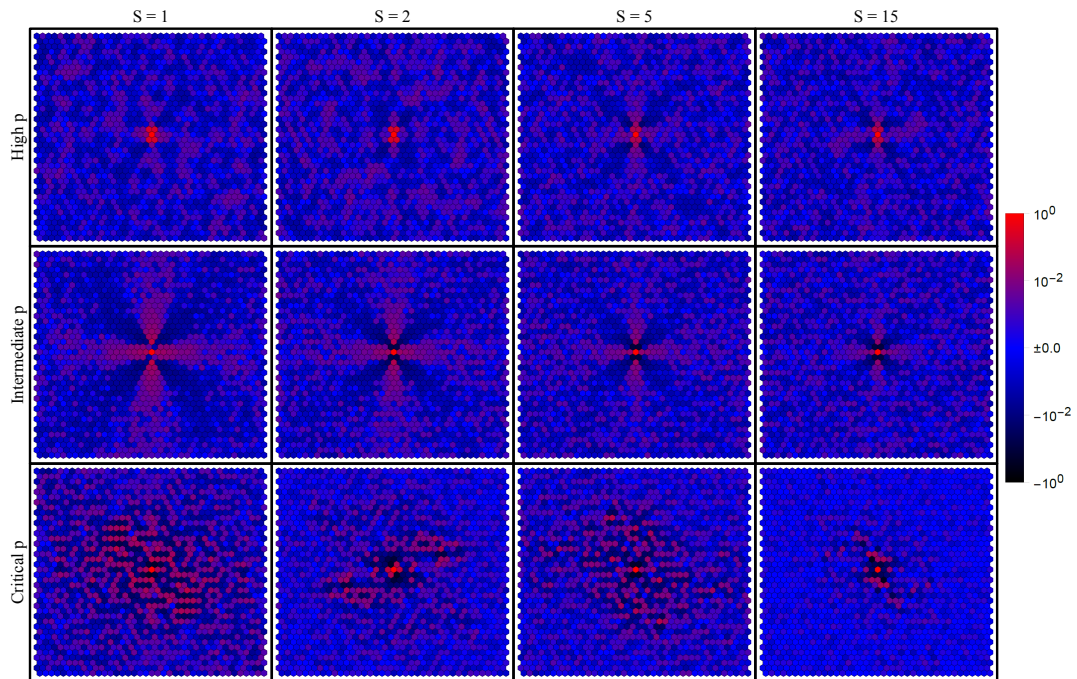


Figure 3.19: Two dimensional correlation maps of G^{NA} .

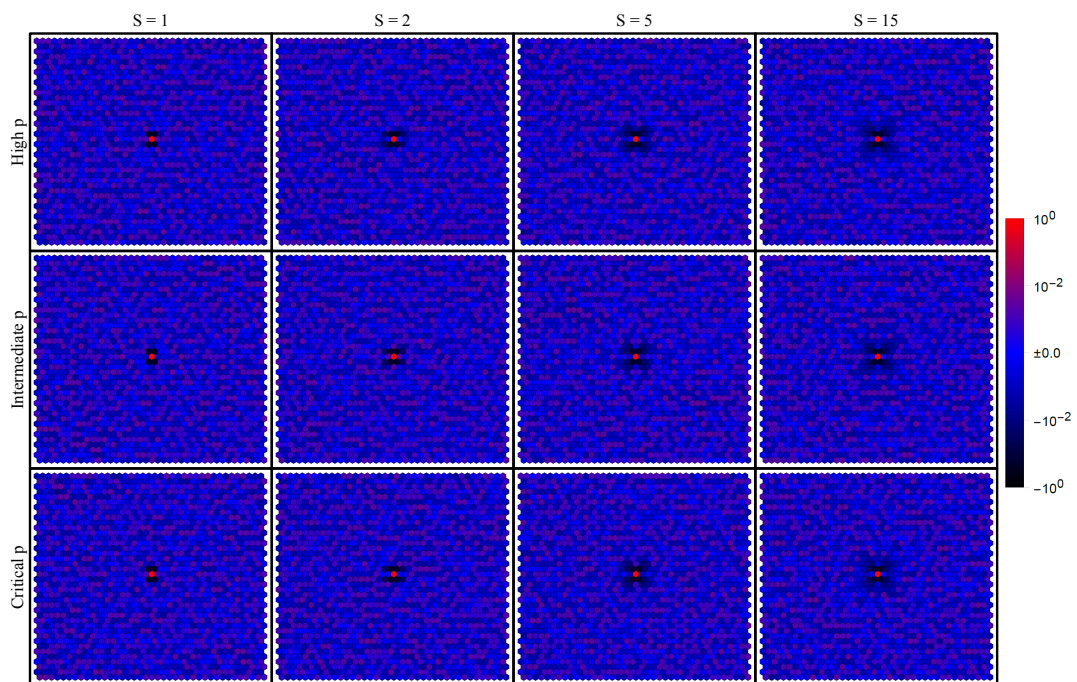


Figure 3.20: Two dimensional correlation maps of Ξ .

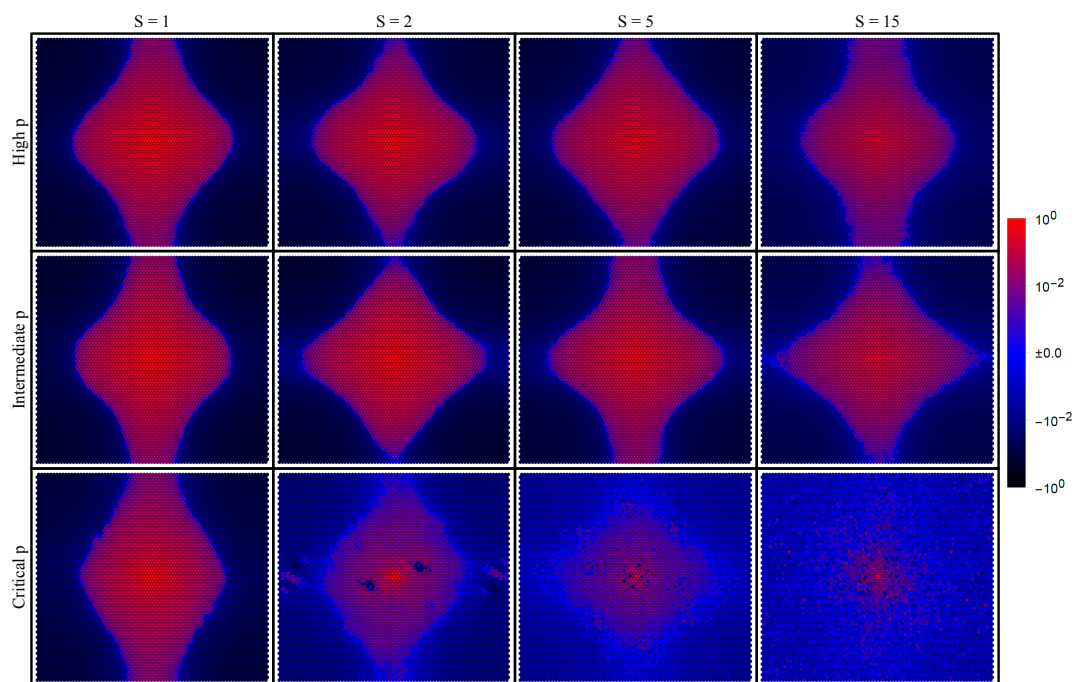


Figure 3.21: Two dimensional correlation maps of δr .

Polymer networks

Polymers play a big role in modern life, from the widely used polystyrene over membranes for fuel cells to biomolecules as proteins or DNA. Much analytical work has been done in analysing the vibrational properties of polymers [50, 51], starting from theoretical determination of the single-chain backbone vibrational spectra in seminal work by J. G. Kirkwood [52] and K. S. Pitzer [53], followed by the powerful combination of Wilson’s GF-method with group theory by P. Higgs [54]. Still the spectra of more realistic polymer melts are only little explored, due to lack of any periodicity or symmetry in the system, which makes the mentioned analytical methods inapplicable.

In this work we will explore the behaviour a simple spring-bead polymer model, known as Kremer-Grest [55] model, at low temperature and present a systematic review on how the vibrational spectrum depends on the length and bending stiffness of the individual chains. The motivation for this, brought forward by BASF and Professor Alexei Lapkin from the Department of Chemical Engineering and Biotechnology at the University of Cambridge, is the development of a sensor, based on Raman spectroscopy, to monitor the growth of polymers in real time. Since the Raman spectrum is tied to the VDOS $D(\omega)$ in the following way [56]:

$$I_{Raman}(\omega) = \frac{\omega [n(\omega, T) + 1] C(\omega)}{\omega^2} D(\omega), \quad (4.1)$$

it is important to present a systematic review of the VDOS for changing length and bending stiffness. Here $n(\omega, T)$ denotes the Bose distribution function and $C(\omega)$ the coupling between photons and phonons.

The first part of the chapter in which we examine the vibrational properties of our model system is mostly based on [57]. We’ll give a description of the model, which was simulated in LAMMPS [58] by Christopher Ness at 25% of the approximate

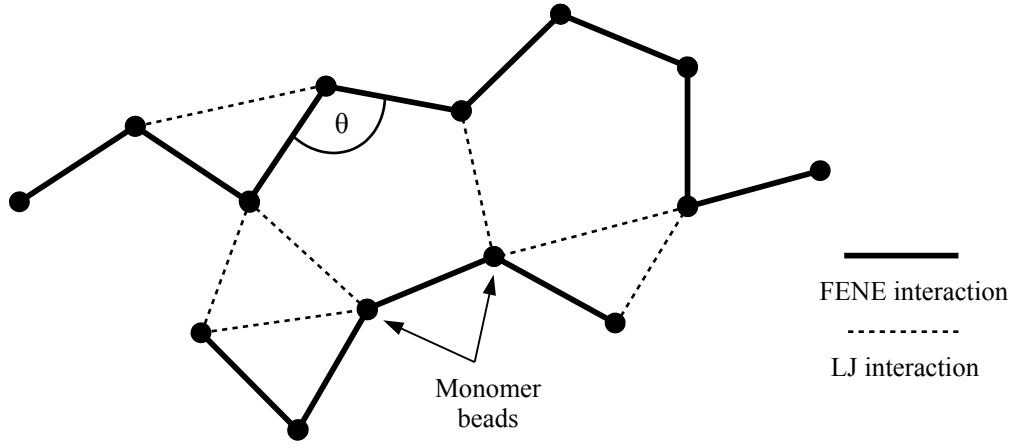


Figure 4.1: Sketch of our model polymer system.

glass transition temperature T_g . This was followed by a second relaxation using the gradient method done in python to reach a configuration at $\approx 0.025\%$ of T_g , which is sufficiently low to use harmonic approximation without further assumptions. Afterwards we present the results for changes in structure and vibrational patterns, including a comparison with analytic results for similar single chain systems. The last part will revolve around the mechanical stability of our systems. Since the calculations were performed at low but non-zero temperatures we will discuss the limits of non-affine lattice dynamics in this context and provide a solution for its shortcomings.

4.1 Model systems

The model uses a coarse-graining on the level of the monomer, such that individual polymer chains are treated as a chain of monomer beads connected with elastic springs as depicted in Fig. 4.1. For each monomer bead in the system LAMMPS was used to solve the Langevin equation

$$m \frac{dv}{dt} = -\frac{m}{\xi} v + \frac{dU}{dr} + f_B(t), \quad (4.2)$$

for uniform monomers of mass m and velocity v , coefficient of friction $1/\xi$ and random forces $f_B(t)$ satisfying $\langle f_B(t) f_B(t') \rangle = 2mk_B T \delta(t - t')/\xi$. The simulation was performed at $T = 0.1$ and three potentials were used: A finitely extensible

nonlinear elastic (FENE) interaction along the backbone of the polymer chain, a truncated Lennard-Jones potential acting on all particle pairs within a cut-off of 2.5 and an angular potential between neighbouring bonds along the backbone, determining the bending stiffness of our model chains. The potentials have the explicit form:

$$\begin{aligned}
 U_{FENE}(r) &= -\frac{1}{2}\varepsilon_{FENE}R_0^2 \log \left[1 - \left(\frac{r}{R_0} \right)^2 \right] \\
 U_{LJ}(r) &= 4\varepsilon_{LJ} \left[\left(\frac{\sigma}{r} \right)^{12} - \left(\frac{\sigma}{r} \right)^6 \right] + 4\varepsilon_{LJ} \left[\left(\frac{\sigma}{2.5} \right)^{12} - \left(\frac{\sigma}{2.5} \right)^6 \right]; r < 2.5 \quad (4.3) \\
 U_{bend}(\theta) &= \varepsilon_{bend}[1 - \cos(\theta - \theta_0)]
 \end{aligned}$$

The first two potentials combined are the standard choice for the Kremer-Grest model.

With reference to fundamental units of mass ν , length d , and energy ϵ , the parameters are set as $\sigma = 1$, $R_0 = 1.5$, $m = 1$ and $\varepsilon_{LJ} = 1$, giving a time unit of $\tau = \sqrt{m\sigma^2/\varepsilon_{LJ}}$, and we set $\xi = 100\tau$. The system volume V has units d^3 . The equilibrium distance between two beads in a chain $\sigma \approx 0.96$ is substantially different from the equilibrium distance of the pure LJ-interaction $r_0 \approx 1.12$ to avoid crystallization of the system. As rest angle we chose the bond angle $\theta_0 = 109.5^\circ$ of the polystyrene backbone. A dissipative timescale emerges as $m\sigma^2/\xi\varepsilon_{LJ}$, and a thermal timescale emerges as $m\sigma^2/\xi k_B T$. The state of our system, i.e. whether it is in the melted or glassy state, is simply given by the ratio of these timescales, as $T^* = k_B T/\varepsilon_{LJ}$. Initial loose polymer configurations are generated within a cubic periodic domain using a non-overlapping random-walk algorithm. We use a system of 5×10^3 monomers, in chains of uniform length L , which we vary from 2 to 50. For each value of L we generate 5 realisations of the system for the purposes of ensemble averaging. The system is first equilibrated in a melted state at $T^* = 1.2$, maintaining zero external pressure using a Nose-Hoover barostat. The system is subsequently cooled to $T^* = 0.1$ by decreasing T^* at rate $1/\tau_c$, with $\tau_c \sim \mathcal{O}(10^5)\tau$. Taking those configurations obtained from LAMMPS, relaxation with a simple gradient method was performed to bring the system closer to zero temperature and reduce the net forces \mathbf{f} acting in the system. To estimate the temperature after

the second relaxation we used the ratios of the force fields before and after the relaxation together with $T \sim \langle \mathbf{f}^2 \rangle$:

$$T_{new} = T_{old} \frac{\langle \mathbf{f}_{new}^2 \rangle}{\langle \mathbf{f}_{old}^2 \rangle} \quad (4.4)$$

We set up the gradient method so that it stops when $\langle \mathbf{f}_{new}^2 \rangle / \langle \mathbf{f}_{old}^2 \rangle < 10^{-3}$, leading to a target temperature of $T = 10^{-4}$, which is very small compared to the glass transition temperature $T_g = 0.4$.

Those calculations were performed for systems with five different chain lengths $L = 3, 4, 5, 10, 50$ and various bending stiffness ranging from $\varepsilon_{bend} = 0$ to $\varepsilon_{bend} = 1000$. Since the calculations are based on harmonic approximation and to get a better comparability of the different interactions, we will from now on look at the effective spring constants obtained from the second derivative at the rest position of each potential. We get:

$$\kappa_{LJ} \approx 57.1$$

$$\kappa_{FENE} \approx 981.3 \quad (4.5)$$

$$\kappa_{bend} = \varepsilon_{bend},$$

which is useful as it shows the clear difference between the strength of bonds along the chain and bonds formed between chains $\kappa_{FENE} / \kappa_{LJ} \approx 17.2$. It is important to note that κ_{FENE} was obtained from the combination of U_{FENE} and U_{LJ} as both potentials contribute to interactions along the backbone.

4.2 Structural analysis

We will now have a look at how the structure of the system changes with length and bending stiffness by looking at the radial distribution function $g(r)$, the distribution of angles along the chains and the density of the system. The latter is interesting as the initial relaxation in LAMMPS was performed under constant pressure and changing volume. Results for the density are shown in Fig. 4.2. We

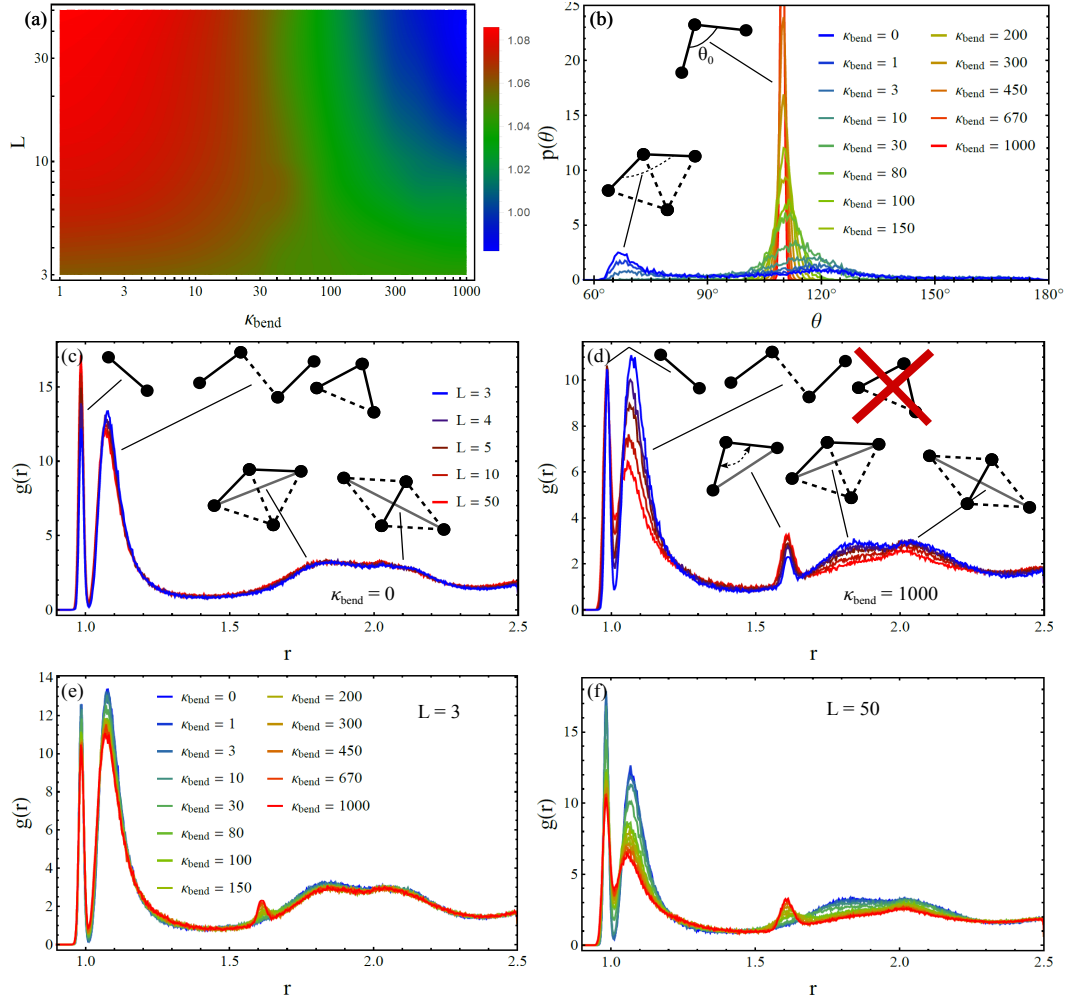


Figure 4.2: (a) Density $\rho = N/V$ of our systems. (b) Angle distribution of our systems with two configurations responsible for its peaks. (c-f) Radial distribution function $g(r)$ for flexible and stiff chains with variable lengths shown with main configurations.

can see that overall the density decreases with increasing bending stiffness. This happens because stiffer chains have a longer persistence length and cannot coil around each other so easily, leading to the formation of small cavities in between the chains. This increases the volume and in turn decreases the density of the system. The effect is accompanied by a drastic change in the angle distribution. Flexible chains can adjust the bond angle to their surrounding filling less space, which results in angles piling up around $\theta = 60^\circ$, corresponding to close packing structures, while stiff chains have a mostly fixed bond angle $\theta_0 = 109.5$. This is reflected well by the angle distribution of our systems shown in Fig. 4.2. Another important difference between flexible and stiff chains is the dependence on chain

length. Since bonds in the backbone are shorter than inter chain LJ bonds, an increase in chain length leads to an overall decrease in volume and an increase in density for flexible chains. Stiff chains show the exact opposite behaviour as they cannot coil around each other very well. The change of behaviour happens at around $\kappa_{bend} \approx 80$, where also the peak at $\theta_0 = 109.5$ starts to emerge, supporting the given argument.

The radial distribution function also shows a rich phenomenology depending both on length and bending stiffness as can be seen in Fig. 4.2. In general we can observe two peaks at the FENE rest length $r = 0.96$ and the LJ rest length $r = 1.12$. Since the FENE bonds are much stronger than LJ bonds the peak is narrower. Aside from that the behaviour mirrors the changes in structure discussed before. Let's start by analysing the flexible chain, whose $g(r)$ does not depend much on the chain length aside from the replacement of LJ by FENE bonds, leading to an increase in the FENE peak and a decrease in the LJ peak. At larger distances we see a double peak caused by two distinct configurations originating from a chain pushing itself in between two bonds of another chain (as shown in Fig. 4.2). The configuration has two characteristic distances $r = 1.73$ and $r = 2.02$. The actual peaks are observed at slightly shifted positions due to overlapping of the two peaks and general imperfection of the LJ rest length.

By increasing the bending stiffness LJ bonds between next-to-nearest neighbours along the chain break as more and more angles snap into the rest position. This creates a peak at $r = 1.57$ and the breaking of our inserted configuration described before, lowering $g(r)$ at this distance as well as the LJ peak. This effect is more severe in systems with longer chains, as the density is decreased on top of that, leading to longer average distances in the polymer network. This shows especially when we look at very stiff chains. The long persistence length of stiff chains leads to a drastic decrease of nearest-neighbour LJ bonds as the chains cannot really coil around each other. In addition you add more bending interaction as the chain length increase leading to more rest angle configurations and an increase of the corresponding peak.

4.3 Vibrational density of states

The prime interest of this section is the vibrational density of states (VDOS) and its dependence on chain length and bending stiffness. In the following section we

will see how the structural changes, explained above, translate into a reorganisation of vibrational modes and change in motion pattern. The VDOS is obtained in the same way as before using eq. (1.12) to calculate the Hessian \mathbf{H} of our system and solving the eigenvalues problem (1.6) to obtain eigenvectors and -values. One new thing is the bending interaction from (4.3). Although it is a three-body interaction we can perform the second derivative with respect to all combinations of two spatial components by using:

$$\cos \theta_{ijk} = \frac{\vec{r}_{ij} \cdot \vec{r}_{ik}}{|\vec{r}_{ij}| |\vec{r}_{ik}|} \quad (4.6)$$

The explicit components for \mathbf{H} are written in the Appendix A.1. Another difference to previous work of chapter 2,3 is the fact that our systems are not at a minimum of the energy landscape, which leads to net forces acting in the system. Since the forces are small we can ignore them in the context of VDOS, but this might cause some issues for the calculation of the shear modulus later.

4.3.1 Projection on different motion patterns

In contrast to mono-atomic networks, polymer systems have a much more defined spatial structure to them. If we take one triplet of particles with bending interaction we can define orthogonal directions relative to that triplet, as shown in Fig. 4.3. A similar approach with different projections was used by Tanguy et al. [59] to analyse the VDOS of amorphous silica. The first is the out-of-plane motion perpendicular to the triplet plane, called *rocking motion*. The other two are in-plane motions, one being directed along the bisector of the bond angle, called *perpendicular motion* and the other pointing perpendicular to the bisector, called *along chain motion*. Here 'along' and 'perpendicular' refer to the direction of the chain backbone. To obtain each of these contributions separately we project the displacement vector $\hat{v}_i(\omega_k)$ of each particle onto the orthogonal basis formed by the three unit vectors $(\hat{a}_{i,1}, \hat{a}_{i,2}, \hat{a}_{i,3})$ (see Figure 4.3), generating a new representation $\hat{u}_i(\omega_k)$:

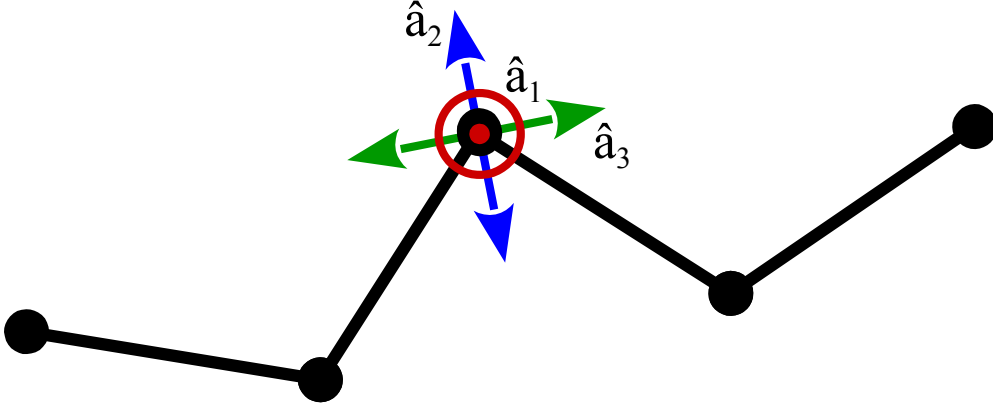


Figure 4.3: Special motion directions relative to our chain. \hat{a}_1 denotes rocking motion going into the plane. \hat{a}_2 and \hat{a}_3 are perpendicular and along chain motion.

$$\hat{u}_i(\omega_k) = \begin{pmatrix} \hat{v}_i(\omega_k) \cdot \hat{a}_{i,1} \\ \hat{v}_i(\omega_k) \cdot \hat{a}_{i,2} \\ \hat{v}_i(\omega_k) \cdot \hat{a}_{i,3} \end{pmatrix} = \begin{pmatrix} \hat{u}_{i,1} \\ \hat{u}_{i,2} \\ \hat{u}_{i,3} \end{pmatrix} \quad (4.7)$$

$$\mathcal{X}_j(\omega_k) = \sum_{i=1}^N \hat{u}_{i,j}^2 \quad j = \{1, 2, 3\}$$

$\mathcal{X}_j(\omega_k)$ is the contribution by the three different motions discussed before. By averaging over these values in a bin of the frequency histogram we get a partial VDOS showing the contribution of each of these three motions to the full VDOS. This gives us insights into the dynamics of the chains at different frequencies in the spectrum.

4.3.2 Imaginary frequencies, collective Lennard-Jones sea and higher frequency modes

One feature of our systems, that is very different from depleted lattices, is the fact that it is not at an energy minimum. We discussed earlier how the system was brought to a low relative temperature of $T = 10^{-4}$ by the gradient method. Even in this state very close to zero temperature there are still net forces in the system, which means it is not at an energy minimum. This results in the Hessian of the system to be no longer positive semi-definite and hence having negative

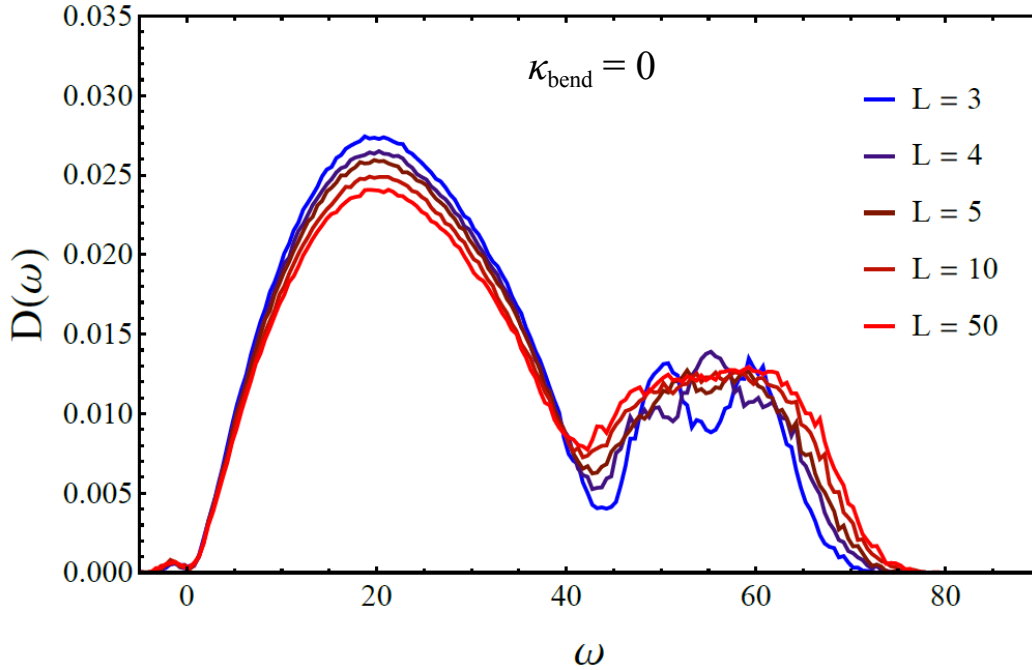


Figure 4.4: VDOS of flexible chains. The separation between low frequency LJ-peak and the high frequency FENE contributions can clearly be seen. Another important feature is the loss of peak structure for longer chains.

eigenvalues $\lambda < 0$ [60, 61, 62, 63, 64]. Through the relation $\omega^2 = \lambda$ this gives us imaginary eigenfrequencies, which will be shown in the plots as negative real values for convenience. A physical interpretation can be obtained from the harmonic oscillator model, where imaginary frequencies correspond to non-oscillatory motions, i.e. permanent rearrangement, which is in agreement with findings that link those modes to diffusive properties of the system [65]. This makes sense as the system would naturally try to release the net forces stored in the system to get to a nearby energy-minimum. As non-affine lattice dynamics is only defined at zero temperature without net forces in the system, this leads to problems when calculating the non-affine part of the shear modulus. Since we are at a very low temperature, there are not many of those modes in our systems, which is why they are of no interest in the context of the vibrational spectrum. We will address those problems in a later section when we analyse the mechanical stability.

For flexible chains with $\kappa_{bend} = 0$ the VDOS are given in Fig. 4.4 for various chain lengths. It shows the common feature of all systems with low bending stiffness studied in this work which is a distinct splitting of the VDOS into a low and

high frequency part. The low frequency part occupies $\omega = 0 \rightarrow \sim 40$, while the high frequency part extends up to $\omega \approx 65$ in most cases, and $\omega \rightarrow 100$ when $\kappa_{bend} \sim \kappa_{FENE}$. The low and high frequency bands are separated by a trough, whose depth and precise location in ω is subtly dependent on κ_{bend} . The general splitting of the VDOS into two bands was shown previously by Jain and De Pablo [66], who considered fully flexible chains only. By considering the relative prefactors of the LJ and FENE potentials, we find it instructive to interpret the low frequency part as a Lennard-Jones ‘sea’, that comprises weak but ubiquitous inter-chain interactions, while the high frequency part represents FENE bonds, that are fewer in number and follow specific paths along chain backbones. Within this picture, the contributions to the VDOS coming from bending interactions are highly sensitive to κ_{bend} . In particular, when κ_{bend} is small, we expect bending interactions to contribute frequencies comparable to, or even lower than, the LJ interactions. By contrast, when $\kappa_{bend} \rightarrow \kappa_{FENE}$ we expect the bending interactions to contribute frequencies comparable to the FENE interactions. We anticipate a redistribution, therefore, of the bending contributions from the low to the high frequency band as κ_{bend} is increased.

4.3.3 VDOS for chains with $L = 3$

It is instructive to take a closer look at the system with $L = 3$, for which we have an analytically solvable model system as presented in Appendix A.4. Excluding the LJ interaction in between chains and the trivial zero-modes, each chain adds the three eigenfrequencies from (A.19) to the VDOS:

$$\begin{aligned}\omega_1^2 &= \frac{\kappa}{m}(2 - \cos \theta) \\ \omega_2^2 &= \frac{\kappa}{2m} \left(2(1 + 2\gamma') + (1 - 2\gamma') \cos \theta + \sqrt{(2(1 + 2\gamma') + (1 - 2\gamma') \cos \theta)^2 - 24\gamma'} \right) \\ \omega_3^2 &= \frac{\kappa}{2m} \left(2(1 + 2\gamma') + (1 - 2\gamma') \cos \theta - \sqrt{(2(1 + 2\gamma') + (1 - 2\gamma') \cos \theta)^2 - 24\gamma'} \right)\end{aligned}\tag{4.8}$$

Here m denotes the mass, κ the effective spring constant of the FENE bonds κ_{FENE} , θ the bond angle and $\gamma' = \kappa_{bend}/(\kappa r^2)$ the reduced bending stiffness. For $\kappa_{bend} = 0$ the third eigenfrequency goes to zero as well. By numerically solving

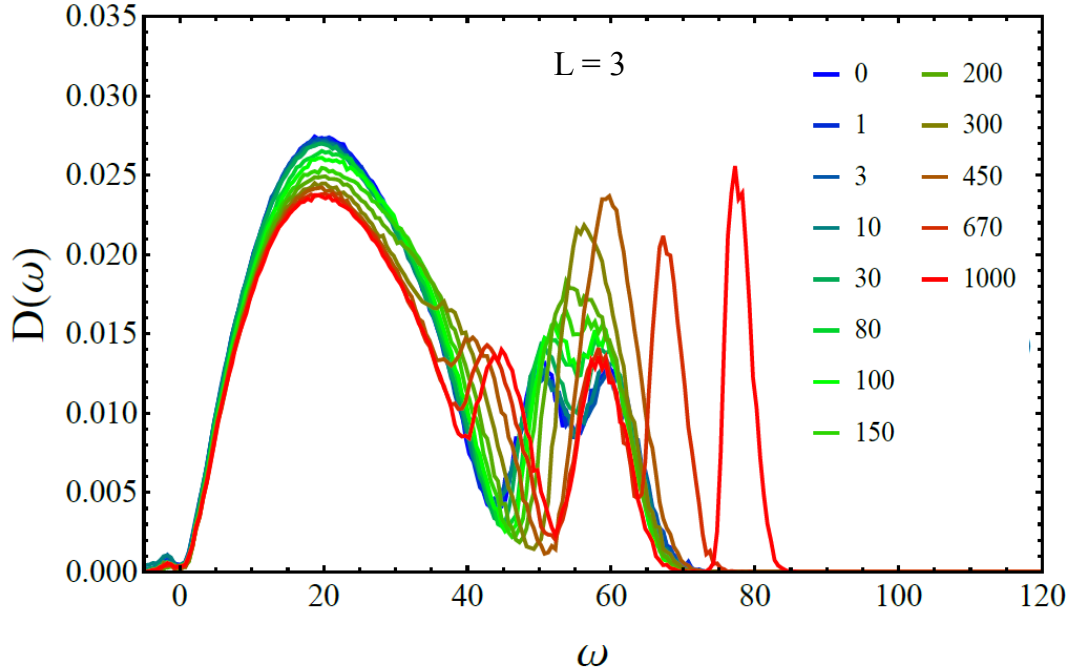


Figure 4.5: VDOS of chain with $L = 3$. We can see the transition from flexible (blue) to stiff (red) as described in the text.

for the eigenvectors of those three eigenfrequencies we can evaluate the weight of perpendicular and along chain motion introduced in (4.7). As the chain is inherently flat, no rocking motion can be introduced by FENE or bending interaction. In Fig. 4.5 we see the full VDOS for various bending stiffness. We can separate three general shapes of the VDOS:

- (i) For the rather flexible case $\kappa_{bend} < 100$ we see the previously described split in low frequency LJ-sea and the high frequency backbone part. The high frequency part shows two broad peaks, caused by contributions from the two eigenfrequencies $\omega_{1,2}$ with distributed angle.
- (ii) As the bending stiffness increases the two peaks merge into one high peak at around $\kappa_{bend} = 300$, while a shoulder forms at the right side of the LJ-peak.
- (iii) For very high bending stiffness $\kappa_{bend} > 500$, the high frequency peak splits again with one peak staying at $\omega \approx 60$ and the other moving to ever higher frequencies. At the same time the shoulder at the LJ peak develops into a separated peak, whose positions shows a convergent behaviour.

By looking at the motion patterns and the analytical results for $L = 3$ we can make sense of this behaviour. In Fig. 4.7 we can see one VDOS for each of the three

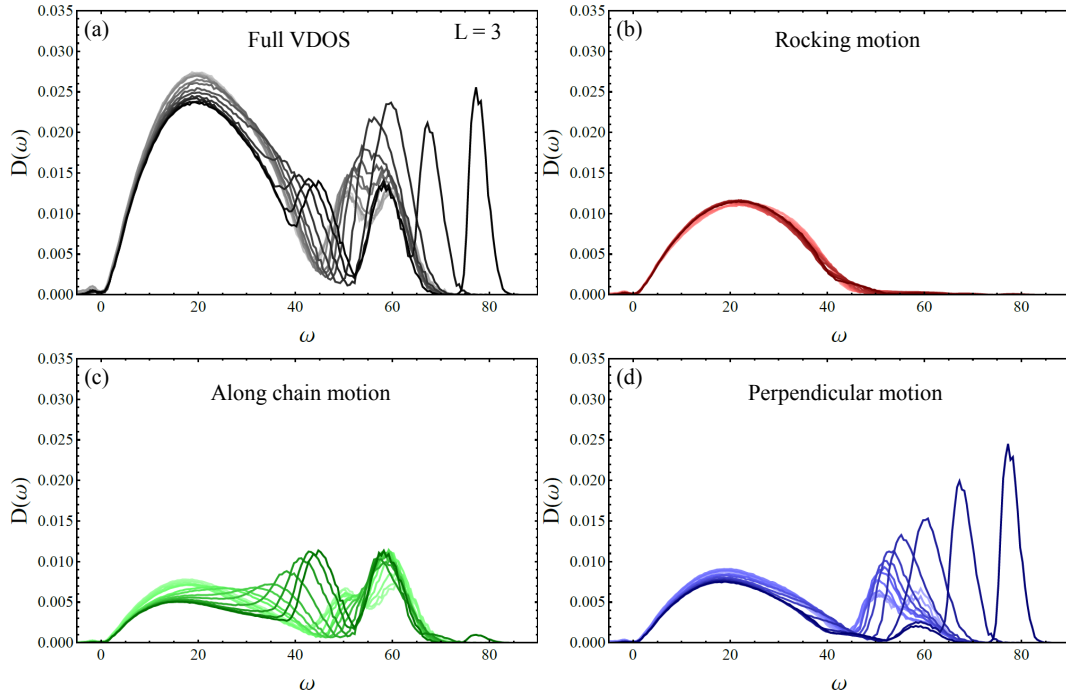


Figure 4.6: VDOS of chains with $L = 3$ for various κ_{bend} . Lighter shades of colour indicate lower bending stiffness. In (b-d) we can see the partial VDOS for the three different motions defined in 4.3.1. Rocking motion only occurs in the LJ-part of the spectrum. The high frequency peak almost only consists of perpendicular motion, while the other two peaks are dominated by along chain motion.

cases mentioned above at $\kappa_{bend} = 1, 300, 1000$, including the partial VDOS for the three motions. Next to it are plots showing the bending stiffness dependence of the three eigenfrequencies $\omega_{1,2,3}$ and the relative contribution of perpendicular and along chain motion for each. As the bending interaction cannot cause rocking motion in a chain of length $L = 3$, it makes sense that the partial VDOS of rocking motion does not change qualitatively with the bending stiffness. The behaviour of $\omega_{1,2,3}$ is well reflected in the numerical results for the VDOS although ω_3 is hidden in the LJ peak for low κ_{bend} . The shoulder forming at around $\kappa_{bend} = 300$ are therefore just the ω_3 modes moving out of the LJ peak. This interpretation becomes even more solid when we take a look at the motion ratio of the three peaks at $\kappa_{bend} = 1000$. They correspond exactly to the predicted ratios from the model, with $\omega_{1,3}$ being dominated by along chain and ω_2 by perpendicular motion. We can therefore conclude that the total VDOS is a superposition of the LJ peak with three peaks caused by the FENE and bending interaction. The VDOS

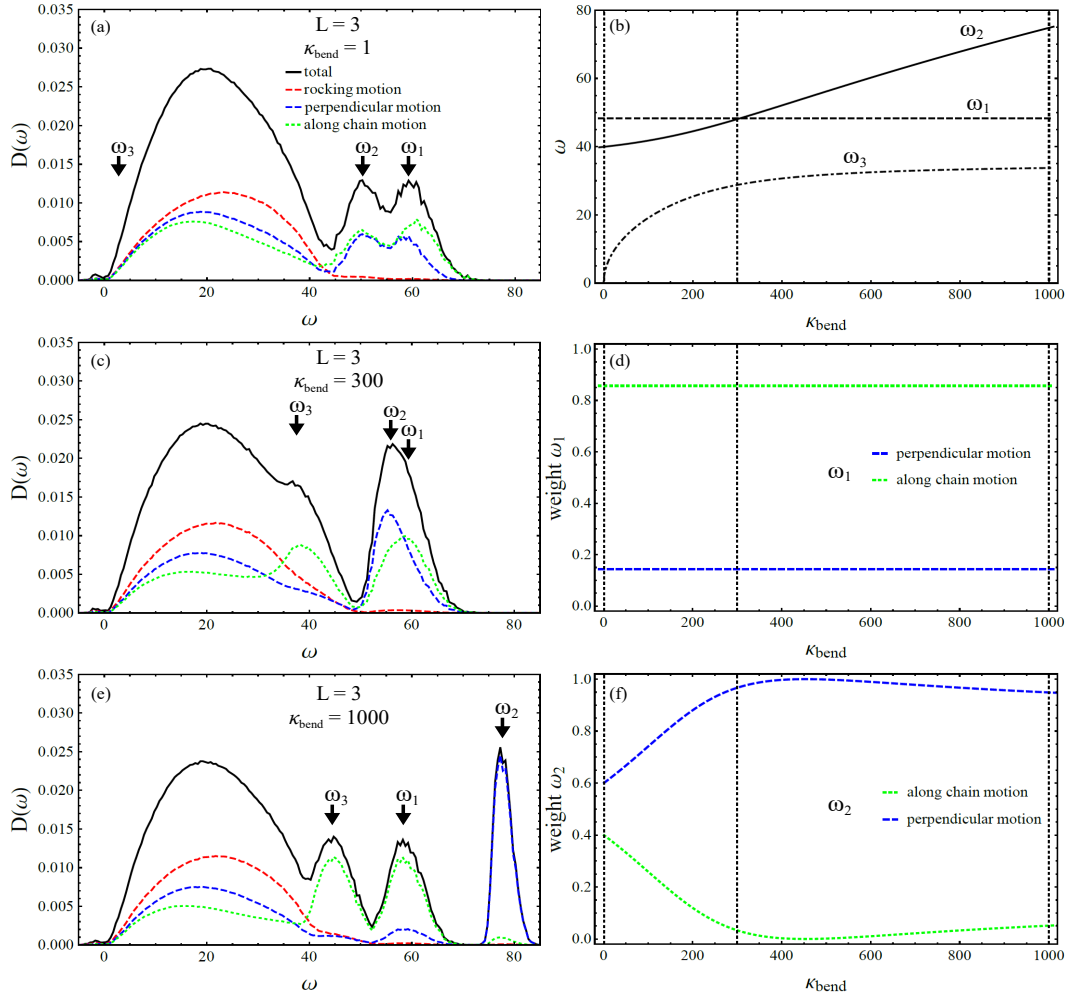


Figure 4.7: Illustration of the three regimes (i-iii) described in the text. (b) Dependence of the three non-zero eigenfrequencies of a chain with $L = 3$, obtained from (4.8), on κ_{bend} . (d,f) Contribution weights for along chain and perpendicular motion for ω_1 and ω_2 . The weights of ω_3 are inverted compared to ω_2 . Vertical dashed lines in (b,d,f) indicate sample values of κ_{bend} for which the VDOS are shown in (a,c,e). As we can see the qualitative behaviour of our real systems with $L = 3$ is well captured by the analytical model, both in terms of frequency and motion weight evolution. The actual frequencies differ due to the bulk of LJ interactions acting on each particle which pushed the bond energy, and therefore frequency, to higher values.

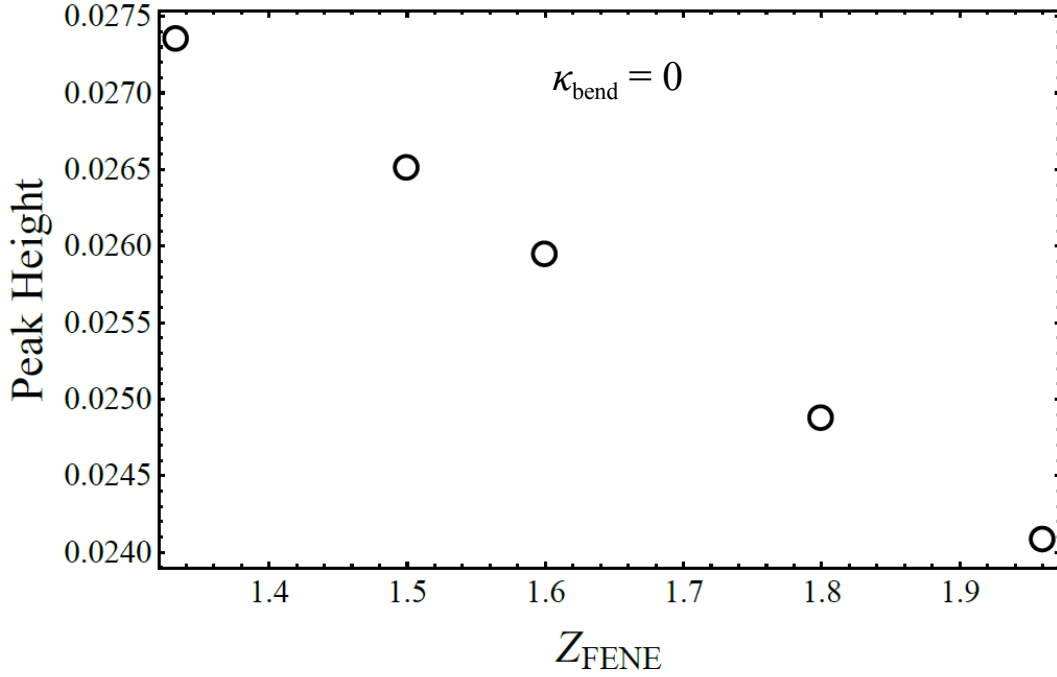


Figure 4.8: Height of the LJ-peak depending on the connectivity of FENE bonds $Z_{FENE} = (L - 1)/L$ for flexible chains.

including partial spectra are shown for all κ_{bend} in Fig. 4.6 to further illustrate the continuous change according to the described mechanism. The position of the peaks is governed by (4.8) and they are broadened by the distribution of bond angles and FENE bond lengths. The deviation from the predicted position is a result of the inter chain LJ interaction which is neglected in the model. This adds a non-neglectable amount of bond energy to each triplet which shifts the frequency to higher values. Furthermore we can draw a connection between high frequency perpendicular motion and the bending stiffness as well as along chain motion at intermediate frequencies with FENE interaction, which will become important for longer chains, where no analytical solvable model exists.

4.3.4 VDOS for chains with $L > 3$

Next we will look at longer chains and explain changes due to chain length as well as translate the insights from $L = 3$ to those systems. In Fig. 4.9 we see the spectra of all our systems. The first thing to notice is that the general dependence on κ_{bend} does not depend on the chain length, meaning we can observe the three cases (i-iii) from above for all lengths in the same regimes of the bending stiffness.

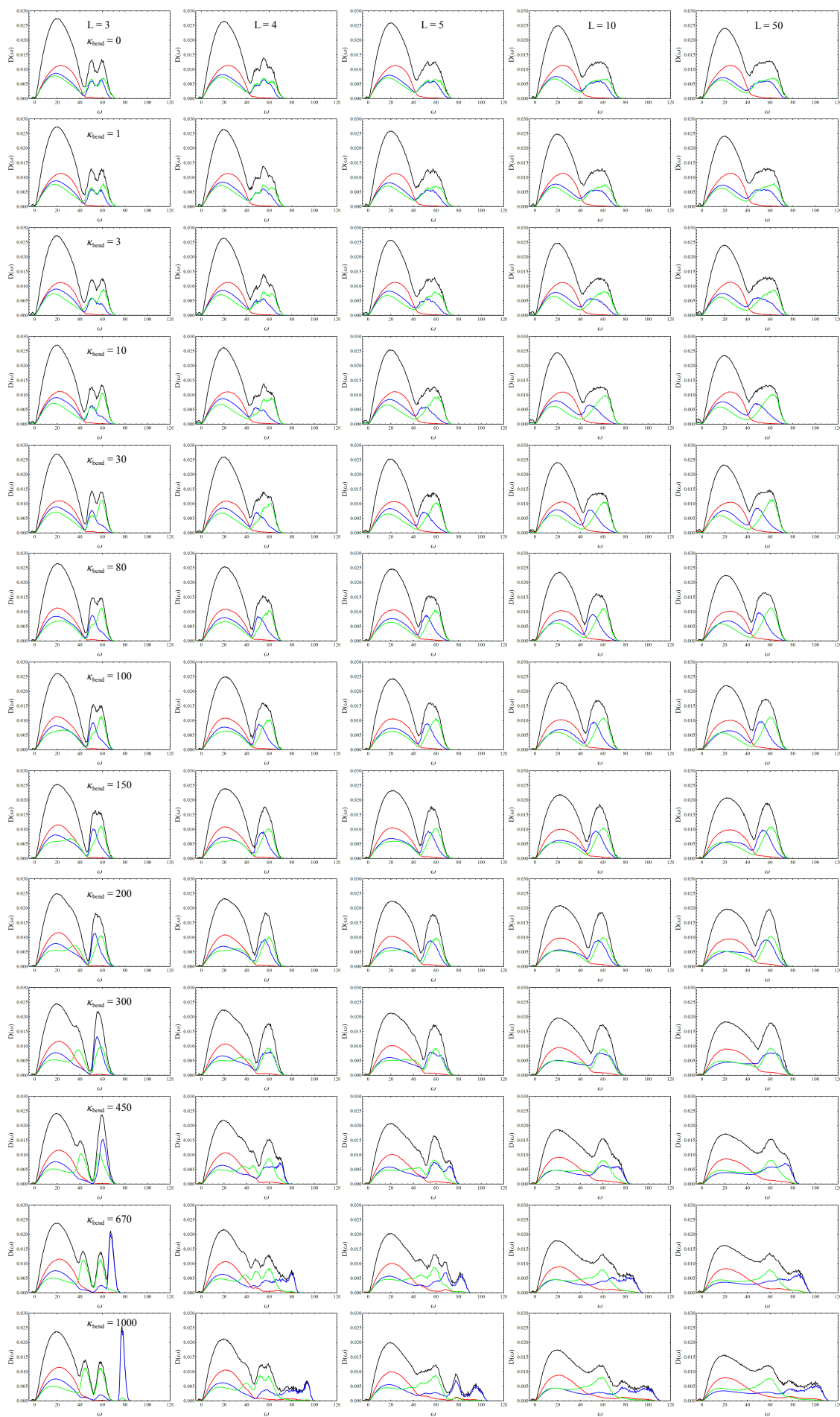


Figure 4.9: VDOS of all systems including partial spectra of motions.

There are however differences within those regimes for different lengths.

Flexible chains

For the flexible case we can look at the model system described in Appendix A.3. With longer chain length we get more non-zero values. This leads to the two peaks for $L = 3$ as described above. For $L = 4$ we have three eigenvalues, of which the middle one does not depend on the bond angles in the chain, leading to the high frequency part of the VDOS observed in Fig. 4.9. One pronounced peak in the middle with two smaller ones on the sides. For even longer chains this trend continues with the high frequency part forming a continuous peak due to bond angle distributions in the system. VDOS of the flexible systems are shown in Fig. 4.4 for all lengths. We can see that the LJ peak decreases with length, since longer chains have more FENE bonds, which add more high frequency modes to the system. The rate of change however slows down with length, as there are less FENE bonds added for a fixed number of particles. In Fig. 4.8 we can see the peak height plotted against the FENE connectivity Z_{FENE} of the system, showing a clear linear dependence. As the connectivity has an upper boundary $Z_{FENE} = 2$, which is the case of all particles in the system belonging to one chain, the VDOS of this configuration is a limiting case. For $L = 50$ we are already very close to this spectrum with the LJ peak only being $\sim 1\%$ higher than the extrapolated limiting case. This makes the system with $L = 50$ a reasonable approximation for the limiting case and shows that there is not much to gain from analysing longer chains in terms of vibrational spectra.

Stiff chains

In Fig. 4.10 we can see the VDOS for $\kappa_{bend} = 1000$ and all lengths. For $L = 4$ one would expect five peaks, as there are five interactions per chain (three FENE bonds and two bending interactions). Indeed we can make out three peaks dominated by along chain motion for $35 < \omega < 70$ and two peaks dominated by perpendicular motion for $\omega > 70$. The latter two are more spread out as the eigenvalues of chains with bending interaction are in general not invariant under rotations around individual bonds. In the case of $L = 4$ they depend on the relative orientation of the two outer bonds in the chain. This seems to affect the high frequency

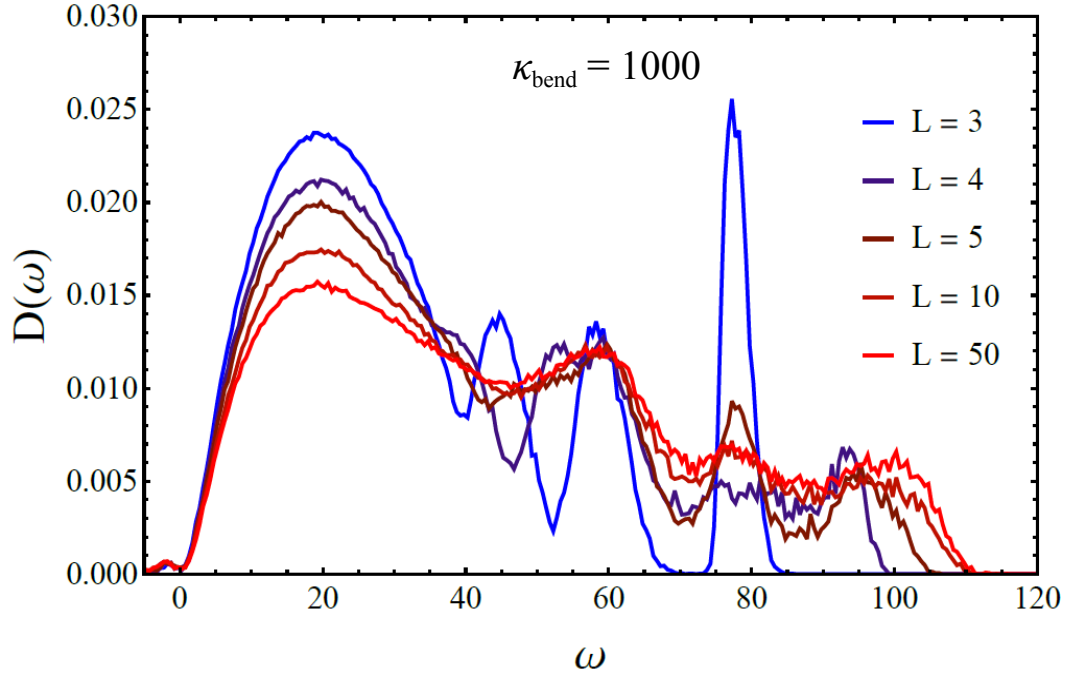


Figure 4.10: VDOS of stiff chains. One can clearly see the loss of peak structure for longer chains.

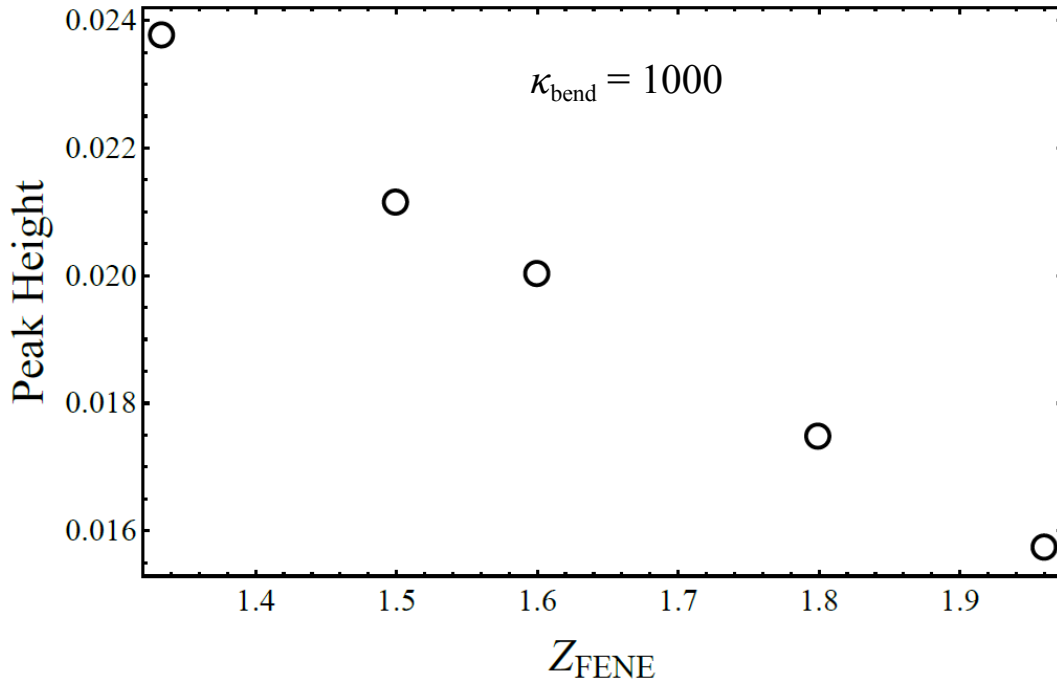


Figure 4.11: Height of the LJ-peak depending on the connectivity of FENE bonds $Z_{\text{FENE}} = (L - 1)/L$ for stiff chains.

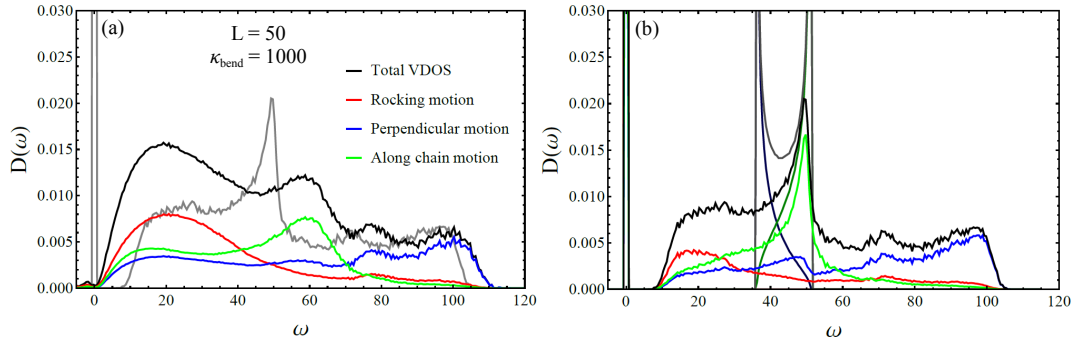


Figure 4.12: (a) VDOS for $L = 50$ and $\kappa_{bend} = 1000$ in black with its partial spectra for the three motions. In gray we see the VDOS of a freely rotating chain of length $L = 5000$ with the same parameters as our system. We can make out the same features as for our simulated system only without the LJ-regime. Due to the missing LJ interaction the 'real' spectrum is shifted towards higher values with the discrepancy being smaller for higher frequencies. (b) VDOS of the freely rotating chain with its motion spectra. We can see more to the $L = 50$ VDOS from our system. In gray we can see the VDOS from (4.9) with its partial spectra. As described in the text the behaviour around $\omega = 60$ can be traced back to this model system.

modes more, which is in agreement with our interpretation of high frequency perpendicular modes being closely related to bending interaction.

For longer chains we get more and more possible frequencies, which changes the peak structure of the VDOS to a more continuous spread out distribution. As can be seen in Fig. 4.11 the LJ peak decreases in a similar way as for flexible chains linearly with Z_{FENE} but shows lower values. This can be explained by the fact that in addition to the high energy FENE bonds, stiff chains also have high energy bending interaction, which further shifts modes from the low frequency LJ peak to higher frequencies. As for flexible chains the VDOS of stiff chains tends towards a limiting distribution, which is well approximated by our system with $L = 50$. One interesting feature is the peak at around $\omega = 60$ that appears for all lengths at high bending stiffness. For $L = 3$ we already connected it to one of the characteristic eigenfrequencies ω_1 of the system. In systems with long chains, it originates from the regular zig-zag backbone structure of stiff chains. An analytic description for this configuration without bending stiffness is given in Appendix A.3 For long chains it has the VDOS:

$$D(\omega) = \frac{2}{\pi} \frac{\omega}{\sqrt{4 \frac{\kappa^2}{m^2} \cos^2 \theta - (\omega^2 - 2 \frac{\kappa}{m})^2}} \quad (\theta \neq \pi/2) \quad (4.9)$$

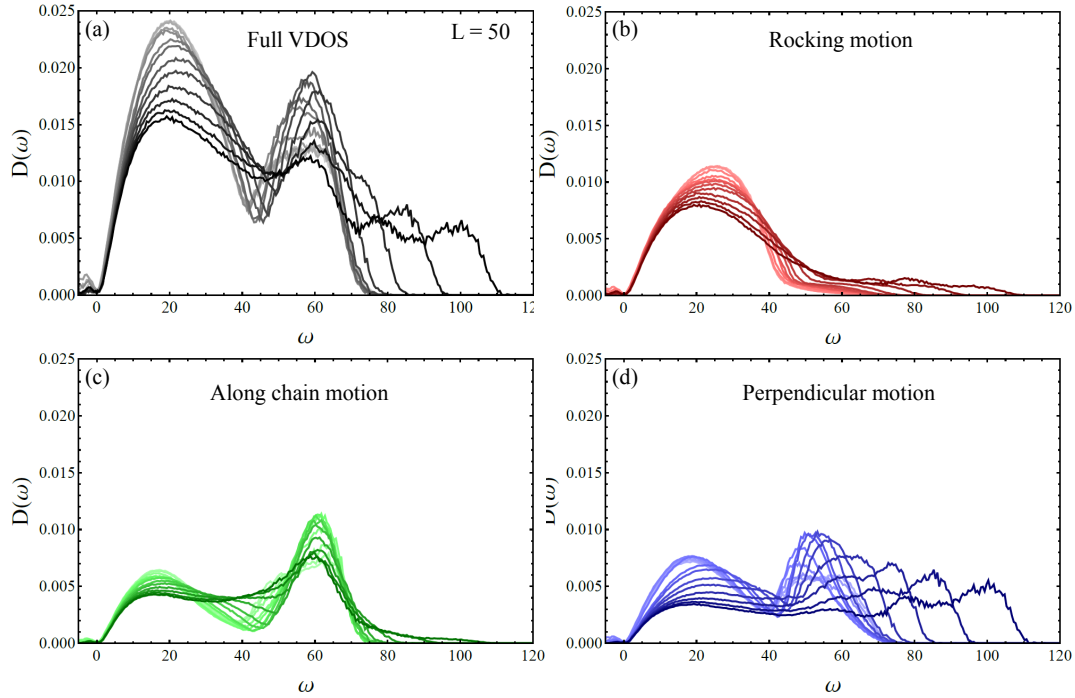


Figure 4.13: VDOS of chains with $L = 50$ for various κ_{bend} . Lighter shades of colour indicate lower bending stiffness. In (b-d) we can see the partial VDOS for the three different motions defined in 4.3.1. Rocking motion mostly occurs in the LJ-part of the spectrum, although the freely rotated structure of the chains causes rocking motion in the high frequency part as well. The high frequency regime almost only consists of perpendicular motion, while the peak at $\omega = 60$ is dominated by along chain motion.

As shown in Appendix A.3 the eigenfrequencies are independent under rotations around single FENE bonds, which makes this result so useful for our model as stiff chains can also rotate freely around each FENE bond. Of course, in the real system the regular structure is enforced by the bending interaction but we can still translate insights from the hypothetical model to our real system. In Fig. 4.12 we can see the VDOS of the regular freely rotating zig-zag chain with $\kappa_{bend} = 1000$ and $L = 5000$ in comparison with our system for $L = 50$ and the model VDOS form (4.9). It is evident that the features of the real system have corresponding parts in the model system aside from the missing LJ peak which also leads to a shift in the frequencies to higher values. We can further verify that the high frequency perpendicular motion modes are a result of the bending interaction, while the peak at $\omega = 60$ is caused by the FENE interactions along the backbone of the chain in combination with the regular structure of the chain,

as it corresponds perfectly to the right peak of (4.9) at $\omega = \frac{\kappa}{m}(2 - 2\cos\theta)$. This peak position does not coincide with the frequency of ω_1 from the $L = 3$ model in (4.8). However, they appear at the same position for the real systems as the bulk of LJ interaction has higher influence on FENE modes of shorter chains. The reason for this is most likely an increase in influence for modes closer to the LJ peak, as they correspond to systems with lower FENE bond energy per particle. It is therefore the ratio $\kappa_{FENE}/\kappa_{LJ}$ that keeps this peak at a steady position for different lengths and bending stiffness.

Transition from flexible to stiff chains for $L = 50$

Finally we take a look at how the VDOS and contributions from different motions change with κ_{bend} . In Fig. 4.13 we see the full VDOS for various bending stiffness as well as the partial VDOS for the three motion patterns. As stated earlier there are many similarities between the case of $L = 3$ and $L = 50$ in terms of how modes are shifted. We start with a well separated LJ and FENE part for flexible chains. As the bending stiffness is increased modes associated with perpendicular motion are shifted towards higher frequencies, leading to the formation of a single high peak when they reach the characteristic frequencies of the FENE interaction at $\omega = 60$. For stiffer chains the bending modes are shifted to higher frequencies with mostly perpendicular motion. One difference between chains of length $L = 3$ and longer chains is that strong bending interactions also cause rocking motion. This is due to the fact that in-plane motions in one triplet of the chain is, in general, out-of-plane motion from the perspective of neighbouring triplets. Aside from that we can again see the association of perpendicular motion with bending interaction, along chain motion with FENE interaction and rocking motion with LJ interaction as described in 4.3.3, although the peak structure has changed into a continuous spectrum.

4.4 Shear modulus

Next we study the influence of our parameters (bending stiffness and length) on the shear modulus of the systems. To do this we first take a look at the correlator function $\Gamma(\omega)$ calculated from (1.19) and its product with the VDOS $D(\omega)\Gamma(\omega)$ to compare it with our previous findings from 2. We then go further on and present the results for the static shear modulus calculated according to the framework of

non-affine lattice dynamics (1.17).

4.4.1 The non-affine correlator function

In Fig. 4.14 the correlator functions for $L = 3$ and $L = 50$ are shown covering the complete range of bending stiffness explored in this work. Both systems have the same qualitative behaviour with the longer chains having a higher peak for very stiff chains. This makes sense as $\Gamma(\omega)$ includes the affine force field, which is proportional to the force constant of the corresponding potential. More high energy bonds result in a higher affine force field and a higher correlator function. Unlike for our depleted lattice systems from Chap. 2 we can see no power law behaviour for small ω . Furthermore we can make out four regimes. For $\omega < 30$ we observe a gradual increase of the correlator with the frequency as well as with the bending stiffness. At $\omega \approx 40$ the correlator of the more flexible systems increases about one order of magnitude. Since this jump is not apparent in the correlator of stiff chains it leads to non-monotonic behaviour for $40 < \omega < 60$, where with increasing bending stiffness $\Gamma(\omega)$ first decreases and then increases again. In the inset we see the dependence of $\Gamma(\omega = 45)$ on the bending stiffness showing the non-monotonic behaviour. For higher frequencies $\omega > 60$ the behaviour of the correlator becomes monotonic again. As discussed before, the increasing bending stiffness creates more high frequency modes which have the highest values of $\Gamma(\omega)$ associated with them.

Next we look at the product $D(\omega)\Gamma(\omega)$ for which results are shown in Fig. 4.14. We see the same $D(\omega)\Gamma(\omega) \sim \omega^2$ scaling as for the depleted lattices. Aside from that the regimes are the same as for $\Gamma(\omega)$ discussed before. We will next study the integrand of the non-affine integral (1.20) $I(\omega) = D(\omega)\Gamma(\omega)/\omega^2$ as this quantity gives us insight into what each frequency contributes to the non-affine shear modulus G^{NA} . We see in Fig. 4.14 that for low frequencies this quantity follows a linear function $I(\omega) = a(\omega_0 - \omega)$ with some constants a, ω_0 . This represents the fitting from (2.21) as :

$$D(\omega)\Gamma(\omega) = \omega^2 I(\omega) = a\omega^2(\omega_0 - \omega) \quad (4.10)$$

In this case ω_0 can be seen as the a kind of Debye frequency for the LJ-part, although the full spectrum is more complicated so that the fitting from before

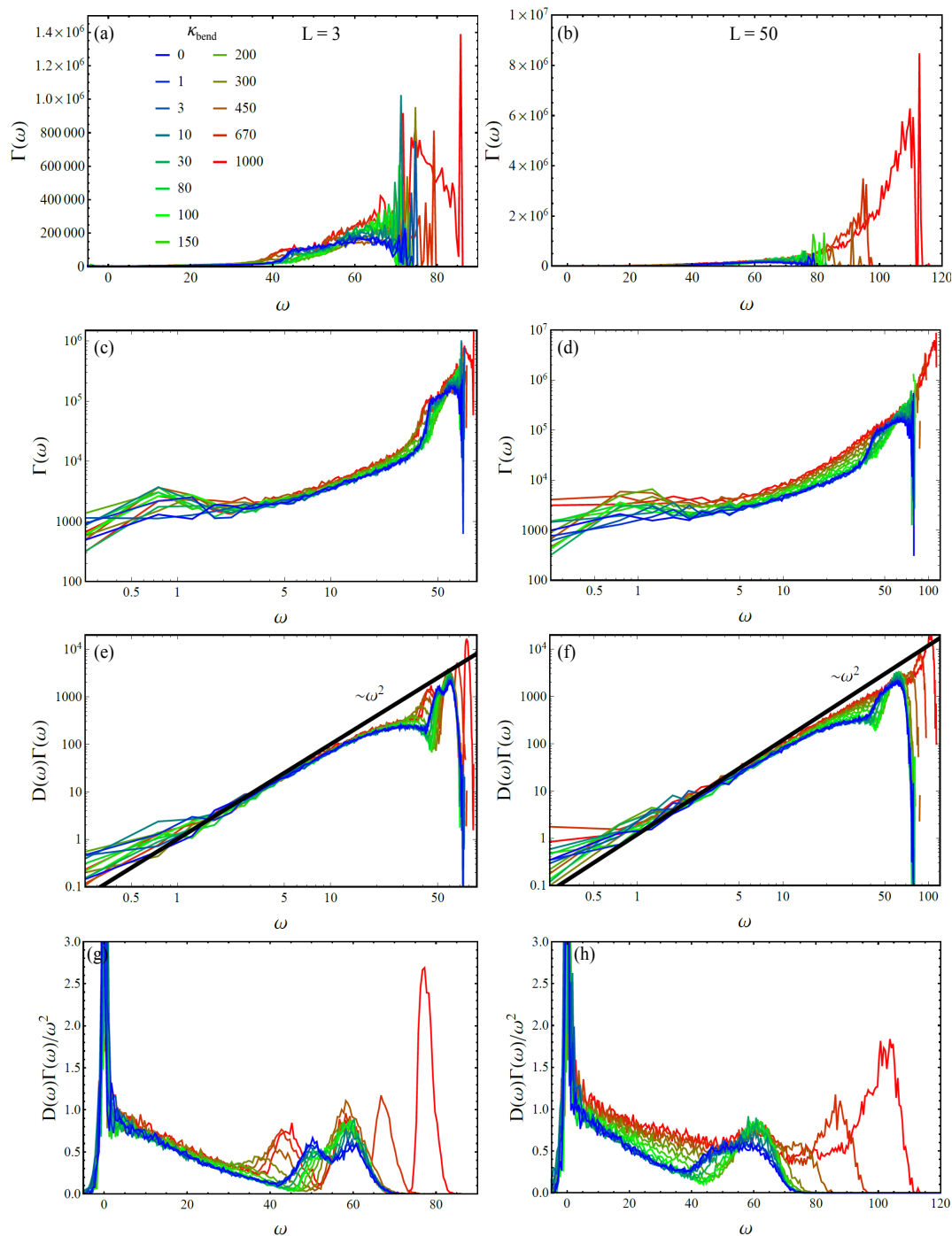


Figure 4.14: (a-d) Non-affine correlator $\Gamma(\omega)$ in normal and logarithmic plot. Results for $L = 3$ are shown on the left. We can see that the correlator shows no power law scaling at low frequencies. (e,f) The product $D(\omega)\Gamma(\omega)$ scales like $\sim \omega^2$, which we also found for depleted fcc lattices in Chapter 2. (g,h) Non-affine integrand $D(\omega)\Gamma(\omega)/\omega^2$ of our systems.

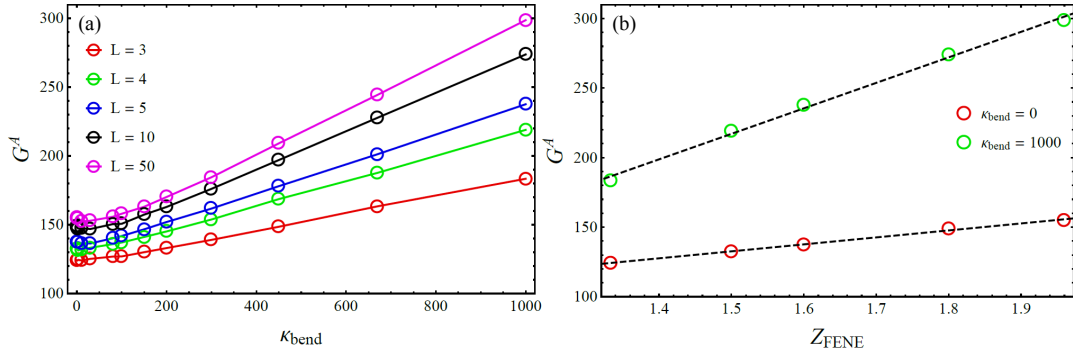


Figure 4.15: (a) Affine shear modulus G^A of our systems in dependence of the bending stiffness. (b) Dependence of G^A on the connectivity of FENE bonds. We see a linear behaviour for both $\kappa_{bend} = 0$ and $\kappa_{bend} = 1000$.

cannot be used.

4.4.2 Static shear modulus

As discussed before, the fact that our systems are not exactly at a local energy minimum might lead to problems when calculating the static shear modulus. We will first look at the affine part, which is well defined even with net forces in the system as it just depends on the energy stored by the affine deformation. The explicit contributions from pair and angular bonds are given in the Appendix A.1. Therefore the results for G^A shown in Fig. 4.15 show the expected behaviour with the modulus increasing for higher bending stiffness and longer chains, as both increase the bond energy in the system and make it harder to deform. G^A shows a good convergence with the deviation $\sigma = \sqrt{\langle (G^A)^2 \rangle - \langle G^A \rangle^2}$ never exceeding a relative value of 4% of the average affine shear modulus.

The same is not true for the non-affine shear modulus G^{NA} . In Fig. 4.16(e) the results calculated from the framework derived in (1.18) and averaged over 5 realisations are shown together with the corresponding error bars. In contrast to the affine part the non-affine shear modulus shows no good convergence which renders the average results meaningless. We can relate those uncertainties to the fact that our systems are not fully relaxed which prevents the accurate calculation of the non-affine displacements. The same is true for the total shear modulus.

To get meaningful results for G we look at the complex modulus $G^*(\Omega)$. We have already established that the affine shear modulus G^A shows reliable results. Since we know that $G^*(\infty) = G^A$ we can be sure that the high frequency

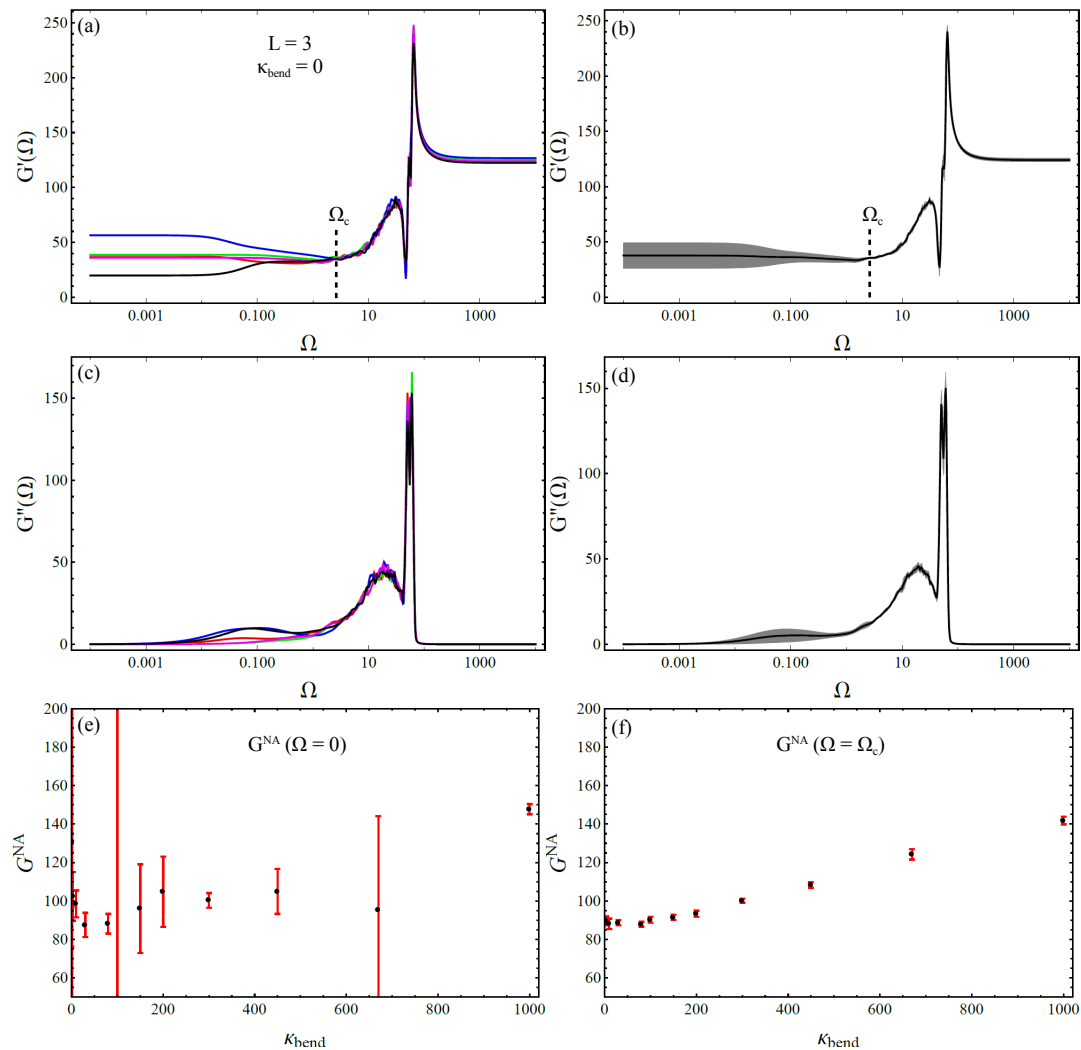


Figure 4.16: (a,c) Shown are 5 different realisations of $G'(\Omega)$ and $G''(\Omega)$ for $L = 5$ and κ_{bend} . We can clearly see the high fluctuation of $G'(\Omega > \Omega_c)$. (b,d) Mean value (black) of the systems with 1- σ error bar (gray). (e,f) average non-affine shear modulus of systems with $L = 3$ calculated according to (1.18) (left) and from $G'(\Omega_c)$ (right).

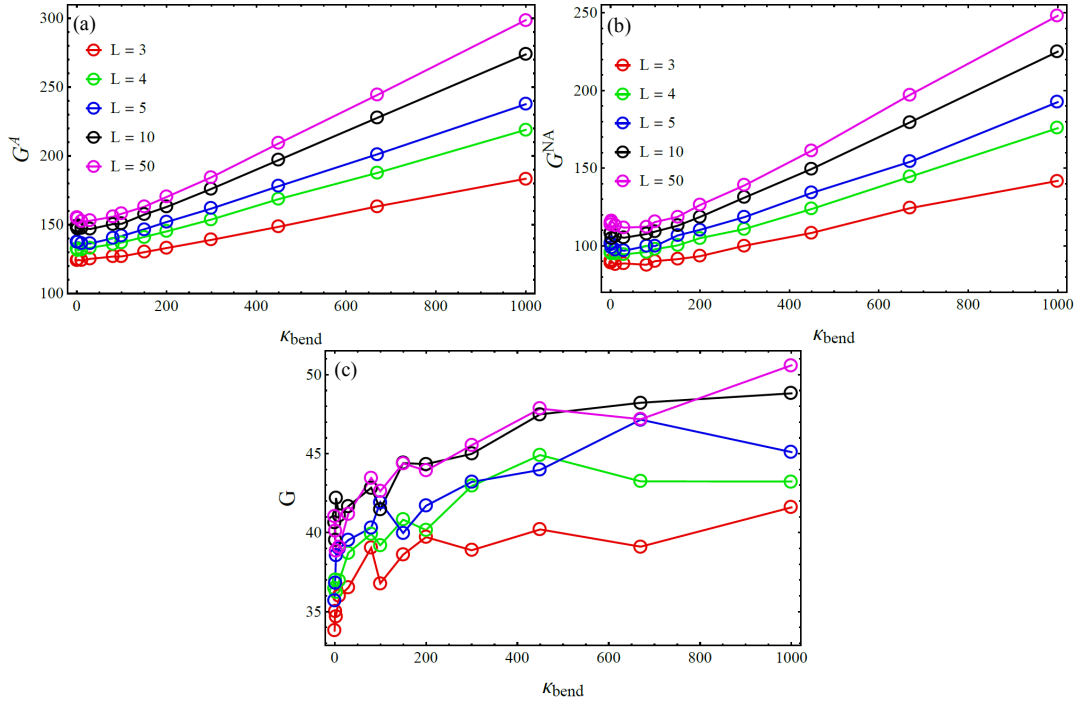


Figure 4.17: (a) affine shear modulus of our systems. (b) Non-affine shear modulus calculated from $G'(\Omega_c)$. (c) Total shear modulus calculated from $G'(\Omega_c)$.

modulus is accurate as well. At some critical frequency Ω_c that accuracy will be lost as the complex modulus goes to $G^*(0) = G$. in Fig. 4.16 we can see the results of individual realisations for $L = 3$, $\kappa_{bend} = 0$ and friction $\nu = 1$. We verify the good convergence at high Ω as predicted and the sudden increase of fluctuations at $\Omega_c \approx 1$. To aid clarity we have plotted the same results averaged over the realisations with continuous $1-\sigma$ error bar. We will use the approximation $G \approx G^*(\Omega_c)$ to study the behaviour of the static shear modulus G . We will therefore restrict ourselves to low friction as it shifts the transition $G \rightarrow G^A$ to higher frequencies, giving the value $G^*(\Omega_c)$ more reliability as it lays further in the low Ω plateau regime.

In Fig. 4.16 we can see that the error bars of the values of G^{NA} extracted from $G^*(\Omega)$ are much smaller compared to the error bars from G^{NA} calculated from (1.18). Additionally the values of G^{NA} show a smoother behaviour. Although the total shear modulus G , shown in Fig. 4.17 still shows some noise, it has a clear trend towards a plateau at high κ_{bend} . We can conclude from this that increasing the bending stiffness has a diminishing return in terms of shear modulus. This makes sense as at some point the stiffness will cause the FENE bonds to deform

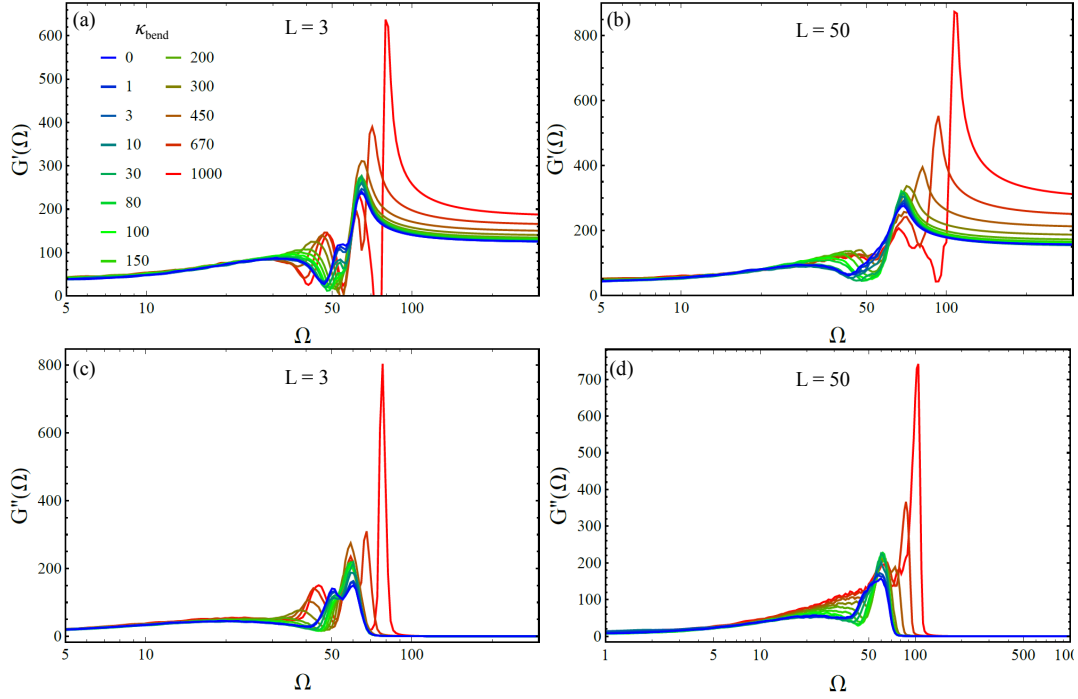


Figure 4.18: Real and imaginary part of the complex shear modulus $G^*(\Omega)$ for $L = 3$ and $L = 50$ with varying κ_{bend} .

instead and since κ_{FENE} is independent of κ_{bend} there will be no change in required energy for shear deformation after this point.

4.4.3 Complex shear modulus

As the VDOS shows a very interesting behaviour it is worthwhile to study the complex shear modulus $G^*(\Omega)$ to see how those features are mirrored in $G'(\Omega)$ and $G''(\Omega)$. Results for $L = 3$ and $L = 50$ are shown in Fig. 4.18. To explore the relation between $G''(\Omega)$ and $D(\omega)$ it is convenient to look at $G''(\Omega)$ on semi-logarithmic scale and restrict the plot range. In $G''(\Omega)$ for $L = 3$ we can identify similar features as in the VDOS, especially the double peak for low κ_{bend} , the static peak at $\Omega \approx 60$ and the developing high frequency peak for large bending stiffness. It is therefore reasonable to look for a connection between $D(\omega)$ and $G''(\Omega)$. We recall the definition from (1.33):

$$G''(\Omega) = \frac{1}{V} \sum_k \frac{\nu \Omega (\Xi \cdot \hat{\mathbf{v}}_k)^2}{(\omega_k^2 - \Omega^2)^2 + \nu^2 \Omega^2} \quad (4.11)$$

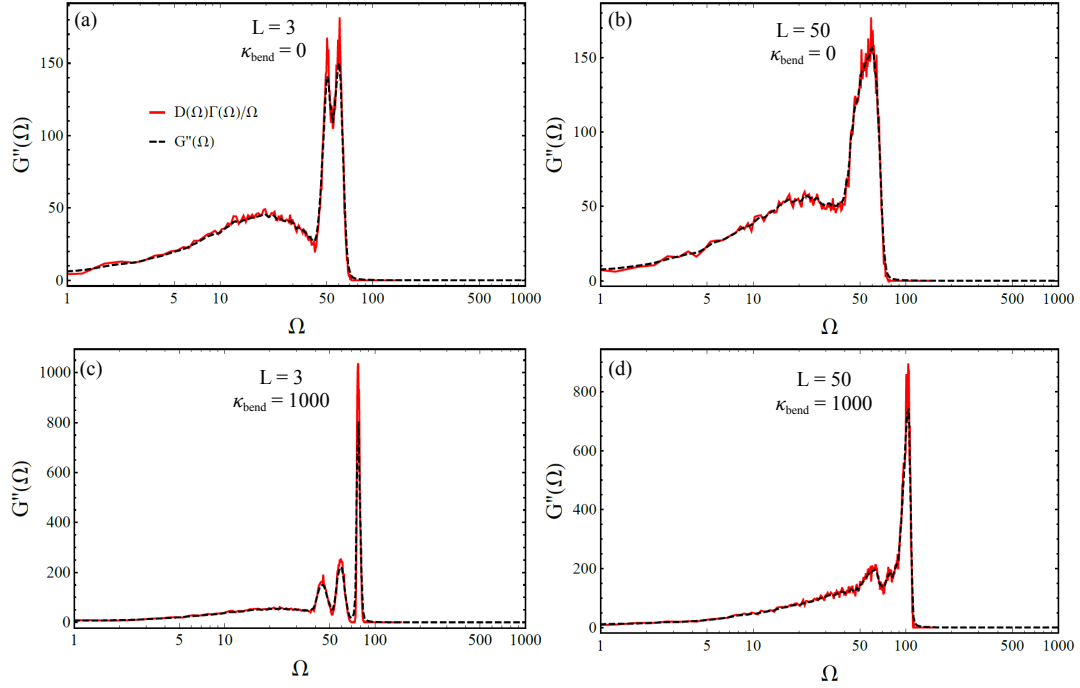


Figure 4.19: Comparison between $D(\Omega)\Gamma(\Omega)/\Omega$ and $G''(\Omega)$ for different lengths L and bending stiffness κ_{bend} . The match is very good, verifying (4.13).

The contribution to the sum are largest when the denominator is small, which for a given Ω is true, if $\omega_k \in [\Omega - \epsilon, \Omega + \epsilon]$. We can write:

$$\begin{aligned}
 G''(\Omega) &\approx \frac{1}{V} \sum_{\omega_k \in [\Omega - \epsilon, \Omega + \epsilon]} \frac{\nu \Omega (\Xi \cdot \hat{\mathbf{v}}_k)^2}{(\omega_k^2 - \Omega^2)^2 + \nu^2 \Omega^2} \\
 &\approx \frac{1}{V} \sum_{\omega_k \in [\Omega - \epsilon, \Omega + \epsilon]} \frac{(\Xi \cdot \hat{\mathbf{v}}_k)^2}{\nu \Omega} \\
 &= \frac{1}{V} N(\omega_k \in [\Omega - \epsilon, \Omega + \epsilon]) \frac{\langle (\Xi \cdot \hat{\mathbf{v}}_k)^2 \rangle_{\omega_k \in [\Omega - \epsilon, \Omega + \epsilon]}}{\nu \Omega}
 \end{aligned} \tag{4.12}$$

In the first step we used $(\omega_k^2 - \Omega^2)^2 \approx 0$ since $\omega_k \in [\Omega - \epsilon, \Omega + \epsilon]$. In the second step we used the random nature of $(\Xi \cdot \hat{\mathbf{v}}_k)^2$, which justifies to use the average of this quantity over a small frequency interval. We further recall that $\langle (\Xi \cdot \hat{\mathbf{v}}_k)^2 \rangle_{\omega_k \in [\Omega - \epsilon, \Omega + \epsilon]} = \Gamma(\Omega)$, which follows from (1.19). This leaves us with

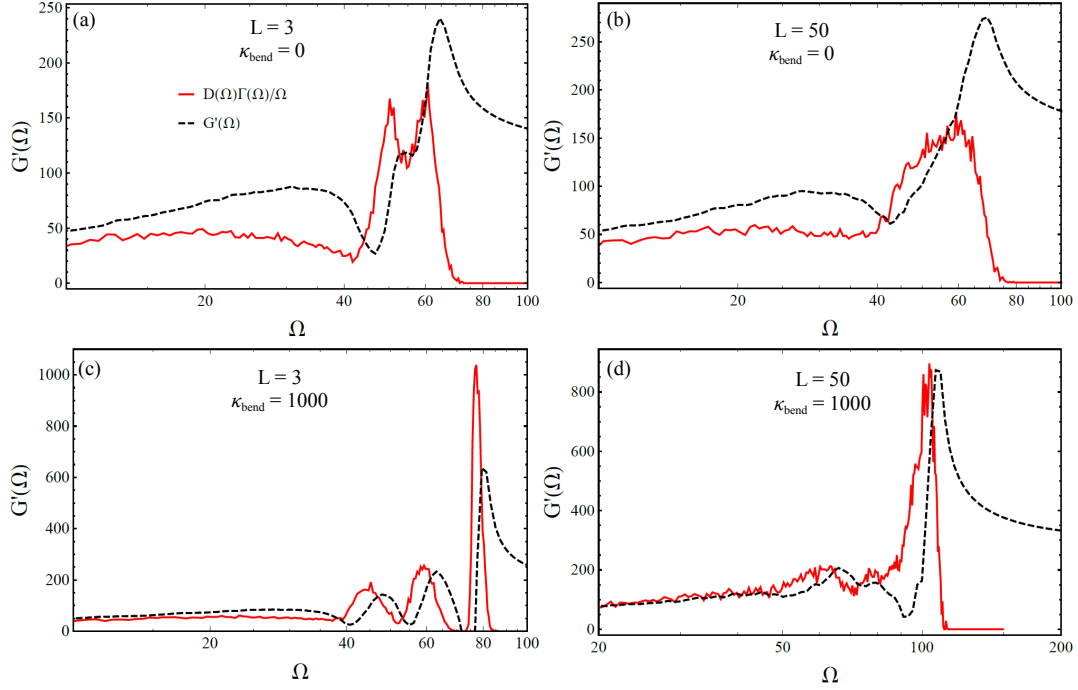


Figure 4.20: Comparison between $D(\Omega)\Gamma(\Omega)/\Omega$ and $G'(\Omega)$ for different lengths L and bending stiffness κ_{bend} . As $D(\Omega)\Gamma(\Omega)/\Omega \approx G''(\Omega)$ we can observe the predicted relation $\frac{d}{d\Omega}G'(\Omega) = G''(\Omega) - x$ (4.15).

the number of modes in a given frequency interval $N(\omega_k \in [\Omega - \epsilon, \Omega + \epsilon])$, which is exactly the definition of the VDOS in this interval $D(\omega) = N(\omega_k \in [\omega - \delta\omega, \omega + \delta\omega])/N_{tot}$ with the total number of eigenfrequencies $N_{tot} = 3N$. We can therefore write:

$$\begin{aligned}
 G''(\Omega) &\approx \frac{1}{V}N(\omega_k \in [\Omega - \epsilon, \Omega + \epsilon]) \frac{\langle (\Xi \cdot \hat{\mathbf{v}}_k)^2 \rangle_{\omega_k \in [\Omega - \epsilon, \Omega + \epsilon]}}{\nu \Omega} \\
 &= \frac{1}{V}3ND(\Omega) \frac{\Gamma(\Omega)}{\nu \Omega} = 3 \frac{N}{V} \frac{D(\Omega)\Gamma(\Omega)}{\nu \Omega}
 \end{aligned} \tag{4.13}$$

The exact values of $G''(\Omega)$ differ of course but the general behaviour matches very well as long as Ω stays in the frequency regime where our system has eigenvalues as we can see in Fig. 4.19. This means we can directly relate the features of $D(\omega)\Gamma(\omega)$ to features in $G''(\Omega)$. Therefore $D(\omega)$ is translated into $G''(\Omega)$ directly in structure but slightly skewed in intensity. We can translate those features to

the real port of the complex modulus $G'(\Omega)$ by using its definition:

$$G'(\Omega) = G^A - \frac{1}{V} \sum_k \frac{(\omega_k^2 - \Omega^2) (\Xi \cdot \hat{\mathbf{v}}_k)^2}{(\omega_k^2 - \Omega^2)^2 + \nu^2 \Omega^2} \quad (4.14)$$

We will now take a look at the derivative of $G'(\Omega)$:

$$\begin{aligned} & \frac{d}{d\Omega} G'(\Omega) \\ &= \frac{1}{V} \sum_k \left[\frac{2\Omega (\Xi \cdot \hat{\mathbf{v}}_k)^2}{(\omega_k^2 - \Omega^2)^2 + \nu^2 \Omega^2} - \frac{\Omega(\omega_k^2 - \Omega^2)[4(\omega_k^2 - \Omega^2) - 2\nu^2](\Xi \cdot \hat{\mathbf{v}}_k)^2}{[(\omega_k^2 - \Omega^2)^2 + \nu^2 \Omega^2]^2} \right] \quad (4.15) \\ &= \frac{1}{\nu} G''(\Omega) - \sum_k \frac{\Omega(\omega_k^2 - \Omega^2)[4(\omega_k^2 - \Omega^2) - 2\nu^2](\Xi \cdot \hat{\mathbf{v}}_k)^2}{[(\omega_k^2 - \Omega^2)^2 + \nu^2 \Omega^2]^2} \end{aligned}$$

We can see that the derivative of $G'(\Omega)$ is directly related to $G''(\Omega)$. The features observed in $G''(\Omega)$ therefore show up in $G'(\Omega)$ as well just shifted. We have visualized this in Fig. 4.20 by comparing $D(\Omega)\Gamma(\Omega)/\Omega$ to $G'(\Omega)$.

4.5 Conclusion

In this work we have studied the effect of chain length and bending stiffness on the Vibrational and elastic properties of simple model chains. We found that light can be shed on the overall complex behaviour of $D(\omega)$ by projecting the eigenvectors on three conveniently chosen motion directions relative to the chain geometry (rocking, perpendicular, along chain) to extract the according partial VDOS. From that we could associate certain frequency regimes with motions and furthermore with our three interaction types (LJ, FENE, bending). We found that bending interaction mostly causes high frequency perpendicular motion, while FENE interaction is closely related with along chain motion at intermediate frequencies present at all lengths and bending stiffness. Rocking motion is closely related to LJ-interaction at low frequencies and bending interaction at high frequencies for $L > 3$. Additionally only a fraction of the modes is affected by the bending stiffness in a way that creates diverging frequencies. Most of the frequencies show

converging behaviour within the frame given by the strength of FENE and LJ bonds.

Length has a diminishing effect on the VDOS as the number of high energy bonds, which creation is the main effect of chain growth, only increases like $\sim (L - 1)/L$ and reaches a plateau quite early.

Another interesting finding is the scaling of the product $D(\omega)\Gamma(\omega)$, which shows a similar behaviour in the LJ-regime as the depleted lattices from Chapter 2 did, hinting at some unifying quality of the scaling $D(\omega)\Gamma(\omega) \sim \omega^2(\omega_0 - \omega)$. The features found in the VDOS directly relate to similar features in the complex shear modulus due to the relation (4.13) and (4.15). We also verified that non-affine lattice dynamics is not directly applicable to systems that are not perfectly relaxed as the fluctuations of the non-affine modulus are not controllable in such cases. We were however able to approximate the static shear modulus from $G'(\Omega)$ by taking a value at the beginning of the low- Ω plateau. From there we can see the same diminishing effect of length for G, G^A, G^{NA} as for the LJ-peak height. We also found that the bending stiffness has a diminishing effect on the shear modulus as it approaches the limit of an infinitely stiff chain with fixed bond angle.

As for our initial motivation to lay the groundwork for a sensor that can measure the growth of polymers in real time, we found that the diminishing effect of length makes it difficult to impossible to distinguish between chain lengths above $\approx 50 - 100$ monomers, which is far below the lengths of industrially used polymers, which have lengths of multiple thousand monomers. We therefore conclude that Raman spectroscopy is not suitable to measure the growth of long polymers.

Conclusion

In this work we have studied multiple disordered systems and analysed the vibrational density of states (VDOS) and the shear modulus in the framework of non-affine lattice dynamics. In the first chapter we looked at defected fcc lattices and compared them to spatially disordered random network as well as compared different types of disordered lattices such as regular depletion where each particle has the same number of bonds, random depletion where each bond has a given probability to be removed and vacancies where whole particles are removed. We found that the VDOS of spatially disordered random networks are almost identical to those of depleted fcc lattices at the same connectivity. This was surprising as structural parameters usually used differ substantially between the two systems and lead us to the conclusion that it is rather inversion symmetry breaking than spatial disorder which influences the VDOS. It also reinforced the practice of using depleted lattices to approximate the properties of disordered systems.

In a second step we compared the different defected lattices by looking at the shear modulus. We found that the type of disorder has no influence on the value of the shear modulus, which is solely defined by the average number of bonds per particle. We also found that the non-affine correlator function, which is a crucial in calculating the complex shear modulus $G^*(\Omega)$, scales like $\Gamma(\omega) \sim \omega^2$. This scaling is robust under changes in the type of disorder as well as the coordination number of the system. The observed change of scaling in the imaginary part of $G^*(\Omega)$, $G''(\Omega)$, can therefore be traced back solely to the changing scaling of the VDOS. This change happens at the critical point $Z = 2d$, where the VDOS changes from $D(\omega) \sim \omega^2 \rightarrow D(\omega) \sim 1$, which is accompanied by a change in $G''(\Omega)$ from $\sim \Omega$ to $\sim \Omega^{1/2}$.

One shortcoming of the used framework is the fact that it only allows for scalings of $G''(\Omega)$ between -1 and 1 , which fails to capture all observed scalings in simulations and experiments. It is therefore necessary to improve on this framework to

reach a broader band of scalings and phenomena.

In the second chapter we looked at the spatial elastic correlations in depleted triangular lattices with long range harmonic interaction that decay with longer distance. We found that the 2-dimensional correlation function of the affine shear modulus G^A shows simple behaviour $C(r, \phi) \sim r^4 \kappa^2 \sin^4 2\phi$, where κ is the spring constant of our harmonic interaction. The angle dependency stems from the different contribution of bonds to G^A depending on their angle, which is ultimately a consequence of the chosen deformation, in this case pure shear. We also see that the spring constant has to decay with $\kappa \sim r^{-3}$ to reproduce the results found in simulations. The correlation the non-affine shear modulus is more complicated. For high bond probabilities the correlation length increases, while for low bond probabilities it decreases. This can be explained by the fact that lattices with low-bond probabilities and decaying spring constant are dominated by the few short ranged bonds with a high spring constant. This leads to local rearrangement during the deformation and a decorrelation of the non-affine shear modulus at long distances.

The correlation of the full shear modulus is now a combination of the affine and non-affine part. We found that at different bond probabilities the local shear modulus is dominated by either the affine or non-affine part, which lead to dominating behaviour of the corresponding correlation pattern. Therefore the correlation length of the shear modulus increases with interaction length for high bond probability and decreases for low bond probability. The correlation pattern changes as well from the structure of the affine part to the one of the non-affine part. In an intermediate regime it resembles non of the two completely and is influenced by the correlation of G^A and G^{NA} , which was not studied in this work.

Since the spatial correlation of elastic moduli has widespread application in phonon scattering and effective medium approximations future work should focus on those correlations between the affine and non-affine part of the modulus and study how they fit into the behaviour of the correlation of the total modulus. Furthermore it is important to study the influence of the correlation patterns on the aforementioned phonon scattering and effective medium theories to get deeper insight into the behaviour of disordered solids.

As a last topic we went from simple central force spring networks to more com-

plex model polymer systems. The initial idea was to study the length dependence of the VDOS in order to lay the groundwork for the development of a sensor technology that measures polymer growth in real time. We then also found it worthwhile to study the spectrum in dependence of the bending stiffness as well as the shear modulus of our systems. One key result was that the chain length has a diminishing effect and no real change is visible in the spectrum above ~ 50 monomers, which speaks against using the vibrational spectrum as a measure for chain growth.

The results were still interesting as the VDOS shows a rich phenomenology depending on the bending stiffness. We found that different motion patterns along the chain correlate with certain interaction types. Rocking motion is mostly related to the inter-chain LJ interaction, while along chain motion is related to the FENE-bonds along the backbone. Bending interaction mostly causes perpendicular motion the the former two and the associated modes shift to higher frequencies as the stiffness is increased. This breakdown of the full VDOS is helpful in understanding the non-trivial behaviour of the full spectrum.

Due to the shortcomings of our framework of non-affine lattice dynamics we were not able to calculate the static shear modulus of our model systems. This again shows the importance of further development of this framework to include the release of at least small internal net forces. However we were still able to get an approximation by using the real part of the complex shear modulus $G'(\Omega)$. With that we found that both length and bending stiffness have diminishing effects on the shear modulus, which approaches a finite limit for one long chain with infinite bending stiffness. We also were able to show how the features of the VDOS translate into the imaginary and real part of the complex shear modulus, which is helpful in studying the latter two under the aspect of changes in the vibrational spectrum.

Appendix

A.1 Explicit form of contributions to H , Ξ and G^A

Here we show the explicit form of the contribution from single pair and bending interactions shown in Fig. A.1. Therefore we evaluate the derivatives from (1.22) whose explicit forms for central potentials are:

$$\begin{aligned}
 H_{nm}^{ab} &= \frac{\partial^2 U(r_{ij})}{\partial r_n^a \partial r_m^b} = \mathbf{c}_{ij} \frac{\partial r_{ij}}{\partial r_n^a} \frac{\partial r_{ij}}{\partial r_m^b} + \mathbf{t}_{ij} \frac{\partial^2 r_{ij}}{\partial r_n^a \partial r_m^b} \\
 \Xi_n^a &= \frac{\partial^2 U(r_{ij})}{\partial r_n^a \partial \gamma} = \mathbf{c}_{ij} \frac{\partial r_{ij}}{\partial r_n^a} \frac{\partial r_{ij}}{\partial \gamma} + \mathbf{t}_{ij} \frac{\partial^2 r_{ij}}{\partial r_n^a \partial \gamma} \\
 G^A &= \frac{\partial^2 U(r_{ij})}{\partial \gamma^2} = \mathbf{c}_{ij} \frac{\partial r_{ij}}{\partial \gamma} \frac{\partial r_{ij}}{\partial \gamma} + \mathbf{t}_{ij} \frac{\partial^2 r_{ij}}{\partial \gamma^2}
 \end{aligned} \tag{A.1}$$

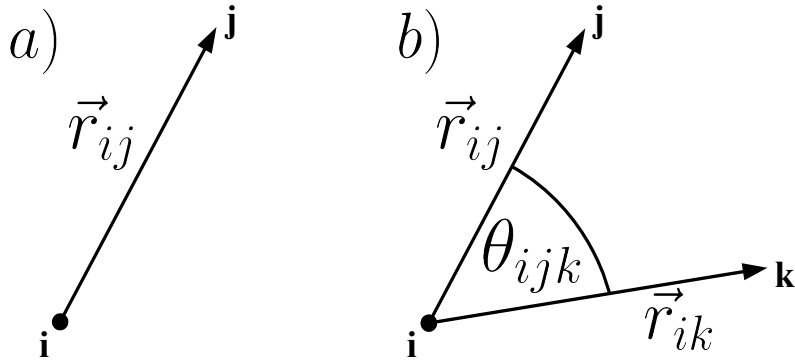


Figure A.1: Sketches of the two types of interaction ((a) pair and (b) angular) considered in this work.

with $r_{ij} = |\mathbf{r}_j - \mathbf{r}_i|$, shear angle γ , tension $\mathbf{t}_{ij} = \partial U(r_{ij})/\partial r_{ij}$ and stiffness $\mathbf{c}_{ij} = \partial^2 U(r_{ij})/\partial r_{ij}^2$ also called effective spring constant κ_{ij} . It is important to note that i, j denote the actual particle labels, while n, m denote the indices of entries in the matrix. To get the explicit expression we have to calculate the five derivatives appearing above:

$$\begin{aligned}\frac{\partial r_{ij}}{\partial r_n^a} &= \delta_{ji}^n \hat{n}_{ij}^a \\ \frac{\partial r_{ij}}{\partial \gamma} &= r_{ij} \hat{n}_{ij}^x \hat{n}_{ij}^y \\ \frac{\partial^2 r_{ij}}{\partial r_n^a \partial r_m^b} &= \frac{\delta_{ji}^n \delta_{ji}^m}{r_{ij}} (\delta_{ab} - \hat{n}_{ij}^a \hat{n}_{ij}^b) \\ \frac{\partial^2 r_{ij}}{\partial \gamma^2} &= -r_{ij} (\hat{n}_{ij}^x \hat{n}_{ij}^y)^2\end{aligned}\tag{A.2}$$

$$\frac{\partial^2 r_{ij}}{\partial r_n^a \partial \gamma} = -\delta_{ji}^n (\hat{n}_{ij}^x \hat{n}_{ij}^y \hat{n}_{ij}^a - (\delta_{ay} \hat{n}_{ij}^x + \delta_{ax} \hat{n}_{ij}^y))$$

Here we used the unit bond vector $\hat{n}_{ij} = \mathbf{r}_{ij}/r_{ij}$ between particle i and j and $\delta_{ji}^n = \delta_{nj} - \delta_{ni}$ with the Kronecker Delta δ . The above expressions are valid both for FENE and Lennard-Jones bonds with the only difference being the stiffness \mathbf{c}_{ij} and tension \mathbf{t}_{ij} that have to be evaluated depending on the potential.

For the angular potential we have a slightly different situation as our main variable in the potential is now the angle between the two bonds $\vec{r}_j - \vec{r}_i$ and $\vec{r}_k - \vec{r}_i$:

$$\theta_{ijk} = \arccos \frac{(\vec{r}_j - \vec{r}_i) \cdot (\vec{r}_k - \vec{r}_i)}{|\vec{r}_j - \vec{r}_i| |\vec{r}_k - \vec{r}_i|} = \arccos A_{ijk}\tag{A.3}$$

Using this we can write:

$$\begin{aligned}
H_{nm}^{ab} &= \frac{\partial^2 U(\theta_{ijk})}{\partial r_n^a \partial r_m^b} = \frac{\mathbf{c}_{ijk} - \mathbf{t}_{ijk} \tan \theta_{ijk}}{\sin^2 \theta_{ijk}} \frac{\partial A_{ijk}}{\partial r_n^a} \frac{\partial A_{ijk}}{\partial r_m^b} - \frac{\mathbf{t}_{ijk}}{\sin \theta_{ijk}} \frac{\partial^2 A_{ijk}}{\partial r_n^a \partial r_m^b} \\
\Xi_n^a &= \frac{\partial^2 U(\theta_{ijk})}{\partial r_n^a \partial \gamma} = \frac{\mathbf{c}_{ijk} - \mathbf{t}_{ijk} \tan \theta_{ijk}}{\sin^2 \theta_{ijk}} \frac{\partial A_{ijk}}{\partial r_n^a} \frac{\partial A_{ijk}}{\partial \gamma} - \frac{\mathbf{t}_{ijk}}{\sin \theta_{ijk}} \frac{\partial^2 A_{ijk}}{\partial r_n^a \partial \gamma} \\
G^A &= \frac{\partial^2 U(\theta_{ijk})}{\partial \gamma^2} = \frac{\mathbf{c}_{ijk} - \mathbf{t}_{ijk} \tan \theta_{ijk}}{\sin^2 \theta_{ijk}} \frac{\partial A_{ijk}}{\partial \gamma} \frac{\partial A_{ijk}}{\partial \gamma} - \frac{\mathbf{t}_{ijk}}{\sin \theta_{ijk}} \frac{\partial^2 A_{ijk}}{\partial \gamma^2}
\end{aligned} \tag{A.4}$$

Here we have used the angular stiffness $\mathbf{c}_{ijk} = \partial^2 U(\theta_{ijk})/\partial\theta_{ijk}^2$ and tension $\mathbf{t}_{ijk} = \partial U(\theta_{ijk})/\partial\theta_{ijk}$. The explicit expressions are obtained by evaluating the derivatives:

$$\begin{aligned}
\frac{\partial A}{\partial r_n^a} &= \frac{\delta_{ji}^n}{r_{ij}} (\hat{n}_{ij} \times (\hat{n}_{ik} \times \hat{n}_{ij}))_a + \frac{\delta_{ki}^n}{r_{ik}} ((\hat{n}_{ik} \times \hat{n}_{ij}) \times \hat{n}_{ik})_a \\
\frac{\partial A}{\partial \gamma} &= (\hat{n}_{ij}^x \hat{n}_{ik}^y + \hat{n}_{ik}^x \hat{n}_{ij}^y) - (\hat{n}_{ij}^x \hat{n}_{ij}^y + \hat{n}_{ik}^x \hat{n}_{ik}^y) \cos \theta_{ijk} \\
\frac{\partial^2 A}{\partial r_n^a \partial r_m^b} &= \frac{\delta_{ji}^n \delta_{ji}^m}{r_{ij}^2} \left[(3 \hat{n}_{ij}^a \hat{n}_{ij}^b - \delta_{ab}) \cos \theta_{ijk} - (\hat{n}_{ij}^a \hat{n}_{ik}^b + \hat{n}_{ik}^a \hat{n}_{ij}^b) \right] \\
&\quad + \frac{\delta_{ji}^n \delta_{ki}^m}{r_{ij} r_{ik}} \left[\delta_{ab} + \hat{n}_{ij}^a \hat{n}_{ik}^b \cos \theta_{ijk} - (\hat{n}_{ij}^a \hat{n}_{ij}^b + \hat{n}_{ik}^a \hat{n}_{ik}^b) \right] \\
&\quad + \frac{\delta_{ki}^n \delta_{ji}^m}{r_{ij} r_{ik}} \left[\delta_{ab} + \hat{n}_{ik}^a \hat{n}_{ij}^b \cos \theta_{ijk} - (\hat{n}_{ij}^a \hat{n}_{ij}^b + \hat{n}_{ik}^a \hat{n}_{ik}^b) \right] \\
&\quad + \frac{\delta_{ki}^n \delta_{ki}^m}{r_{ik}^2} \left[(3 \hat{n}_{ik}^a \hat{n}_{ik}^b - \delta_{ab}) \cos \theta_{ijk} - (\hat{n}_{ij}^a \hat{n}_{ik}^b + \hat{n}_{ik}^a \hat{n}_{ij}^b) \right] \\
\frac{\partial^2 A}{\partial \gamma^2} &= \left[(\hat{n}_{ij}^x \hat{n}_{ij}^y + \hat{n}_{ik}^x \hat{n}_{ik}^y)^2 + 2 (\hat{n}_{ij}^x \hat{n}_{ij}^y)^2 + 2 (\hat{n}_{ik}^x \hat{n}_{ik}^y)^2 \right] \cos \theta_{ijk} \\
&\quad - 2 (\hat{n}_{ij}^x \hat{n}_{ik}^y + \hat{n}_{ik}^x \hat{n}_{ij}^y) (\hat{n}_{ij}^x \hat{n}_{ij}^y + \hat{n}_{ik}^x \hat{n}_{ik}^y) \\
\frac{\partial^2 A}{\partial r_n^a \partial \gamma} &= \frac{\delta_{ji}^n}{r_{ij}} \left[\delta_{ay} \hat{n}_{ik}^x + \delta_{ax} \hat{n}_{ik}^y - \hat{n}_{ij}^a (\hat{n}_{ij}^x \hat{n}_{ik}^y + \hat{n}_{ik}^x \hat{n}_{ij}^y) - \hat{n}_{ik}^a (\hat{n}_{ij}^x \hat{n}_{ij}^y + \hat{n}_{ik}^x \hat{n}_{ik}^y) \right. \\
&\quad \left. + \cos \theta_{ijk} (\hat{n}_{ij}^a (3 \hat{n}_{ij}^x \hat{n}_{ij}^y + \hat{n}_{ik}^x \hat{n}_{ik}^y) - (\delta_{ay} \hat{n}_{ij}^x + \delta_{ax} \hat{n}_{ij}^y)) \right] \\
&\quad + \frac{\delta_{ki}^n}{r_{ik}} \left[\delta_{ay} \hat{n}_{ij}^x + \delta_{ax} \hat{n}_{ij}^y - \hat{n}_{ik}^a (\hat{n}_{ij}^x \hat{n}_{ik}^y + \hat{n}_{ik}^x \hat{n}_{ij}^y) - \hat{n}_{ij}^a (\hat{n}_{ij}^x \hat{n}_{ij}^y + \hat{n}_{ik}^x \hat{n}_{ik}^y) \right. \\
&\quad \left. + \cos \theta_{ijk} (\hat{n}_{ik}^a (3 \hat{n}_{ik}^x \hat{n}_{ik}^y + \hat{n}_{ij}^x \hat{n}_{ij}^y) - (\delta_{ay} \hat{n}_{ik}^x + \delta_{ax} \hat{n}_{ik}^y)) \right]
\end{aligned} \tag{A.5}$$

A.2 Complex modulus for $Z = 6$

For depleted lattices in $d = 3$ at $Z = 6$ we can approximate $D(\omega)\Gamma(\omega)$ according to (2.21) as:

$$D(\omega)\Gamma(\omega) = \frac{1}{12\omega_D^2}\omega^2(\omega_D - \omega) \quad (\text{A.6})$$

With this we can solve the frequency integral that gives us $G^*(\Omega)$ analytically:

$$\begin{aligned} G^*(\Omega) &= G^A - 3\frac{N}{V}\int_0^\infty \frac{D(\omega)\Gamma(\omega)}{\omega^2 - \Omega^2 + i\nu\Omega} d\omega \\ &= G^A - \frac{N}{V}\frac{1}{4\omega_D^2}\int_0^{\omega_D} \frac{\omega^2(\omega_D - \omega)}{\omega^2 - \Omega^2 + i\nu\Omega} d\omega \end{aligned} \quad (\text{A.7})$$

For our systems we can use $G^A(Z = 6) = 1/2$ and $N/V = 4$ to get:

$$\begin{aligned} G^*(\Omega) &= \frac{1}{2} - \frac{1}{\omega_D^2}\int_0^{\omega_D} \frac{\omega^2(\omega_D - \omega)}{\omega^2 - \Omega^2 + i\nu\Omega} d\omega \\ &= \frac{\sqrt{\Omega}}{\omega_D} \left(\sqrt{i\nu - \Omega} \arctan2 \left[\omega_D, \sqrt{\Omega(i\nu - \Omega)} \right] - \frac{1}{2}\frac{\sqrt{\Omega}}{\omega_D} \log \left[\frac{\omega_D^2 + \Omega(i\nu - \Omega)}{\Omega(i\nu - \Omega)} \right] \right) \end{aligned} \quad (\text{A.8})$$

Here $\arctan2(x, y)$ denotes the angle ϕ of the complex number $z = x + iy$. By using the definition of the complex arctan and logarithm one can derive the explicit expression for the real and imaginary part of (A.8), which are too lengthy to be shown here.

A.3 Analytic description of freely joined chains

Although there is not tool to analytically describe a full polymer system as described in this work, we will present model systems that will help with the interpretation of the numerical results. We consider a toy model for the determination

of the skeletal vibration modes of a single polymer chain. The following assumptions are made: (i) the chain is fully flexible (vanishing bending stiffness); (ii) only in-plane motions are considered (rocking or other out-of-plane vibrations are neglected). These assumptions are required in order to obtain analytical results. We will start with the most general case of chains of length L with arbitrary angles between adjacent bonds. The Hessian has the following block structure:

$$H = \begin{pmatrix} A_{12} & -A_{12} & 0 & 0 & 0 & & 0 \\ -A_{12} & A_{12} + A_{23} & -A_{23} & 0 & 0 & \cdots & 0 \\ 0 & -A_{23} & A_{23} + A_{34} & -A_{34} & 0 & & 0 \\ 0 & 0 & -A_{34} & A_{34} + A_{45} & -A_{45} & & \vdots \\ & \vdots & & & & \ddots & -A_{L-1L} \\ 0 & 0 & 0 & 0 & \cdots & -A_{L-1L} & A_{L-1L} \end{pmatrix} \quad (\text{A.9})$$

with blocks given by:

$$A_{ij} = \frac{\kappa}{m} \begin{pmatrix} n_{ij}^x n_{ij}^x & n_{ij}^x n_{ij}^y & n_{ij}^x n_{ij}^z \\ n_{ij}^y n_{ij}^x & n_{ij}^y n_{ij}^y & n_{ij}^y n_{ij}^z \\ n_{ij}^z n_{ij}^x & n_{ij}^z n_{ij}^y & n_{ij}^z n_{ij}^z \end{pmatrix} \quad (\text{A.10})$$

with the unit vector \mathbf{n}_{ij} which goes from monomer i to a nearest-neighbour j , and spring constant κ which corresponds to the effective spring constant of the FENE bonds κ_{FENE} . To get the characteristic polynomial $p(\lambda)$, one has to evaluate the determinant $|H - \lambda \mathbf{1}|$. We can iteratively solve this by using the formula for block matrices:

$$\begin{vmatrix} A & B \\ C & D \end{vmatrix} = |D| |A - BD^{-1}C| \quad (\text{A.11})$$

where the entries are matrices and the relation for our 3×3 blocks:

$$A \cdot B \cdot A = \frac{\kappa^2}{m^2} \cos^2 \theta_{AB} A \quad (\text{A.12})$$

where θ_{AB} is the angle between the bonds belonging to A and B . After some calculation we get the following recursion formula (omitting the $2L + 1$ trivial eigenvalues $\lambda = 0$) for the above matrix:

$$\begin{aligned} p_0(x) &= 1 \\ p_1(x) &= x \end{aligned} \tag{A.13}$$

$$p_n(x) = x p_{n-1}(x) - \cos^2 \theta_{n-1n-2} p_{n-2}(x)$$

where $x = \frac{m}{\kappa} \lambda - 2$. It is important to note that the characteristic polynomial, and hence the eigenvalues, are only dependent on the angle between adjacent bonds. Therefore they are invariant under deformations where parts of the chain rotate around a single bond, which makes them useful as model for the polymer systems in this work as the chains are in general non-flat. Note that n denotes the number of bonds in a chain, and not the number of particles in the chain ($n = L - 1$). For arbitrary angles between the bonds it is not possible to describe the roots of this polynomial, except for short chains (see below). But, if all angles are the same we can bring (A.13) into the form of the Chebyshev polynomials of the second kind $U_n(x)$ by substituting $\tilde{x} = x/2 \cos \theta$:

$$\begin{aligned} p_n(\tilde{x}) &= \cos^n \theta U_n(\tilde{x}) \\ \tilde{x} &= \frac{x}{2 \cos \theta} = \frac{\frac{m}{\kappa} \lambda - 2}{2 \cos \theta}. \end{aligned} \tag{A.14}$$

The roots of $U_n(x)$ are $x_k = \cos\left(\frac{k}{n+1}\pi\right)$; $k = 1, \dots, n$, which gives us the eigenvalues

of the linear chain with constant angle as:

$$\lambda_k = \omega_k^2 = 2\frac{\kappa}{m} \left(1 + \cos\theta \cos \left[\frac{k\pi}{n+1} \right] \right)$$

$$D(\omega) = \frac{2}{\pi} \frac{\omega}{\sqrt{4\frac{\kappa^2}{m^2} \cos^2\theta - (\omega^2 - 2\frac{\kappa}{m})^2}} \quad (\theta \neq \pi/2) \quad (\text{A.15})$$

$$\rho(\omega) = \delta\left(\omega - \sqrt{2\frac{\kappa}{m}}\right) \quad (\theta = \pi/2).$$

This result can also be derived from exploiting the periodicity of the chain with constant angle, as was done by J. Kirkwood [52]. If we assume that the chain points along the x-axis we can identify the previously introduced along-chain and perpendicular motion (see Fig. 4.3) as A and B in Eq.(6) of [52]. By using the dispersion relation found in this work, we can solve for those two quantities and find the weigh functions:

$$X_l(\omega) = \frac{|A|^2}{|A|^2 + |B|^2} = \frac{\cos\theta + 1}{\cos\theta} \frac{\omega^2 + 2\frac{\omega}{m}(\cos\theta - 1)}{2\omega^2}$$

$$X_t(\omega) = \frac{|B|^2}{|A|^2 + |B|^2} = \frac{\cos\theta - 1}{\cos\theta} \frac{\omega^2 - 2\frac{\kappa}{m}(\cos\theta + 1)}{2\omega^2} \quad (\text{A.16})$$

As mentioned before, for the flexible case with distributed angles an analytical solution is not accessible for a chain of arbitrary length. But we can give the

eigenvalues in the case of short chains with $L = 2, 3, 4, 5$:

$$L = 2 : \quad \frac{m}{\kappa} \omega^2 = 2$$

$$L = 3 : \quad \frac{m}{\kappa} \omega^2 = 2 \pm \cos \theta_1$$

$$L = 4 : \quad \frac{m}{\kappa} \omega^2 = 2, 2 \pm \sqrt{\cos^2 \theta_1 + \cos^2 \theta_2}$$

$$L = 5 : \quad \frac{m}{\kappa} \omega^2 =$$

$$\pm \frac{1}{\sqrt{2}} \sqrt{\cos^2 \theta_1 + \cos^2 \theta_2 + \cos^2 \theta_3 \pm \sqrt{(\cos^2 \theta_1 + \cos^2 \theta_2 + \cos^2 \theta_3)^2 - 4 \cos^2 \theta_1 \cos^2 \theta_3}} \quad (\text{A.17})$$

A.4 Analytical description of a single chain with

$$L = 3$$

For a single chain of length $L = 3$ we can even derive analytic results for the case of bending interaction, which will provide useful insights into the dependence of mode distribution and motion pattern on the bending stiffness. The chain consists of three particles with two FENE pair interactions and one bending interaction. The Hessian is calculated by using the (A.2) and (A.5). As the eigenvalues of the Hessian are invariant under spatial rotations, we can chose the triplet to be lying in the x-y plane with coordinates of the three particles being $P_1 = -r(s, 0)$, $P_2 = r(0, c)$, $P_3 = r(s, 0)$ and $s = \sin \theta/2$, $c = \cos \theta/2$. The Hessian reads as:

$$H = \frac{\kappa}{m} \begin{pmatrix} s^2 + \gamma' c^2 & -(1 - \gamma') s c & -s^2 & (1 - 2\gamma') s c & -\gamma' c^2 & \gamma' s c \\ -(1 - \gamma') s c & c^2 + \gamma' s^2 & s c & -c^2 - 2\gamma' s^2 & -\gamma' s c & \gamma' s^2 \\ -s^2 & s c & 2s^2 & 0 & -s^2 & -s c \\ (1 - 2\gamma') s c & -c^2 - 2\gamma' s^2 & 0 & 2c^2 + 4\gamma' s^2 & -(1 - 2\gamma') s c & -c^2 - 2\gamma' s^2 \\ -\gamma' c^2 & -\gamma' s c & -s^2 & -(1 - 2\gamma') s c & s^2 + \gamma' c^2 & (1 - \gamma') s c \\ \gamma' s c & \gamma' s^2 & -\gamma' s c & -c^2 - 2\gamma' s^2 & (1 - \gamma') s c & c^2 + \gamma' s^2 \end{pmatrix} \quad (\text{A.18})$$

where κ denotes the spring constant of the FENE bonds, m the mass of the particles and $\gamma' = \kappa_{bend}/(\kappa r^2)$ the reduced bending stiffness. The above matrix has 3 non-zero eigenvalues, leading to the following eigenfrequencies:

$$\begin{aligned}\omega_1^2 &= \frac{\kappa}{m}(2 - \cos \theta) \\ \omega_2^2 &= \frac{\kappa}{2m} \left(2(1 + 2\gamma') + (1 - 2\gamma') \cos \theta + \sqrt{(2(1 + 2\gamma') + (1 - 2\gamma') \cos \theta)^2 - 24\gamma'} \right) \\ \omega_3^2 &= \frac{\kappa}{2m} \left(2(1 + 2\gamma') + (1 - 2\gamma') \cos \theta - \sqrt{(2(1 + 2\gamma') + (1 - 2\gamma') \cos \theta)^2 - 24\gamma'} \right)\end{aligned}\tag{A.19}$$

As we can see, one eigenfrequency ω_1 is independent of the bending stiffness, while ω_3 shows a convergent behaviour against $\omega \rightarrow \sqrt{3\kappa/m/(2 - \cos \theta)}$ and ω_2 diverges like $\sim \sqrt{\gamma'}$.

Bibliography

- [1] P. Debye, "*Zur Theorie der spezifischen Wärme*", Ann. d. Phys. **344**, 789 (1912).
- [2] M. Born and K. Huang, "*Dynamical Theory of Crystal Lattices*", (Oxford University Press, 1954).
- [3] I. M. Lifshitz, "*Some problems of the dynamic theory of non-ideal crystal lattices*", Nuovo Cim. Suppl. **3**, 716 (1956).
- [4] P. Soven, "*Coherent-Potential Model of Substitutional Disordered Alloys*", Phys. Rev. **156**, 809 (1967).
- [5] T. W. Taylor, "*Vibrational properties of Imperfect Crystals with Large Defect Concentrations*", Phys. Rev. **156**, 1017 (1967).
- [6] S. Köhler, G. Ruocco, and W. Schirmacher, "*Coherent potential approximation for diffusion and wave propagation in topologically disordered systems*", Phys. Rev. B **88**, 064203 (2013).
- [7] A. Lemaître and C. Maloney, "*Sum Rules for the Quasi-Static and Visco-Elastic Response of Disordered Solids at Zero Temperature*", J. Stat. Phys. **123**, 415 (2006).
- [8] H. C. Andersen, "*Molecular dynamics simulations at constant pressure and/or temperature*", J. Chem. Phys. **72**, 2384 (1980).
- [9] J. Ray and A. Rahman, "*Statistical ensembles and molecular dynamics studies of anisotropic solids*", J. Chem. Phys. **80**, 4423 (1984).

-
- [10] I. Souza and J. L. Martins, "*Metric tensor as the dynamical variable for variable-cell-shape molecular dynamics*", Phys. Rev. B **55**, 8733 (1997).
- [11] R. Milkus and A. Zaccone, "*Local inversion-symmetry breaking controls the boson peak in glasses and crystals*", Phys. Rev. B **93**, 094204 (2016).
- [12] R. Milkus and A. Zaccone, "*Atomic-scale origin of dynamic viscoelastic response and creep in disordered solids*", Phys. Rev. E **95**, 023001 (2017).
- [13] J. Krausser, R. Milkus and A. Zaccone, "*Non-affine lattice dynamics of defective fcc crystals*", Soft Matter **13**, 6079-6089 (2017).
- [14] H. Shintani and H. Tanaka, "*Universal link between the boson peak and transverse phonons in glass*", Nat. Mater. **7**, 870 (2008).
- [15] D. Kaya, N.L. Green, C.E. Maloney, and M.F. Islam, "*Normal modes and density of states of disordered colloidal solids*", Science **329**, 656 (2010).
- [16] R. Zargar, J. Russo, P. Schall, H. Tanaka, and D. Bonn, "*Disorder and excess modes in hard-sphere colloidal systems*", EPL **108**, 38002 (2014).
- [17] A. I. Chumakov, et al., "*Role of Disorder in the Thermodynamics and Atomic Dynamics of Glasses*", Phys. Rev. Lett. **112**, 025502 (2014).
- [18] A. Tanguy, J. P. Wittmer, and J.-L. Barrat, "*Continuum limit of amorphous elastic bodies. III. Three-dimensional systems*", Phys. Rev. B **72**, 224206 (2005).
- [19] P. B. Allen and J. L. Feldman, "*Thermal conductivity of disordered harmonic solids*", Phys. Rev. B **48**, 12581 (1993).
- [20] J. L. Feldman, M. D. Kluge, P. B. Allen, and F. Wooten, "*Thermal conductivity and localization in glasses: Numerical study of a model of amorphous silicon*", Phys. Rev. B **48**, 12589 (1993).
- [21] P. B. Allen, J. L. Feldman, J. Fabian, and F. Wooten, "*Diffusons, Locons, Propagons: Character of Atomic Vibrations in Amorphous Si*", Phil. Mag. B **79**, 1715 (1999).
- [22] A. F. Ioffe and A. R. Regel, "*Non-crystalline, amorphous and liquid electronic semiconductors*", Prog. Semicond. **4**, 237 (1960).

- [23] N. Xu, V. Vitelli, A. J. Liu, and S. R. Nagel, "*Anharmonic and quasi-localized vibrations in jammed solids*" Modes for mechanical failure", EPL **90**, 56001 (2010).
- [24] Y. M. Beltukov, V. I. Kozub, and D. A. Parshin, "*Ioffe-Regel criterion and diffusion of vibrations in random lattices*", EPL **90**, 56001 (2010).
- [25] L. E. Silbert, A. J. Liu, and S. R. Nagel, "*Vibrations and Diverging Length Scales Near the Unjamming Transition*", Phys. Rev. Lett. **95**, 098301 (2005).
- [26] K. Vollmayr, W. Kob, and K. Binder, "*How do the properties of a glass depend on the cooling rate? A computer simulation study of a Lennard-Jones system*", J. Chem. Phys. **105**, 4714 (1996).
- [27] M. Y. Ha, G. Choi, D. H. Kim, H. S. Kim, S. H. Park, and W. B. Lee, "*Effect of lattice relaxation on thermal conductivity of fcc-based structures: an efficient procedure of molecular dynamics simulation*", Modelling Simul. Mater. Sci. Eng. **25**, 055011 (2017).
- [28] C. P. Goodrich, A. J. Liu, and S. R. Nagel, "*Solids between the mechanical extremes of order and disorder*", Nat. Phys. **10**, 578 (2014).
- [29] P. J. Steinhardt, D. R. Nelson, and M. Ronchetti, "*Bond-orientational order in liquids and glasses*", Phys. Rev. B **28**, 784 (1983).
- [30] M.F. Thorpe, "*Continuous deformations in random networks*", J. Non-Cryst. Solids **57**, 355 (1983).
- [31] A. Zaccane and E. Scossa-Romano, "*Approximate analytical description of the nonaffine response of amorphous solids*", Phys. Rev. B **83**, 184205 (2011).
- [32] A. Zaccane, J. R. Blundell, and E. M. Terentjev, "*Network disorder and nonaffine deformations in marginal solids*", Phys. Rev. B **84**, 174119 (2011).
- [33] B. P. Tighe, "*Relaxations and Rheology near Jamming*", Phys. Rev. Lett. **107**, 158303 (2011).
- [34] B. P. Tighe, "*Dynamic Critical Response in Damped Random Spring Networks*", Phys. Rev. Lett. **109**, 168303 (2012).

- [35] M. G. Yucht, M. Sheinman, and C. P. Broedersz, "*Dynamical behavior of disordered spring networks*", *Soft Matter* **9**, 7000 (2013).
- [36] J. Chattoraj and A. Lemaître, "*Elastic Signature of Flow Events in Supercooled Liquids Under Shear*", *Phys. Rev. Lett.* **111**, 066001 (2013).
- [37] S. Gelin, H. Tanaka, and A. Lemaître, "*Anomalous phonon scattering and elastic correlations in amorphous solids*", *Nat. Mater.* **15**, 1177 (2016).
- [38] S. Chowdhury, S. Abraham, T. Hudson, and Peter Harrowell, "*Long range stress correlations in the inherent structures of liquids at rest*", *J. Chem. Phys.* **144**, 124508 (2016).
- [39] A. Marruzzo, W. Schirmacher, A. Fratallocchi, and G. Ruocco, "*Heterogeneous shear elasticity of glasses: the origin of the boson peak*", *Sci. Rep.* **3**, 1407 (2013).
- [40] R. Busselez, T. Pezeril, and V. E. Gusev, "*Structural heterogeneities at the origin of acoustic and transport anomalies in glycerol glass-former*", *J. Chem. Phys.* **140**, 234505 (2014).
- [41] J. Krausser and R. Milkus, "*Long range correlation in depleted spring networks*", preprint (2017).
- [42] J. H. Irving and John G. Kirkwood, "*The Statistical Mechanical Theory of Transport Processes. IV. The Equations of Hydrodynamics*", *J. Chem. Phys.* **18**, 817 (1950).
- [43] C. P. Broedersz, X. Mao, T. C. Lubensky, and F. C. MacKintosh, "*Criticality and isostaticity in fibre networks*", *Nat. Phys.* **7**, 983 (2011).
- [44] J. D. Eshelby, "*The determination of the elastic field of an ellipsoidal inclusion, and related problems*", *Proc. R. Soc. London, Ser. A* **241**, 376 (1957).
- [45] T. Egami and D. Srolovitz, "*Local structural fluctuations in amorphous and liquid metals: a simple theory of the glass transition*", *J. Phys. F: Metal Phys.* **12**, 2141 (1982).
- [46] T. L. Hoang, A. Arsenlis, H. J. Lee-Voigt, D. C. Chrzan, and B. D. Wirth, "*Atomistic study of Eshelby's inclusion and inhomogeneity problems in a model bcc crystal*", *Modell. Simul. Mater. Sci. Eng.* **19**, 085001 (2011).

- [47] S. Ganguly, S. Sengupta, and P. Sollich, "*Statistics of non-affine defect precursors: tailoring defect densities in colloidal crystals using external fields*", *Soft Matter* **11**, 4517 (2015).
- [48] V. Chikkadi, G. Wegdam, D. Bonn, B. Nienhuis, and P. Schall, "*Long-Range Strain Correlations in Sheared Colloidal Glasses*", *Phys. Rev. Lett.* **107**, 198303 (2011).
- [49] B. Wu, T. Iwashita, and T. Egami, "*Anisotropic stress correlations in two-dimensional liquids*", *Phys. Rev. E* **91**, 032301 (2015).
- [50] P. C. Painter, M. M. Coleman, and J. L. Koenig, "*Molecular Spectra and Molecular Structure: Infrared and Raman Spectra of Polyatomic Molecules*", (Van Nostrand Reinhold, 1982).
- [51] D. I. Bower and W. Maddams, "*The vibrational spectroscopy of polymers*", (Cambridge University Press, 1992).
- [52] J. G. Kirkwood, "*The Skeletal Modes of Vibration of Long Chain Molecules*", *J. Chem. Phys.* **7**, 506 (1939).
- [53] K. S. Pitzer, "*The Vibration Frequencies and Thermodynamic Functions of Long Chain Hydrocarbons*", *J. Chem. Phys.* **8**, 711 (1940).
- [54] P. Higgs, "*Vibration Spectra of Helical Molecules*", *Proc. Roy. Soc. A* **220**, 472 (1953).
- [55] K. Kremer and G. S. Grest, "*Dynamics of entangled linear polymer melts: A molecular dynamics simulation*", *J. Chem. Phys.* **92**, 5057 (1990).
- [56] V. Ilyin, I. Procaccia, I. Regev, and Y. Shokef, "*Randomness-induced redistribution of vibrational frequencies in amorphous solids*", *Phys. Rev. B* **80**, 174201 (2009).
- [57] R. Milkus, C. Ness, V. Palyulin, J. Weber, A. Lapkin and A. Zaccone, "*Interpretation of the vibrational spectra of glassy polymers using coarse-grained simulations*", submitted to *Macromolecules* (2017).
- [58] S. Plimpton, "*Fast Parallel Algorithms for Short-Range Molecular Dynamics*", *J. Comp. Phys.* **117**, 1 (1995).

- [59] T. Damart, A. Tanguy, and D. Rodney, "*Theory of harmonic dissipation in disordered solids*", Phys. Rev. B **95**, 054203 (2017).
- [60] R. M. Stratt, "*The Instantaneous Normal Modes of Liquids*", Acc. Chem. Res. **28**, 201 (1995).
- [61] Q. Cui and I. Bahar, "*Normal Mode Analysis: Theory and Applications to Biological and Chemical Systems*", (Chapman and Hall/CRC, 2006).
- [62] T. Keyes, "*Unstable modes in supercooled and normal liquids: Density of states, energy barriers, and self diffusion*", J. Chem. Phys. **101**, 5081 (1994).
- [63] S.D. Bembenek and B.B. Laird, "*Instantaneous normal modes analysis of amorphous and supercooled silica*", J. Chem. Phys. **114**, 2340 (2000).
- [64] R. Schulz, M. Krishnan, I. Daidone, and J. C. Smith, "*Instantaneous Normal Modes and the Protein Glass Transition*", Biophys. J. **96**, 476 (2009).
- [65] B. Madan, T. Keyes, and G. Seeley, "*Normal mode analysis of the velocity correlation function in supercooled liquids*", J. Chem. Phys. **94**, 6762 (1991).
- [66] T. S. Jain and J. J. de Pablo, "*Influence of confinement on the vibrational density of states and the Boson peak in a polymer glass*", J. Chem. Phys. **120**, 9371 (2004).